A STUDY OF AIR FLOW IN A NETWORK OF PIPES USED IN ASPIRATED SMOKE DETECTORS

By

Rohitendra K Singh

A thesis submitted in fulfilment of the requirements for the degree of
Master of Engineering in Mechanical Engineering

School of Engineering and Science

Victoria University

Victoria, Australia.

July, 2009

SUMMARY

A Very Early–warning Smoke Detection Apparatus (VESDA^{TM}) detects the earliest traces of smoke by continuously sampling the air from a designated area. Air sampling is achieved by use of a system of long pipes containing numerous small inlet orifices termed as sampling holes. The air samples are drawn to the detector by means of an aspirator.

In spite of the high sensitivity of the detector, much of this advantage can be lost if the smoke transport time within the pipe network is excessive. Consequently there has been a legislation introduced by Standards such as AS 1670 and BS 5839 stating the maximum transport time to be within 60 seconds of entering that extremity of a pipe system of 200 meters aggregate length, and the suction pressure was to be no less than 25 Pascals.

Once the pipe network is installed, it is impractical and often impossible to test the transport time and suction pressure drop of every sampling hole in a complex network of pipes. Therefore, a software modelling tool is required to accurately predict these parameters to 90% of measured value with high accuracy.

The flow regimes within the sampling pipes proved complex, involving frequent transitions between laminar and turbulent flows due to disturbances caused to the main flow by jet flows from the sampling holes. Consequently, the published equations to determine friction factors does not predict pressure loss and transport time results to an acceptable accuracy for this thesis.

Computational Fluid Dynamics simulations were carried out at various magnitudes of disturbances similar to the effects in VESDA pipe network. The data from the CFD were analysed and the results were used as a guide to develop mathematical models to calculate the friction factor in flow regimes where jet disturbances are present.

The local loss coefficients of fittings such as bends and couplings were experimentally determined for all types of fittings used in VESDA pipe networks.

The local loss coefficients that were determined made significant improvements in calculating pressure losses compared to the results obtained when commonly used loss coefficient values were used.

The characteristics of the VESDA aspirators of all models were determined. The experiments were carefully set up to ensure the apparatus did not have any influence on the aspirator performance. Mathematical models were developed for each VESDA model.

A relationship between the magnitude of disturbance and the delay it caused for the smoke to travel from one segment to the next was established. From this relationship, a new transport time mathematical model was developed.

Validations of all mathematical models were carried out in different pipe configurations. In all cases the results calculated were within 90% or better compared to the measured results.

DECLARATION

"I, Rohitendra Kumar Singh, declare that the Master by Research thesis entitled A STUDY OF AIR FLOW IN A NETWORK OF PIPES USED IN ASPIRATED SMOKE DETECTORS is no more than 60,000 words in length including quotes and exclusive of tables, figures, appendices, bibliography, references and footnotes. This thesis contains no material that has been submitted previously, in whole or in part, for the award of any other academic degree or diploma. Except where otherwise indicated, this thesis is my own work".

Signature Date

ACKNOWLEDGEMENTS

I am deeply indebted to my Principal Supervisor Dr. Jun De Li for his sustained and unfailing interest and his invaluable guidance, kind concern and support throughout this work. To my Co-Supervisor Dr.Vincent Rouillard, I express my sincere thanks and gratitude for his keen interest, excellent guidance and expert advice he has given me throughout this work

I am very thankful to Visions Systems Ltd, Melbourne, for giving me the opportunity to carry out this work and for their financial support associated with this project. My sincere thanks are also due to Mr. Charles Mays, former Director of the Department of Research and Development, Visions Systems Ltd, Melbourne, for his continuous interest and encouragement.

Grateful appreciation is extended to all the staff members and post-graduate students of the school for their help and courtesy extended to me during the period of my study at the University.

Finally, I would like thank my entire family for their encouragement and support they have given me throughout.

LIST OF SYMBOLS

A	m^2	Cross sectional area of main pipe
B		Boundary layer thickness
C_f		Correction factor
D	m	Main pipe diameter
D_{CT}	m	Capillary tube diameter
d	m	Sampling hole diameter
f		Frictional factor
g	m/s^2	Gravitational acceleration
V	m/s	Velocity of air in the main pipe
v	m/s	Velocity of air in the sampling hole
L	m	Length of pipe
L_D	m	Development length
L_T	m	Extended Length
L_{CT}	m	Length of capillary tube
K		Loss coefficient
Q	m^3	Volume flow rate
h_f		Head loss due to friction
Re		Reynolds number
λ		Constants
μ	$Pa.s$	Dynamic viscosity of air
ρ	Kg/m^3	Density of air
$P_{manifold}$	Pa	Pressure in the manifold
T_{lam}	s	Transport time in a segment when the flow is laminar
T_{tur}	s	Transport time in a segment when the flow is turbulent
Ts	s	Transport time for the smoke to travel in a segment
Tt	s	Total transport time
V_{core}	m/s	Core velocity of air in the pipe

V_{Mean}	m/s	Mean velocity of air in the pipe
V_r	m/s	velocity ratio ($V_{core/}\ V_{Mean}$)
V_{CT}	m/s	Velocity of air in the capillary tube
Q_{CT}	m^3/s	Flow rate of air in the capillary tube
F_{sim}		Friction factor from simulated results
F_{lam}		Friction factor calculated from laminar flow equation

CHAPTER 1

INTRODUCTION

1.1 Background.

This thesis presents the result of a study of the flow characteristics in a network of pipes used to deliver sampled air to a detector, which looks for the presence of a target particulate. Specifically, this project studies air-sampling networks used with the smoke detecting system designed and manufactured by Vision Systems Limited.

Vision Systems Limited is the world's leading manufacturer of Very Early Smoke Detection Apparatus (VESDA). The VESDA system provides very early warning of potential fires by detecting smoke particles at the incipient stage of a fire. Detection at this stage is crucial, as losses of equipment, early and orderly evacuation to save human lives and valuable assets are inevitable once the flaming stage of a fire is reached.

1.2 The VESDA smoke detection system

Figure 1 shows a diagram of the VESDA smoke detection system. The VESDA system consists of an aspirator driven by a DC motor, a detection unit, and up to four sampling pipes. In each pipe, small holes are drilled (normally at regular intervals) for sampling air within an area or room and one end of each pipe is connected to a detection chamber. Low pressure, inside the pipes relative to the ambient, is produced by the aspirator to draw air into the pipes through small holes, (usually ranging between 20 to 40 in number). The sampled air flows along the pipes and into the detection chamber. A typical pipe layout is shown in the appendices, figureA1.

Smoke arriving near the pipe during the early stage of the fire will be drawn into one of the holes in the network of pipes.

A sample of this smoke and air mixture is then passed through a filter to remove dust and dirt before it enters the detection chamber. Scattered laser light is used to detect the presence of particles which indicates within the sampled air the possibility of the early stage of fire.

As the smoke enters the main pipe and because of the high velocity in the sampling hole, it takes very little time to achieve full mixing. Consequently, the smoke front will be spread by molecular diffusion which is a comparatively much slower process. Therefore this would have limited effect on the smoke time delay.

A VESDA unit cannot differentiate between fine dust that may pass through the filters and smoke. All VESDA units are calibrated in controlled clean rooms to sensitivity levels from 0.001% to 4 % obscuration.

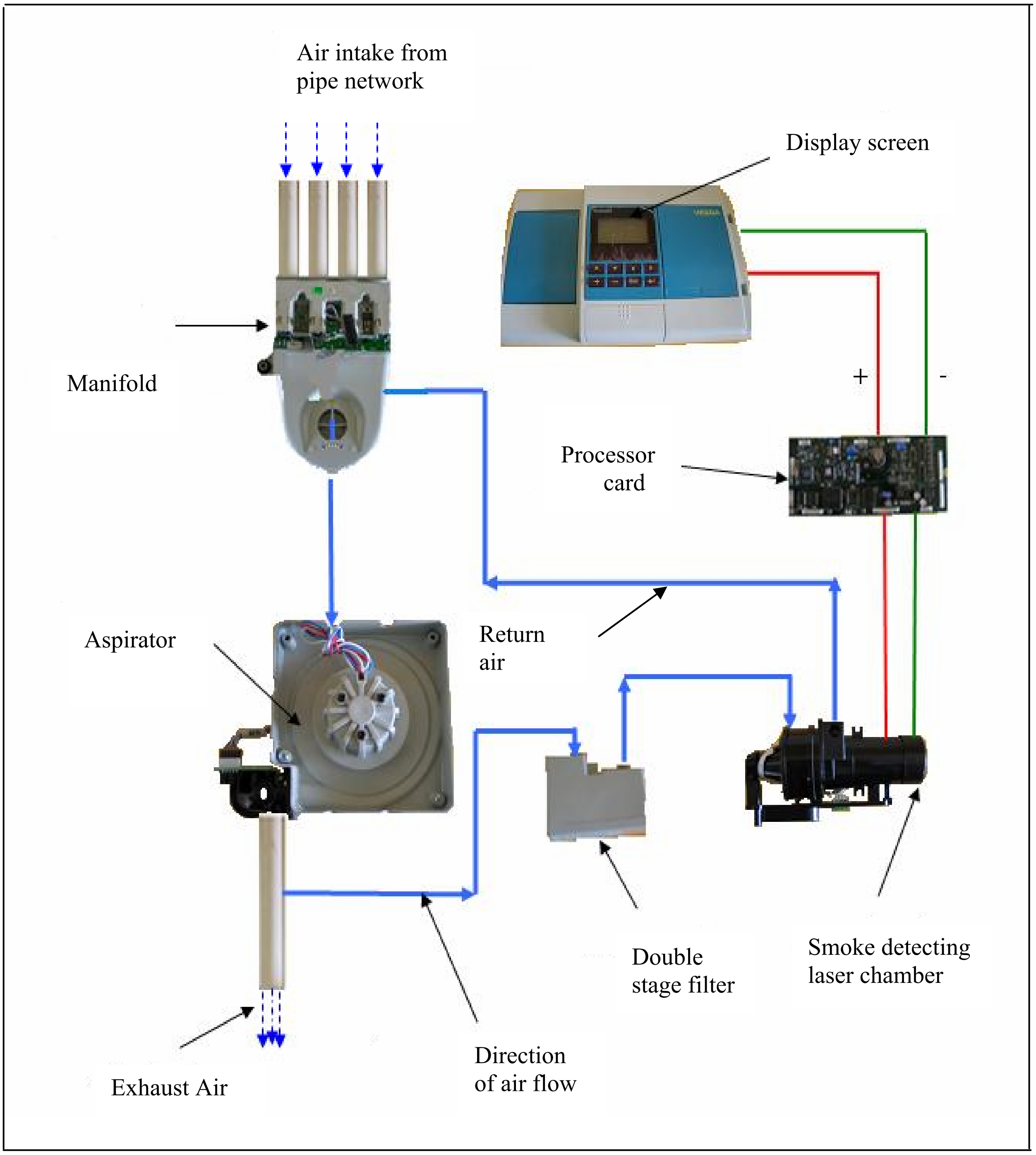

Figure 1 VESDA smoke detection system

1.3 Uncertainties in modelling the flow in a network of pipes with sampling holes

Ideally a smoke detector should respond immediately when smoke is present. However, for a system like VESDA, immediate smoke detection cannot be achieved due to the time required to transport the smoke from where it occurs to the detection unit. This time delay depends on three important factors; (a) the suction pressure drop in the sampling pipes; (b) air velocity in the pipes; and (c) the distance between the sampling hole and the detecting unit.

The suction pressure at each sampling hole and the hole diameter determine the flow rate in each segment of the sampling pipe. Velocities calculated from these flow rates in each segment can be used to calculate the transport time. It is also important that the suction pressure is high enough so that the smoke has a better chance to be drawn into the sampling pipe as it passes by a sampling hole.

Legislations such as the British and Australian Standards BS5839, BS6266, and AS 1670, set the acceptable minimum suction pressure drop of a sampling hole at 25 Pa and the maximum acceptable “transport time” from any sampling hole to the detection unit at 60 seconds.

Once installed, it is impractical and often impossible to test the transport time, suction pressure drop and dilution factor of every sampling hole in a complex network of pipes. Therefore, a tool to accurately predict these parameters is needed.

A single VESDA pipe network system can normally achieve coverage of an area up to 2000 m^2. In estimating the suction pressures, smoke transport time and smoke dilution factor, the characteristics of the aspirator and the airflows in the pipe networks need to be modelled. The flow in the pipe network is affected by the length of pipe, number of bends and joins (couplings) used, and the number of sampling holes. Only after the effects from all these network elements are taken into account can the predicted transport time closely match the actual transport time.

Currently, Vision Systems Limited has a computer package known as ASPIRE® to model the airflows in the pipe network. The software can give some predictions on transport time and the suction pressure from each sampling hole. However, field experience shows that the predicted transport times and suction pressures routinely have errors of 20% or more. Legislations in the U.S.A. and Europe require that models should be able to generate prediction within 90% or better of the measured values.

The second problem with ASPIRE® modeling software is that it can only model the airflow with up to four main sampling pipes. It does not have the capability of predicting the suction pressure and transport time when extra sampling pipes are branched from the main sampling pipes to form a more complex network.

In order to determine the transport time and the suction pressures accurately for each sampling location, there is a need to take into account the effects of disturbances to the flow due to jet induction at the sampling holes and the effects of local losses due to sudden enlargements and contractions of the flow path.

1.4 The objective of this thesis

There is a significant level of uncertainty in determining the pressure loss, particularly when the main flow is disturbed by jet inductions. The disruption could affect the friction factor in the segment of the pipe immediately downstream of a sampling hole. The extent of this effect is not known.

The objective of this thesis is to systematically study the effects of the jet disturbances on friction factor and to experimentally determine the local loss coefficients of various fittings such as bends, joints, and branches in order to develop a new mathematical model to significantly improve the prediction capability to achieve an accuracy of 90% or better.

The collection and analysis of the experimental data is challenging because of the small pressure drop between each segment, which consequently will have a diminutive effect on the flow rates over short distances. Available experimental equipment in the field is in general not sensitive enough to capture reliably the small change in pressure. It is therefore proposed to use Computational Fluid Dynamics (CFD) to simulate the flow in a pipe with small sampling holes. Using a CFD package, the disturbing effect of the flow entering the sampling pipe through the small holes is studied and correlations to the pressure drop near the sampling hole will be generated at different levels of disturbance and at various Reynolds numbers. These results are used to guide the development of the mathematical models.

The models are used to predict the pressures and transport time from each location of the sampling hole in the VESDA pipe network and compared with the experimental results. By doing so, the mathematical models are validated.

1.5 Significance

The significance of this research is to find ways to improve the techniques and thereby the accuracy of mathematically modelling a pipe flow network system. An improved mathematical model will result in significantly better estimates for transport time, suction pressures and dilution factors thereby providing more confidence that a pipe network can be installed to meet the legislative requirements. This will enable such systems to be installed and commissioned correctly, with the significant benefit of reducing the risk to human life and property from fire.

CHAPTER 2

LITERATURE REVIEW

The literature reviews described in this chapter include two parts. The first part focuses on the theories of energy losses due to friction, disturbances, and boundary layer conditions. The second part focuses upon the published literature relating to aspirated fire detection systems. A critical analysis of the publications is taken in order to identify the strengths and weaknesses of the current practice in modelling pipe networks.

2.1 Equations relating to energy losses in pipes

Considering a straight pipe shown in Figure 2.1, the flow between the inlet and outlet follows the Bernoulli's equation (White, 1994)

$$\int_1^2 \frac{\partial V}{\partial t} ds + \int_1^2 \frac{dP}{\rho} + \frac{1}{2}\left(V_2^2 - V_1^2\right) + g(z_2 - z_1) = 0 \tag{2.1}$$

where P is the pressure, ρ is the density of the fluid, ds is the length, g is the gravitation acceleration, z_1 and z_2 are the heights, and V_1 and V_2 are the velocities. In Equation (2.1), it is assumed that the flow between the inlet and outlet is compressible, unsteady and frictionless.

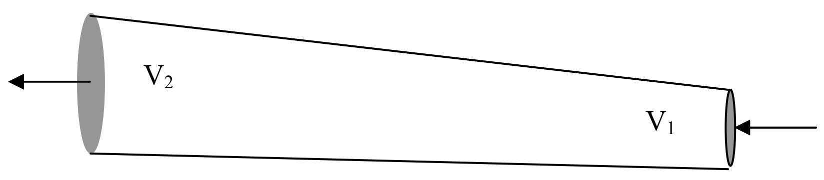

Figure 2.1 Flow in Pipe

For incompressible steady state flow, Equation (2.1) reduces to:

$$\frac{(P_2 - P_1)}{\rho} + \frac{1}{2}\left(V_2^{\,2} - V_1^{\,2}\right) + g\,(z_2 - z_1) = 0 \tag{2.2}$$

2.1.1 Bernoulli's Equation as Conservation of Energy

In modelling steady flow for pipe networks, normally the energy form of the Bernoulli's equation is used,

$$\frac{\mathrm{P}_1}{\rho} + \frac{1}{2}V_1^{\,2} + gz_1 = \frac{P_2}{\rho} + \frac{1}{2}V_2^{\,2} + gz_2 + \left[\sum_i f_i \frac{L_i}{D_i}\frac{V_i^{\,2}}{2}\right]_{friction\ loss} + \left[\sum_j K_j \frac{V_j^{\,2}}{2}\right]_{local\ loss} \tag{2.3}$$

where subscripts 1 and 2 are for upstream and downstream locations as shown in Figure 2.1, f is the friction factor, L is the length of the pipe, D is the diameter of the pipe, and K is the local energy loss factor. In this form the energy equation relates the pressure, velocity and elevation at different points of the flow, with the frictional and local losses.

In Equation (2.3), the first summation is the energy loss due to friction in pipes of different diameter and length and the second is the energy losses due to local disturbances to the flow. These could include local disturbances such as valves, elbows, and sudden constrictions and enlargements.

2.2 Energy Losses in Pipes.

Internal flow is constrained by bounding walls. There is an entrance region where a nearly inviscid upstream flow converges and enters the tube. Shown in Figure 2.2, for a long pipe, is a viscous boundary layer that grows downstream and retards the axial flow u (r,x) near the wall and thereby accelerates the flow at the centre (core flow) to maintain continuity (for incompressible flow). The total flow rate, Q, can be determined using:

$$Q = \int u \, dA = cont. \tag{2.4}$$

At a finite distance from the entrance, the boundary layers merge and the inviscid core disappears. The pipe flow is then entirely viscous, and the axial velocity adjusts slightly until x = L_e. After x = L_e, velocity no longer changes with x and is said to be fully developed. Downstream of x = L_e, the velocity profile is constant, the wall shear is constant, and the pressure drops linearly with x for either laminar or turbulent flow. This characteristic can be seen in Figure 2.2. The pressure drops shown in Figure 2.2 are due to the friction at the wall and thus the energy loss is called the friction loss.

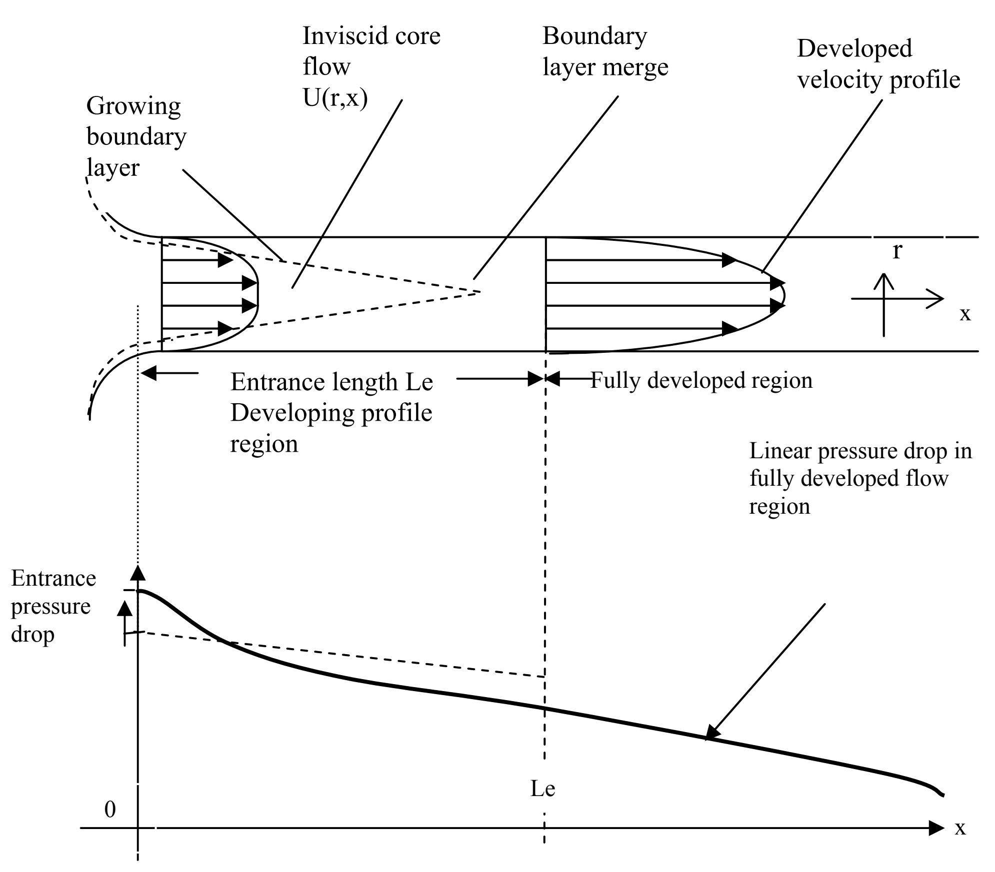

Figure 2.2 Developing velocity profiles and pressure changes in entrance of a pipe flow after White (1994)

2.2.1 Energy loss in pipes due to friction

In pipe flows, energy is lost due to friction at the pipe walls. The energy loss due to friction has to be calculated in order to know how much energy must be used to move the fluid.

The head loss due to friction can be expressed by Darcy's equation,

$$h_f = f \frac{L}{D} \frac{V^2}{2g} \tag{2.5}$$

where f is the friction factor. Different equations exist for friction factor f, depending on whether the flow is laminar or turbulent.

The shear stress will vary with the velocity of the flow; hence, the pressure loss due to friction will change accordingly. Janna (1993) states that in general the shear stress, τ_w, is very difficult to measure. However, for fully developed laminar flow it is possible to calculate a theoretical value for friction for a given velocity, fluid type and pipe dimensions using the Reynolds number (Re) without having to measure the shear stress.

$$f = \frac{64}{\mathrm{Re}} \tag{2.6}$$

where

$$\mathrm{Re} = \frac{VD\rho}{\mu} \tag{2.7}$$

For turbulent pipe flows, Blasius in 1913 (Watters, Street and Vennard, 1996) gave an empirical expression for the friction f as:

$$f = \frac{0.316}{\mathrm{Re}^{0.25}} \tag{2.8}$$

Equation (2.8) is reasonably accurate for Reynolds numbers between $4x10^3$ and 10^5 (Gerhart, Gross and Hochstein, 1992)

Von Karman and Prandtl in 1934 (Gulyan and Agrwal, 1996) provided an empirical correlation for determining friction factor for turbulent flow in smooth pipes as

$$\frac{1}{\sqrt{f}} = 2.0\log\left(\mathrm{Re}\sqrt{f}\right) - 0.8 \qquad (2.9)$$

This equation is valid for Reynolds numbers between $4x10^3$ and 80 $x10^3$ (Gulyan and Agrwal, 1996).

Equations (2.6), (2.8), and (2.9) do not cater for the effect of jet induction and the subsequent interference with the main flow. This naturally led us to examine the energy losses for the special condition caused by jet induction.

2.2.2 Local Head Losses

Local head losses occur in pipelines because of bends, T junctions, Y junctions, sudden enlargement, sudden contractions, and the like.

These losses are due to a phenomenon called Boundary Layer Separation. This often occurs whenever the flow experiences a positive pressure gradient in a direction of the flow, as for example when the flow is obstructed or impeded within the pipe. If the pressure rise is sufficient, the flow at the boundary will reverse, which results in large energy losses (Janna, 1993). When a flow reversal occurs, the boundary layer is lifted away from the surface as shown in figure 2.3.

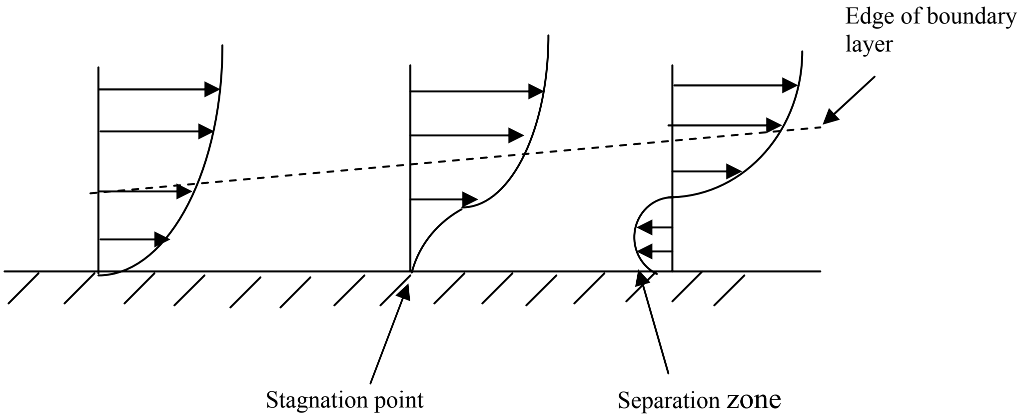

Figure 2.3 Boundary layer separation after (Potter and Wiggert, 2002)

Schasschke (1998) states that a general theory for local loss is not possible for all fittings and therefore the losses must be determined experimentally.

To calculate the local losses of fittings such as in a sudden enlargement, Robertson and Crowe (1985) state that such problems are normally not amenable to analytic solutions, but can be estimated with reasonable assumptions.

Consider the case of a sudden enlargement in a flow between points 1 and 2 as shown in the figure 2.4. Using Bernoulli's equation and the equations for momentum and continuity, Schasschke (1998) developed the expression for the local loss for a sudden enlargement as:

$$h_L = \left[1 - \frac{A_1}{A_2}\right]^2 \frac{V_1^2}{2g} \tag{2.10}$$

Thus h_L can be estimated by measuring V_1, for given areas A_1 and A_2.

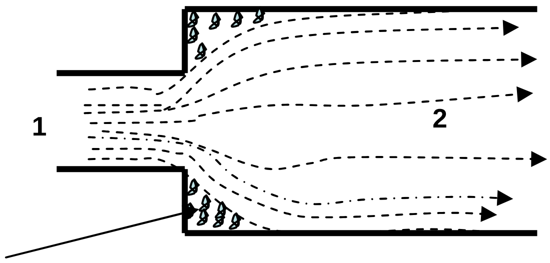

Figure 2.4 Sudden Expansion

Similarly, in a sudden contraction, where the flow contracts from point 1 to point 2 forming a vena contracta, the major losses occur as the flow expands after point 2.

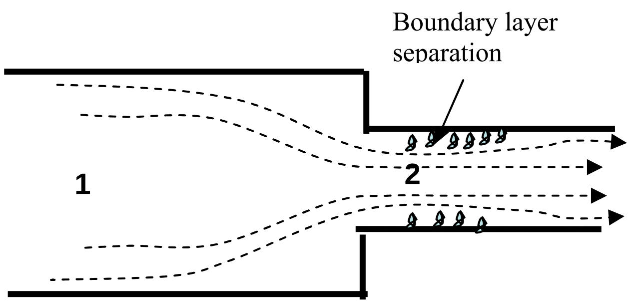

Figure 2.5 Sudden Contraction

Potter and Wiggert (2002) state that the local loss for sudden contractions can be approximated using equation 2.10, applied to the expanding flow from vena contracta to downstream.

For components such as T junctions and Y junctions, additional geometrical parameters are involved.

Miller (1990) states that the cause of major energy loss for T and Y junctions is due to the combination and division of flows, which arise from separation and subsequent turbulent mixing. Here the term ‘combining flow’ means flow entering from a branch pipe into the main pipe and ‘dividing flow’ means flow exiting from the branch pipe.

By numbering the flow paths as legs 1, 2, and 3 (leg 3 carrying the total flow) as shown in figures 2.6 and 2.7, Miller (1990) defines the loss coefficient, $K_{ij,}$ of T and Y junctions as

$$K_{ij} = \frac{\textit{total pressure in leg}_{\,i} - \textit{total pressure in leg}_{\,j}}{\textit{Mean pressure in leg 3}} \qquad (2.11)$$

According to Miller (1990), for sharp edged 90^0 ‘combining’ T junctions, with an equal cross sectional area in the branch and the main pipe, $\frac{A_1}{A_3}=1$, the loss coefficient K_{ij} is a function of $\frac{Q_1}{Q_3}$. From figure 2.8, considering zero branch flow, $\frac{Q_1}{Q_3}=0$, the pressure in the branch is essentially the static pressure of the main pipe.

Miller (1990) stated that if the pressure in the branch is raised slightly, a small flow will leave the branch and will be accelerated up to the velocity that is present downstream. This results in a transfer of energy from the upstream flow to the flow from the branch, therefore the loss coefficient for the branch as illustrated by Miller (1990) as negative. This is illustrated in figure 2.8.

Miller (1990) also suggested that in situations where the flow ratio $\frac{Q_1}{Q_3}$ is high and the area $\frac{A_1}{A_3}$ is low, a swirl is generated in the main flow due to an interaction with the branch flow. The swirling action interacts with the main flow causing turbulence, which then contributes to further energy losses.

In figures 2.6 and 2.7, the K subscripts illustrate the branch interactions for sharp edged 90^o and 45^o combing T and Y junctions.

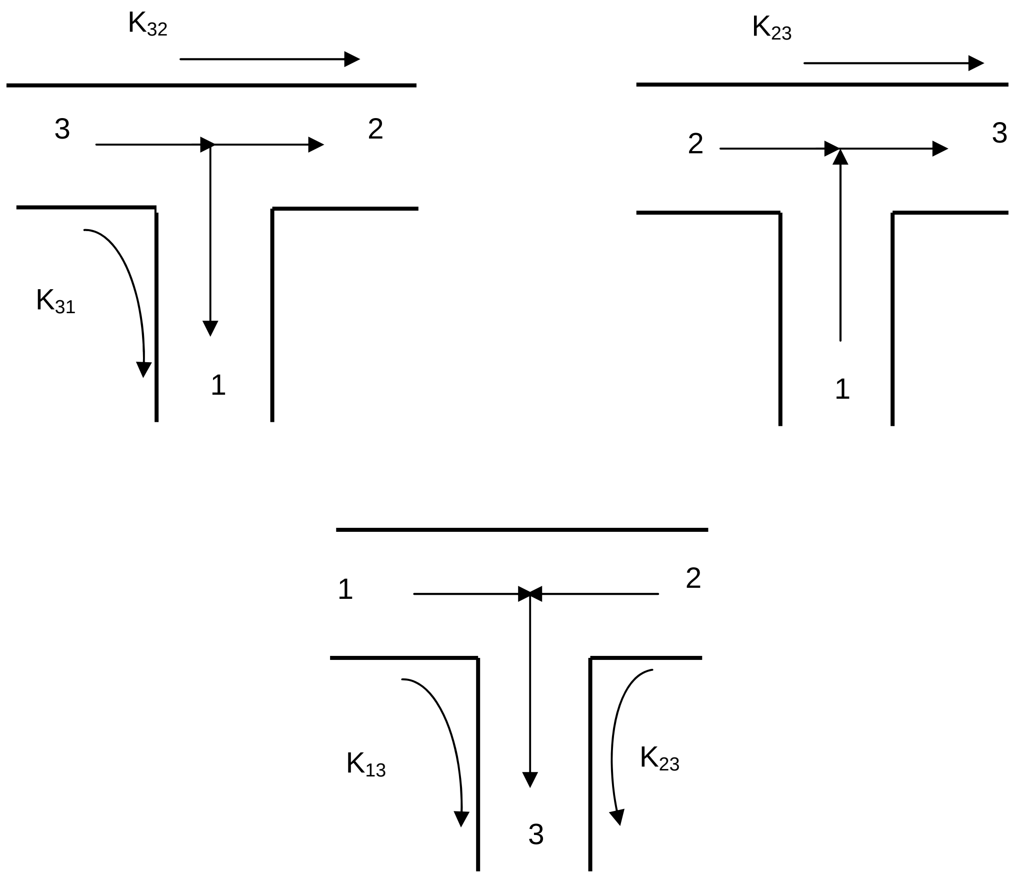

Fig 2.6 T junctions showing different flow paths after Miller (1990)

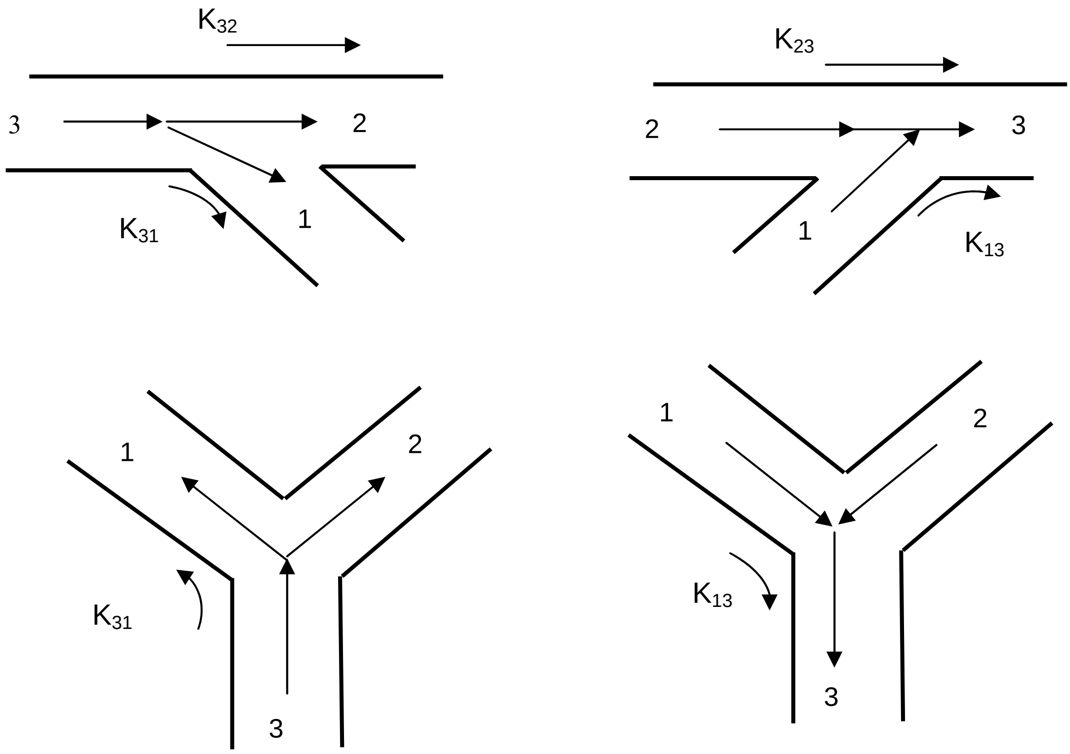

Fig 2.7 Y junctions showing different flow paths, after Miller (1990)

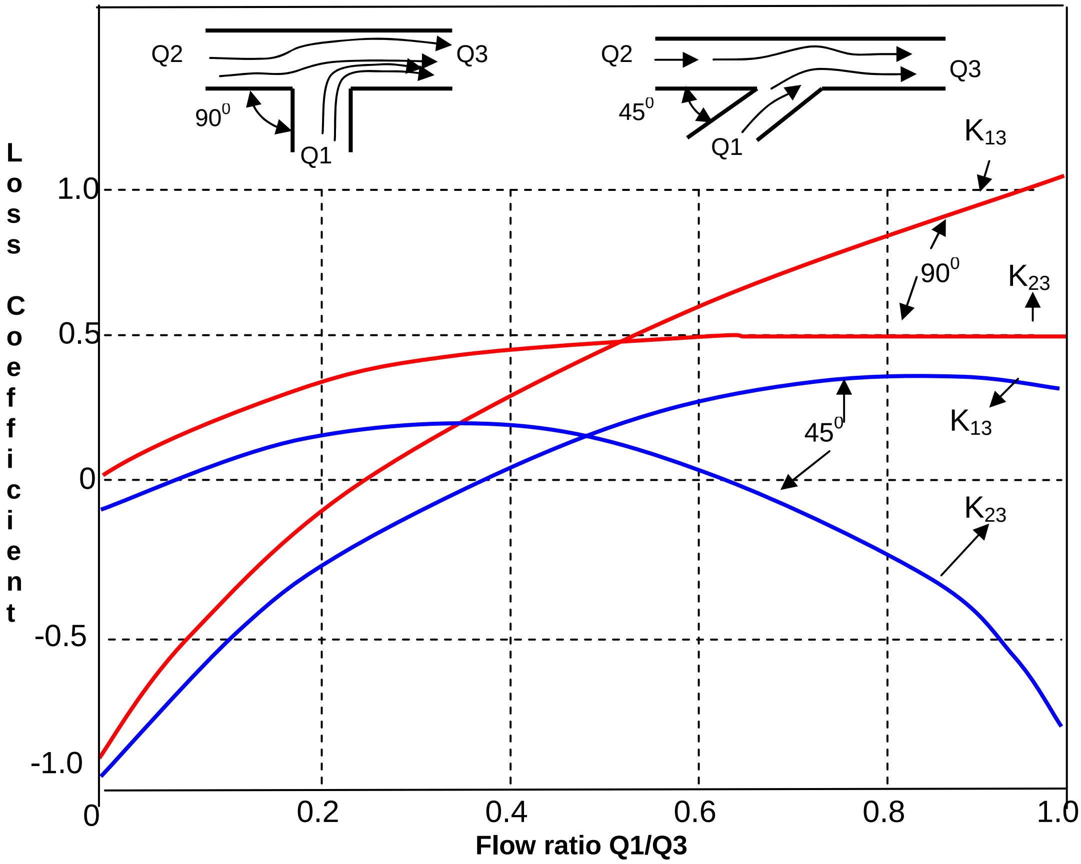

Fig 2.8 Loss Coefficient for sharp 45^0 and 90^0 combining junctions, with equal cross section area after Miller (1990)

Miller's (1990) equations for loss coefficients apply to sharp edged 90^0 T junctions and sharp edged 45^0 Y junctions. These geometries are not always possible with plastic moulded pipe joints such as the VESDA sampling pipes. In addition, the plastic pipe joints mostly have large openings at the ends, approximately the size of the outer diameter of the main pipe so that the main pipe can be inserted. The joint made at these ends cannot be pushed flush to the shoulder due to their design, resulting in an irregular flow path. This can be seen in figure 2.9.

The total local loss of such fitting (figure 2.9) is the sum of losses in A, B and C due to the geometry of the fitting, plus the loss due to turbulence caused by the mixing of the flow from the branch with the flow in the main pipe. The gaps between the pipe and T joints when inserted will always be. The reason is that the internal bores of T joints are made to have a slight taper. The reason for this is to ensure a tight fit. Therefore it is impossible to fit the pipes into the T joint flush to the shoulders.
It is therefore difficult to accurately calculate the loss coefficient of such fitting. Therefore, it is proposed to experimentally determine the loss coefficient of the T junction as well as all the fitting that are used in sampling pipe network.

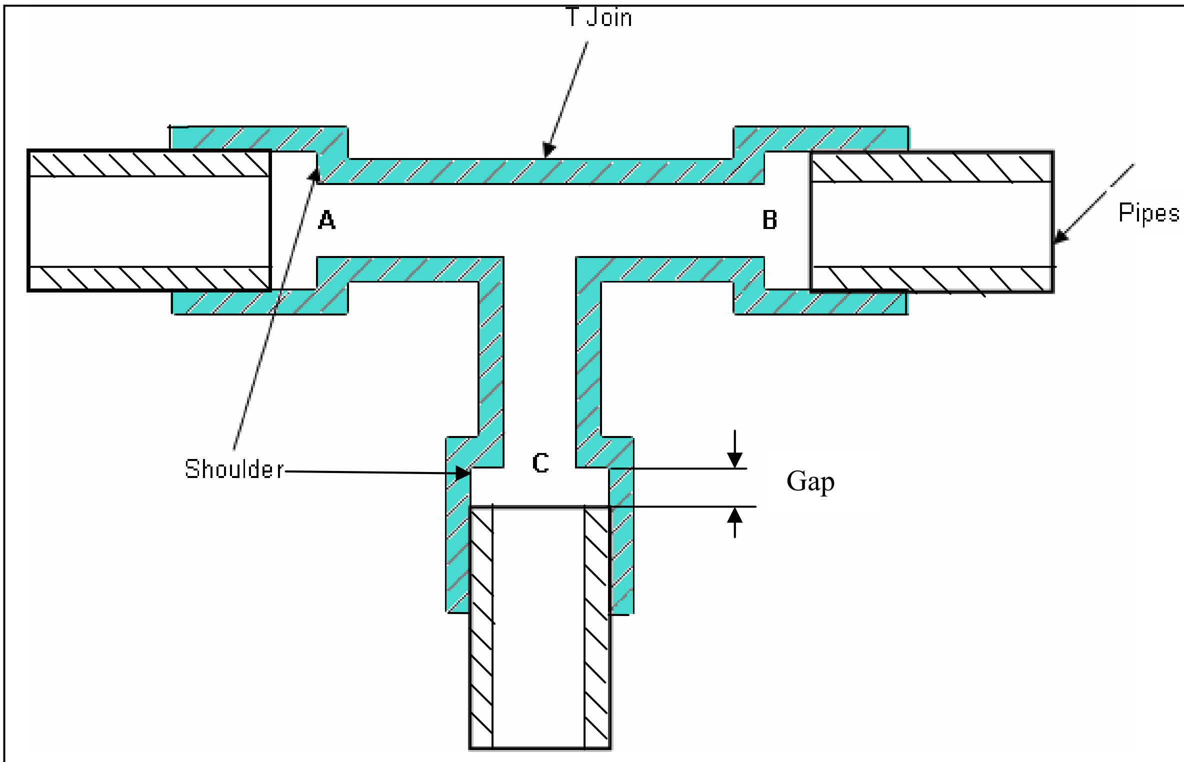

Figure 2.9 Showing the losses in T Join

2.3 Previous work on Aspirated Fire Detection Systems

Here the literature review will focus on the publications relating to aspirated fire detection systems. The analysis of the published materials will indicate the strengths and weaknesses of the current methods and clarify the needs and opportunities for further research.

2.3.1 Notarianni (1988)

Notarianni (1988) developed a mathematical model for a single pipe, 90m long with holes drilled 10m apart, for use in an aspirated smoke detecting system. Notarianni was employed by the Fenwal Corporation in USA at the time the model was developed. Notarianni's objective was to achieve "balance sampling" (i.e. the intake of air at an equal rate through each sampling hole). This can be achieved by increasing the diameter of the sampling hole along the pipe in the direction away from the detector to counter balance the decrease of local vacuum pressures due to energy loss.

Notarianni (1988) stated that since air would enter at equal rates through each hole, smoke entering in any single sampling hole would undergo equal dilution and thus would be detected at the same smoke concentrations. She suggested that the volumetric flow rate through a sampling hole could be described by

$$Q_{o,i} = CA_{o,i}\sqrt{2(P_{atm.} - P_{hole})/\rho} \tag{2.12}$$

Here Q is the volumetric flow rate, C is the coefficient for sampling holes, A_{oi} is the cross sectional area of sampling hole, P_{atm} is the atmospheric pressure, and P_{hole} is the internal pressure of the sampling hole.

The flow rate through each sampling hole is given as:

$$Q_{samplinghole} = \frac{\sum Q_{i,j}}{N_h} \tag{2.13}$$

N_h is the number of holes.

To find the flow in a pipe segment (here segment means the length of a pipe between sampling holes) and the pressure at the sampling hole, Notarianni (1988) assumed that the flow through all sampling holes is balanced (volume flow rates are equal).

Using this approach, Notarianni (1988) determined the flow rate in each segment of the pipe by counting the number of sampling holes upstream and downstream of that segment. She then calculated the pressure drop due to friction in each pipe segment using the Hagen-Poiseuille equation (White, 1994)

$$\Delta P = \frac{32\mu LV}{D^2}. \tag{2.14}$$

Here ΔP is the pressure drop along the length of pipe segment and D is the pipe diameter.

To this pressure drop, Notarianni (1988) added the pressure drop due to bends, filters and other fittings along the segment close to the sampling hole. She stated in her analysis that once the suction pressure in a sampling hole is known, the diameter of the hole necessary to achieve the flow rate can be calculated, by rearranging Equation (2.12) in terms of hole diameter.

$$d = \sqrt{\frac{4Q}{\pi C\sqrt{2(P_{atm.} - P_{hole})/\rho}}} \tag{2.15}$$

Here d is the diameter of the sampling hole.

Notarianni (1988) made assumptions throughout her analysis that the flow in the pipe is laminar. Our previous investigations at Vision System Limited showed that this was not achievable even at low Reynolds numbers due to the various disturbances to the flow. Notarianni (1988) also assumed equal flow rate in all the sampling holes. During a preliminary investigation, it was found that the flow rate is very sensitive to the diameter of a particular sampling hole. Practically, it is very difficult to drill a hole (normally done using a hand held power drill) to within ± 0.25 mm of the specified diameter. Given that the normal diameter of the sampling hole is only 2mm, this can result in large errors in the cross-section area of the sampling hole.

Because the air velocity entering the sampling hole is much higher than that in the main sampling pipe, this uncertainty in the diameter of the sampling hole makes the balance of flow rate in each sampling hole impractical. Although Notarianni (1988) determined the pressure losses in a pipe using the commonly used equations such as the Hagen-Poiseuille equation for friction loss, local loss coefficients for holes and bends determined experimentally, she did not take into account the loss due to jet induction.

Her equation to calculate the transport time is $T_{transport} = \sum \frac{\Delta L}{V}$, where ΔL is the length of a segment, and V is the velocity of air in the segment. Previous investigations have shown that this equation for transport time only applies when there are no sampling holes. It does not apply when the main flow is continuously disturbed by the jets of air from sampling holes, which consequently has an effect on the velocity of the main flow. This implies that the losses that occur during the region of disturbed flow and the region of fully developed flow need to be considered.

Furthermore, Notarianni (1988) only considered a straight single pipe. She did not mention branched pipe systems, the use of capillary tubes and ceiling rose fittings, or pipe couplings. These are the most commonly used fittings in VESDA installations and are the major contributors to pressure losses and transport time.

2.3.2 Taylor (1984)

Taylor (1984) mathematically modelled the airflow through sampling pipes. Taylor (1984) begins by stating that for a steady incompressible fluid flow through a smooth pipe, the energy conservation equation can be used. He quoted Darcy's formula for head loss in pipes caused by friction.

He also commented that this equation is applicable to either laminar or turbulent flow. To obtain friction factor f for laminar flow Taylor (1984) used equation (2.6). For turbulent flow he used equation (2.8)

Additionally, Taylor (1984) stated that there will be losses due to friction in bends and fittings.

To characterise the flow through the sampling holes Taylor (1984) derived the following equations from a series of published empirical graphs. These relate to the inflow and outflow respectively where R_i is the flow ratio of the sample and main flows.

$$K_{in} = 2.053R_i - 2.473R_i^2 + 0.9796R_i^3$$
$$K_{out} = 0.07369R_i - 1.375R_i^2 + 5.319R_i^3 - 5.151R_i^4 + 0.646R_i^5 \qquad (2.16)$$

To calculate the pressure drop in a segment, Taylor's modified equations can be written as:

$$\Delta P_{segment} = \left(K + f\frac{L}{d} + K_{in} + K_{out} \right) \rho \frac{V^2}{2g} \qquad (2.17)$$

where K is the local loss coefficient.

To calculate the transport time, Taylor (1984) assumed that smoke travels at the mean air velocity using the same equation as Notarianni (1988).

Taylor (1984) did not state the values for the local loss coefficient for the bends and fittings. Taylor's equations for K_{in} and K_{out} are not clearly defined as to how he collected the data to derive the equations. And, it is not clear what he means by outflow (K_{out}) since air only flows in from all sampling holes during the normal operating conditions of the smoke detector.

However, it seems that Taylor (1984) did realise that when the main flow is disturbed by the jets from the sampling hole, they contribute to the loss. This is evident from equation (2.16) where one of the loss coefficient is K_{in}.

Similar to Notarianni, Taylor (1984) did not mention the use of capillary tubes or ceiling roses.

Taylor wrote a computer programme using the equations for VESDA pipe systems, but Vision Systems Ltd (manufacturer of VESDA smoke detector) did not use it as a simulating tool. It was suggested that the accuracy of the results were not to the required standard.

2.2.3 Cole (1999)

Cole (1999) investigated the disturbances to pipe flow regimes by jet induction to improve the available techniques to mathematically model the performance of aspirated smoke detection systems. He stated that there is a significant area of uncertainty in determining the friction factor and it has not been established that the friction factor is unaffected by upstream disturbances to the flow regime whether that regime is turbulent, laminar or transitional. He suggested that the assumption that the flow regime can be regarded as fully developed may not be true.

Similar to the work carried out by Taylor (1984), Cole (1999) suggested that the energy losses in any pipe fitting can be broken down into three components: entry loss, exit loss and friction losses. He stated that for an orifice that has square shoulders, the entry loss coefficient is 0.5 and the exit loss coefficient is 1. Cole (1999) suggested that the energy loss for a sampling hole can be calculated as

$$h_l = C_{entry}\frac{V^2}{2g} + f\frac{L}{d}\frac{V^2}{2g} + C_{exit}\frac{V^2}{2g} \tag{2.18}$$

Here h_l is the energy loss, C_{entry} and C_{exit} are the coefficients of local energy losses in entry and exit respectively.

Cole (1999) determined the friction factor *f* for the VESDA sampling pipe, which has a 21mm internal diameter and 4 metres in length, using Darcy's equation (White, 1994)

$$f = \frac{2\Delta PD}{\rho LV^2} \tag{2.19}$$

By measuring the pressure and flow rate in the pipe, he calculated the friction factor *f*.

Cole (1999) correlated the data on various flow rates and plotted friction factors versus Reynolds numbers. Using an Excel spreadsheet, Cole (1999) obtained some empirical relationships for the friction factor *f*.

Using a similar method, Cole (1999) determined the friction factor for a socket (pipe coupling), and the effect on the friction factor when a fully developed flow is disturbed by a jet induction.

Cole (1999) illustrated the friction factor as a function of flow for different regimes, as:

f =64/Re if Re < 2280
f = 0.028 if 2280 < Re < 2400
f = 0.028 +0.007 (Re – 2400)/600 if 2400 < Re < 3000
f = 0.035 + 0.004 (Re – 3000)/800 if 3800 <R e< 4400

To calculate the transport time, Cole (1999) stated that a significant proportion of smoky air is entrained within the central core of pipe flow, therefore the core velocity dominates any measurements of smoke transport time.

Cole (1999) considered the boundary layer theory to determine the effect of the disturbance on velocity profiles. He stated that for the boundary layer to approach the centreline asymptotically, the equation has to be the form of

$$B = \frac{D}{2}(1 - e^{-\frac{S}{s}}) \qquad (2.20)$$

Where *B* is the boundary layer thickness, *S/s* is the displacement ratio, *D* is the pipe diameter.

Cole (1999) stated that, for equation (2.20) to asymptote to 99% of its final value, the displacement ratio *S/s* needs to be 4.6. The shape of the curve of equation (2.20) is represented in figure 2.19. It can be seen that the point where the boundary layer thickness is 99% of the pipe radius, the displacement from the entry is 120*dia.*

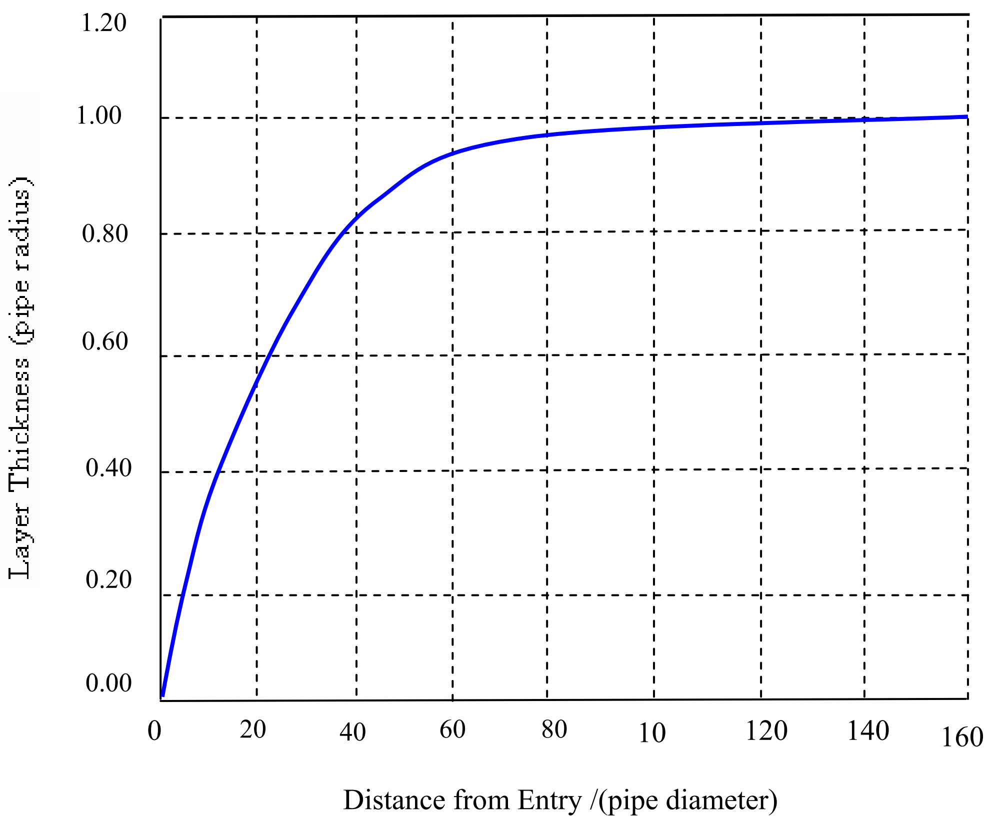

Figure 2.19 Exponential model of boundary layer growth, after Cole (1999)

Cole (1999) decided to adopt the exponential model, being directly related to boundary layer thickness and core velocity growth curve as a function of mean velocity.

For core velocities at the pipe entry and at the entry length (length at which the flow is fully developed), Cole adopted the equations

the pipe entry $$V_{core} = V_{mean}(1+(1-e^{-0})) = V_{mean} \tag{2.21}$$

At the entry length $$V_{core} = V_{mean}(1+(1-e^{-4.6})) = 1.98V_{mean} \tag{2.22}$$

Cole (1999) stated earlier that the exponent must reach the value 4.6 at 120*dia*; therefore, the equation for core velocity growth becomes:

$$V_{core} = V_{mean}(2 - e^{-\frac{-S}{26}}) \tag{2.23}$$

$$S = \frac{x}{D}$$

where x is the distance from the pipe entrance.

To obtain the time delay for a given package of air travelling at a local velocity *(V)* over an infinitesimal pipe displacement *(ds),* Cole derived a differential equation for time delay *(dt);*

$$V = \frac{dx}{dt} \tag{2.24}$$

$$dt = \frac{dx}{V}$$

By substituting the core velocity equation (2.23), Cole (1999) obtained an integral for elapsed time over a displacement L

$$T_{lam} = \int_0^L \frac{dx}{V}$$

$$= \int_0^L \frac{dx}{V_{mean}(2 - e^{\frac{-s}{26}})}$$

$$= \int_0^{\frac{L}{D}} \frac{Dds}{V_{mean}(2 - e^{-\frac{s}{26}})}$$

$$= \frac{D}{2V_{mean}} \left[\frac{L}{D} + 26\ln(2 - e^{\frac{-L}{26D}}) \right]$$

Cole (1999) expressed equation (2.25) in terms of velocity ratio (V_r), where

$$V_r = V_{core}/V_{mean} \tag{2.25}$$

$$T_{lam} = \frac{L + 26D\ln\left[(V_r - (V_r - 1)e^{\frac{-L}{26D}}\right]}{2V_{mean}} \tag{2.26}$$

Here T_{lam} is the transport time in a segment calculated when the flow is laminar.

Similarly for turbulent flow in a segment Cole (1999) derived the equation as

$$T_{tur} = \frac{D}{1.3V_{mean}}\left[\frac{L}{D} + 13\ln(1.3 - 0.3e^{\frac{-L}{13D}})\right] \tag{2.27}$$

$$T_{tur} = \frac{L + 13D\ln\left[(V_r - (V_r - 1)e^{\frac{-L}{13D}}\right]}{1.3V_{mean}} \tag{2.28}$$

Here T_{tur} is the transport time in a segment when the flow is turbulent.

Throughout the experiments undertaken to confirm the transport time estimates, Cole (1999) used an inline flow meter, which became part of the system being analysed. This introduces additional errors due to its frictional and local losses. Cole (1999) could have minimised these additional errors by using a Pitot tube which would not have added significant measurement error to the system under analysis.

To determine the energy losses in fittings, Cole (1999) concentrated more on losses due to friction than losses due to local disturbances. Losses due to local disturbances are more significant in a short pipe segment. The local energy losses in fittings differ from one type to another; therefore, all different types of fittings used in VESDA installations should be characterised.

In his experiments, Cole (1999) used only one single fitting to determine the flow rate for his calculation and compared this result with the results obtained in a pipe without any fittings. The instrument that he used was not sensitive enough to be able to capture the difference in flow with and without the fitting. Cole (1999) could have used a large number of similar fittings to determine the energy loss due to the same type of fitting to increase the comprehensiveness of the experiments.

Cole's equations (equations 2.27 and 2.28) for transport time have their merits when calculating the transport time in a straight pipe, having no more than 4 elbows in each pipe and without a capillary tube. However, since the equations are a function of flow and the development of a boundary layer, further research should have been done.

The modelling software currently used by VESDA, known as ASPIRE®, was developed using Cole's (1999) theory. As discussed earlier, the current ASPIRE® modelling software cannot predict accurately enough (within 90%) the measured transport time or the pressure at the sampling locations, especially when capillary tubes are used as an extension from the main pipe.

The ASPIRE® software requests data regarding the capillary tubes, but actually does not calculate the suction pressures at the ceiling rose, which is an attachment to the capillary tube on which a sampling hole is drilled. Consequently, the transport times and suction pressures predicted in such installations are not correct. Depending on the length of the capillary tubes, the errors can be more than 20%.

The ASPIRE® program also limits the number of bends in an installation. If more than 4 bends are used, the errors begin to increase. The ASPIRE® program does not have an algorithm to simulate a branched network.

As a result of this survey, it is believed that no detailed research has been done into the effects of disturbance due to jet induction, or its effect on the friction coefficient or the consequent pressure loss.

This provides both a need and opportunity for further research where the effects of a disturbance due to jet induction can be determined and mathematical equations derived which can then be programmed in order to predict more accurate results.

Further work is also required to determine the local loss coefficients of all the fittings used by VESDA for installations and the losses which occur at the ceiling rose when a capillary tube is used.

CHAPTER 3

EXPERIMENTAL APPARATUS AND METHODS

Components (fittings) used within an aspirated smoke detection system need to be accurately characterised in terms of energy losses. Numerous tables for loss coefficients of various fittings are available in textbooks such as Potter and Wiggert (2002), but these data are empirical, and therefore may be subjected to experimental conditions and geometry. Such data can only be used as a guide. Given that high accuracy for predicting the VESDA smoke detecting system is required, it is necessary to experimentally determine the loss coefficient for each type of component that may be used in an installation.

The sampling pipes and fittings used in the U.S.A. and U.K. are different in diameter and design, and thus the K values for these fittings need to be determined as well.

The central feature and driving force within an aspirated smoke detection is the aspirator itself, which must be accurately characterised. For any given setting of aspirator speed, it is necessary to determine the inlet vacuum pressure throughout the complete range of flow rates.

To capture the relevant data accurately, it is imperative that the equipment used and the methods applied are appropriate so that the existence of the apparatus as part of the experiment does not affect the data obtained.

This chapter describes the experimental apparatus, experimental set up and methods applied to collect the data to determine the loss coefficient of all fittings and the data to characterise the aspirator. Figure 3.1 is a schematic diagram for the experimental setup to determine the local loss coefficient of coupling join. Mathematical expressions for the aspirator characteristics are then developed.

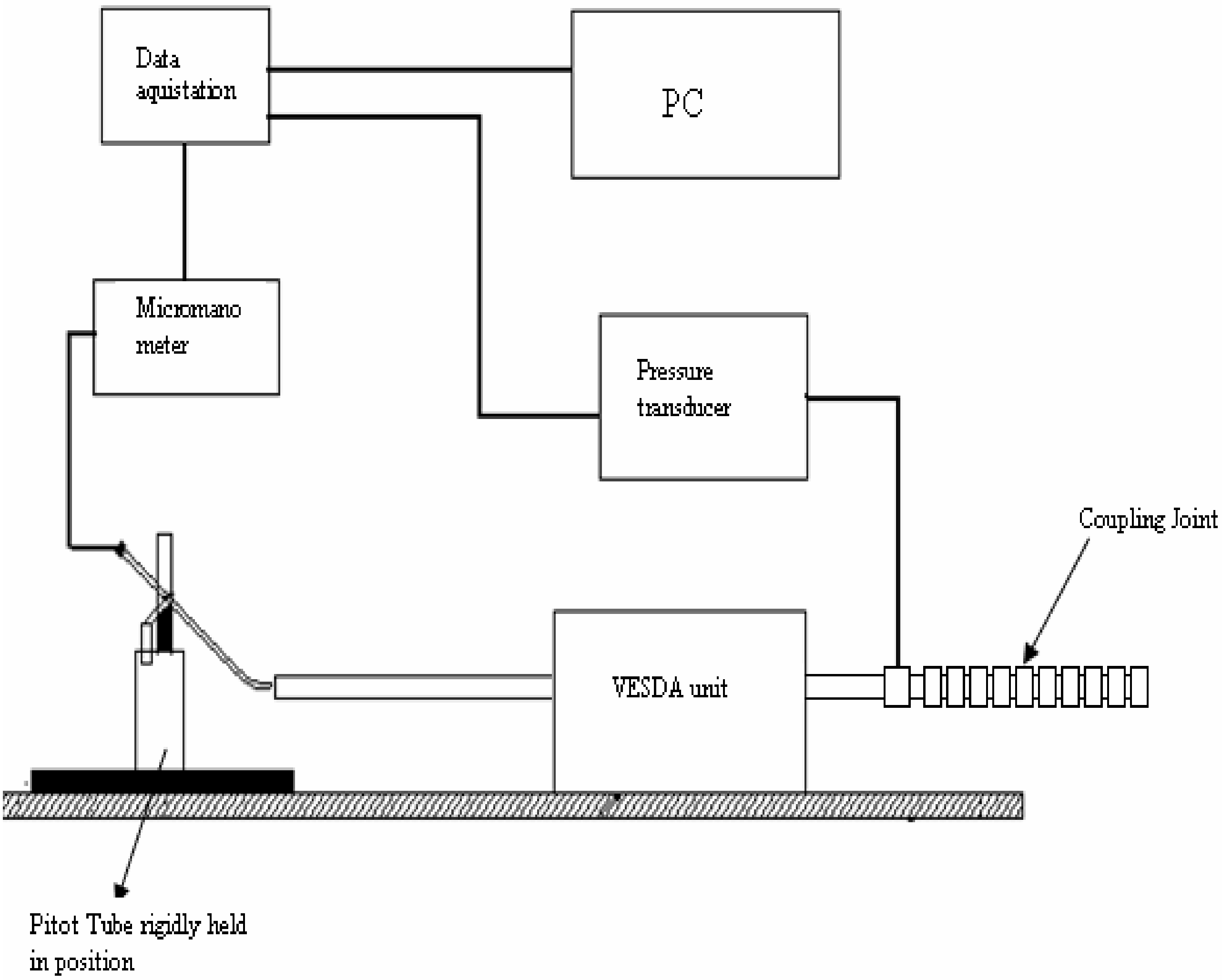

Figure 3.1 Experiment set up to determine the local loss coefficient of coupling joint

3.1 Instruments

3.1.1 Pressure Transducer

The pressure transducer shown in figure 3.1 to determine the static negative pressures was a Furness Controls Ltd. Micromanometer, model MDC FM 497. The pressure transducer is capable of reading pressures from 0 to 1000 Pa, with a resolution of 0. 1 Pa.

3.1.2 Flow meter

The flow meter used in the experiments was a Furness FC096-200L, laminar plate flow meter complete with a FC016 digital manometer calibrated in litres/minute. The flow meter was zeroed at the beginning of each experiment by blocking the flow. The flow meter was used only to calibrate the position of the Pitot tube (to be discussed later). Once the position of the Pitot tube was determined, the flow meter was removed.

3.1.3 Pitot Tube and Micromanometer

The micromanometer used in the experiment was a model MDC FM 497 from Furness Controls Ltd.

A Pitot tube and micromanometer were used in the experiments to measure the outlet velocity of air from the exhaust port of the VESDA system. Having obtained the velocity, the flow rate was calculated.

A Pitot tube, when aligned with the flow, measures the local velocity by means of pressure difference. It has side holes to measure the static pressure P_s in the moving stream and a hole in the front to measure the stagnation pressure P_o, separately. The difference in the pressures (P_s - P_o) measured by the micromanometer and the velocity (V) are determined by using the equations:

$$P_s - P_o = \frac{1}{2}\rho V^2 \tag{3.1}$$

$$V = \sqrt{\frac{2(P_s - P_o)}{\rho}} \tag{3.2}$$

The main reason to use the Pitot tube in the experiments was that it does not impede the upstream flow of the apparatus under test and therefore does not contribute to any significant errors.

3.2 Experimental set up

3.2.1 Positioning of the Pitot tube

As shown in figure 3.1, a 1.5m long, 21mm diameter PVC pipe, which is the commonly used VESDA pipe, was attached to the exhaust of the unit. The 1.5m pipe was used to stabilise the flow so that the flow can be fully developed by the time it reached the Pitot tube. The pipe and the VESDA unit used were fixed in position. The unit was switched on and the reading of the flow meter (l/min) and the Pitot tube (velocity m/s) were recorded. The flow was calculated using the velocity reading of the Pitot tube. The position of the Pitot tube was adjusted (i.e. moved vertically or horizontally) until the reading of the flow meter was in agreement with the flow rate calculated using the velocity V from the Pitot tube.

$$Flowmeter\ reading\ (l/\min) = \frac{\pi D^2}{4}V \tag{3.3}$$

Here D is the internal diameter of the PVC sampling pipe. Once the flow rate calculated using equation (3.2) matched with that from the flow meter, the Pitot tube was locked in position.

3.2.2 Local loss coefficient (K) of the fittings.

Once the Pitot tube is locked in position, the flow meter is removed. To determine the local loss coefficient *K*, ten identical fittings of each type were connected to the inlet of the VESDA detection unit as shown in figure 3. (Only the coupling fittings are shown). A measurement of the pressure loss across a single fitting yields large uncertainties and also having pipe between multiple fittings introduces additional frictional losses. Therefore the only reasonable way is to connect multiple fittings with negligible pipe lengths. Using ten fittings together, an average local loss coefficient can be determined. The *K* is determined as

$$K = \left[\frac{\Delta P \times 2}{\rho \times V^2}\right] \times \frac{1}{N} \tag{3.4}$$

V = velocity of air taken from Pitot tube, N = number of fittings and ΔP is the pressure difference across the fittings.

3.2.3 Results for fitting loss

Item	Australian pipe fittings	U.K pipe fittings	U.S.A. pipe fittings	Text book values
large bend	0.83	*	*	0.16
medium bend	0.97	*	*	0.19
small bend	0.84	*	*	0.35
90°sharp bend	*	0.48	1.04	1.1
45° bend	*	0.41	0.67	0.32
pipe coupling	0.34	0.15	0.31	**
Threaded coupling	*	*	0.31	**
Y-branch	1.94	*	*	0.8
T-branch	2.13	1.87	3.10	1.8
2 or 3 mm sampling hole	1.00	1.00	1.00	**
Ceiling rose	2.00	2.00	2.00	**

Table 3.1 Local Loss coefficients of fittings

Table 3.1 lists the local loss coefficients of different fittings and the corresponding values from the text book, (White, 1994). In table 3.1, * means the type of fitting is not used, e.g. a large bend is used in Australian pipe systems but not in U.K. and U.S.A pipe systems and ** means the loss coefficient is not found in text books.

It can be seen from table 3.1 that while there are some fittings close to the text book values, there exists a significant variation between specific fittings. Therefore using text book values is not adequate. The differences between the text book values and measured values are dominated by the shape of the internal geometry of the fittings which is not considered in the text book. A fitting having higher impedance to flow results in higher value loss coefficient. This phenomenon is explained in chapter 2, Section 2.2.2, Figure 2.9.

Table 3.2 shows the pictorial view of the various fittings in table 3.1.

large bend	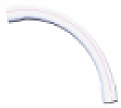
Medium bend	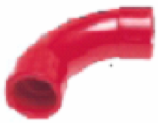
90°sharp bend	
45° bend	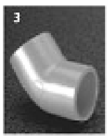
pipe coupling	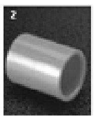
Threaded coupling	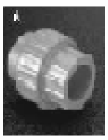

Y-branch	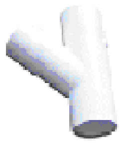
T-branch	
Ceiling rose	
2 or 3 mm sampling hole	

Table 3.2 Pictorial view of the fittings

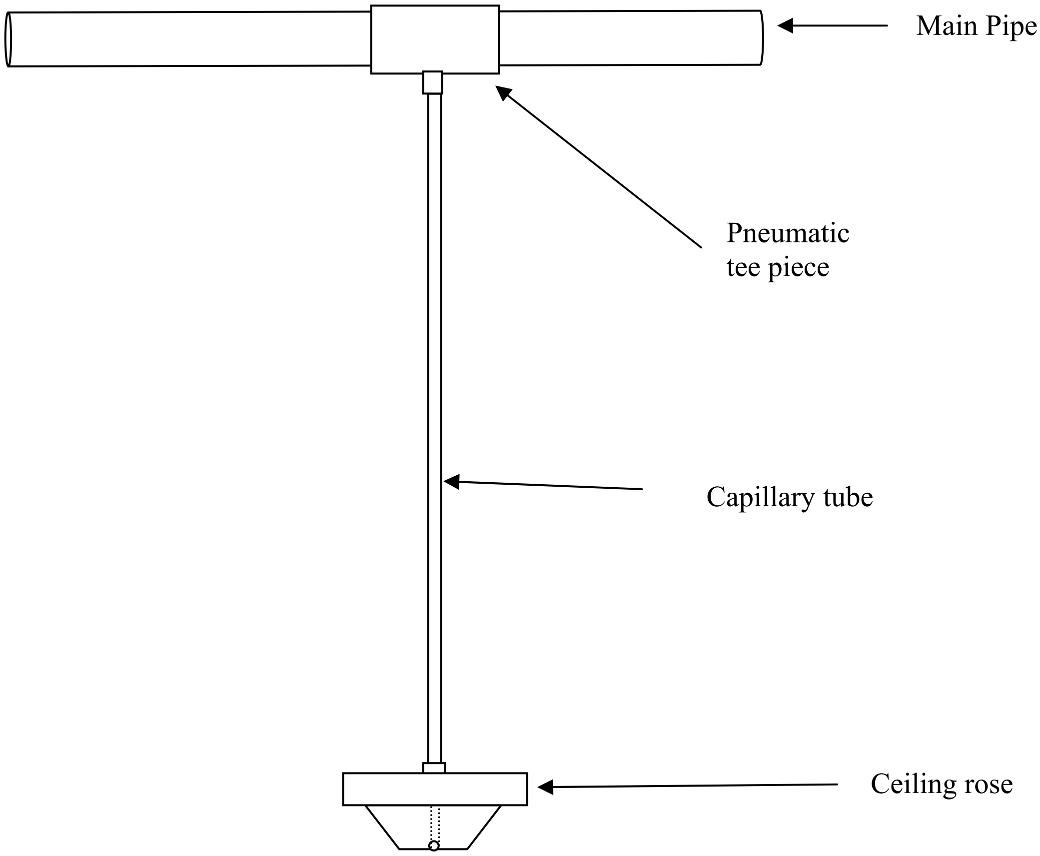

Fig 3.2 A capillary tube set up

3.2.4 Pressure Loss in Capillary Tube

A capillary tube in the VESDA smoke detection system consists of a pneumatic T junction, a 5.1mm diameter capillary tube, and a ceiling rose. Figure 3.2 shows a typical capillary tube setup.

Since there is no disturbance of the flow by jet induction in a capillary tube and the Reynolds number is low (less than 2000) the flow is considered to be laminar.

The local loss occurs at the sampling hole (ceiling rose), the transition from ceiling rose to capillary tube and the transition from capillary tube to the main pipe. In both cases the loss coefficients have been experimentally determined as 2.0, as can be seen from table 3.1

The velocity of air in the capillary tube is considered necessary to calculate the transport time of the smoke (discussed in the later chapters).

From equation (2.3)

$$\frac{\Delta P}{\rho g} = (f\frac{L_{CT}}{D_{CT}} + K_1 + K_2)\frac{V_{CT}^2}{2g} \tag{3.5}$$

Here L_{CT} is the length of the capillary tube, V_{CT} is the air velocity in the capillary tube, D_{CT} is the inside diameter of the capillary tube, K_1 is the loss coefficient of the ceiling rose, K_2 is the loss coefficient where the capillary tube joins the main pipe, ΔP is the pressure drop in the ceiling rose and ρ is the density of air.

The friction factor *f* in the capillary tube is calculated using equation (2.7)

$$f = \frac{64}{\text{Re}}; \qquad \text{Re} = \frac{\rho V_{CT} D_{CT}}{\mu} \tag{3.6}$$

Here V_{CR} stands for velocity of air in the capillary tube and D_{CR} is the diameter of ceiling rose, Q_{CR} is the flow in the ceiling rose and Q_{CT} is the flow in the capillary tube.

From continuity $Q_{CR} = Q_{CT}$

$$V_{CT} A_{CT} = V_{CR} A_{CR}$$

$$V_{CR} = V_{CT}\left(\frac{D_{CT}}{D_{CR}}\right)^2$$

$$V_{CR}^2 = V_{CT}^2\left(\frac{D_{CT}}{D_{CR}}\right)^4 \tag{3.7}$$

Here $D_{CT} = 5.1mm$ and $D_{CR} = 2mm$.

The pressure loss in the ceiling rose due to local loss can be calculated by the equation

$$P_{loss} = K_1 \frac{V_{CR}^2}{2} \rho \tag{3.8}$$

From equation (3.7)

$$= K_1 \frac{V_{CT}^2}{2} \left(\frac{D_{CT}}{D_{CR}} \right)^4 \rho \tag{3.9}$$

From equation (3.5)

$$\Delta P = \left[\left(\frac{64}{\mathrm{Re}} \times \frac{L_{CT}}{D_{CT}} \right)_{friction} + \left(K_1 \left(\frac{D_{CT}}{D_{CR}} \right)^4 + K_2 \right)_{local} \right] \times \frac{V_{CT}^2}{2} \times \rho \tag{3.10}$$

$$= \left[\left(64 \times \frac{\mu}{\rho V D_{CT}} \times \frac{L_{CT}}{D_{CT}} \right) + K_{rose} \right] \times \frac{V_{CT}^2}{2} \times \rho$$

$$\frac{K_{rose}}{2} \rho V_{CT}^2 + \frac{32 \mu L_{CT} V_{CT}}{D^2{}_{CT}} - \Delta P = 0 \tag{3.11}$$

Here

$$K_{rose} = K_1 \left(\frac{D_{CT}}{D_{CR}} \right) + K_2$$

In this experiment $K_{rose} = 86.57$

Using the quadratic equation formula:

$$V_{CT} = \frac{ \frac{-32 \mu L_{CT}}{D_{CT}^2} + \sqrt{ \left(\frac{32 \mu L_{CT}}{D_{CT}{}^2} \right)^2 + 2 K_{rose} \rho \times \Delta P } }{ K_{rose} \times \rho } \tag{3.12}$$

The transport time in the capillary tube can be calculated using;

$$T_{CT} = \frac{L_{CT}}{V_{CT}} \tag{3.13}$$

Here T_{CT} is the time for smoke to travel from ceiling rose to the main pipe, V_{CT} is the velocity in the capillary tube, and L_{CT} is the length of capillary tube in meters.

The pressure drop in the ceiling rose can be calculated by using the Hagen –Poiseuille equation as;

$$P_{CR} = \left[\frac{32\mu L_{CT} V_{CT}}{D^2{}_{CT}}\right] - P_{main} \tag{3.14}$$

Here P_{main} is the pressure in the main pipe where the capillary tube is connected and P_{CR} is the pressure drop in the ceiling rose. This equation is used in later chapters.

3.3 Mathematical Expressions of Pressure versus Flowrates for VESDA Aspirator

VESDA smoke detector range includes the VESDA LaserPlus (figure 3.3) (VLP), the VESDA Laser Scanner (figure 3.4) (VLS), and the VESDA Compact (figure 3.5) (VLC). All VESDA units work in the same principle as described in section 1.2.

There are a number of possible aspirator speed settings for each model. The speeds can range from 3000 rpm to 4200rpm for VESDA Laser Plus (VLP) unit.

Similar speed settings are achievable for the VLS unit. However, this unit has butterfly valves in the manifold (see in figure 3.8). The unit goes to scan mode once smoke is detected to determine the zone (pipe) from which smoke is coming. During the scan mode only one butterfly valve is open at a time and the air is sampled for smoke. The port that has the highest smoke concentration is deemed to be the potential smoke/fire zone.

The presence of butterfly valves in the main stream has a significant impact on the air flow; hence, the characteristics of the aspirator will be different from the VLP.

The VESDA Compact (VLC) is a smaller version of a VLP, which runs at a constant speed of 2800 rpm. The air passage of the VLC is quite different to the other units. Therefore, a VLC also needs to be characterised separately.

The characteristics of each model need to be obtained. Since the physical designs of the units are unique, the experimental set up requires separate configurations to capture the relevant data of the aspirator characteristics.

Figure 3.3 VESDA laser Plus (VLP)

Figure 3.4 VESDA Laser Scanners (VLS)

Figure 3.5 VESDA Laser Compact (VLC)

3.3.1 Experimental set up to characterise the VLP aspirator

Figure 3.6 shows the experimental set up to capture the pressure and flow of the VLP aspirator at different flow rates and speeds.

The Pitot tube senses the air velocity from the exhaust of the VLP unit by means of the pressure difference. The analogue signal is processed by a data acquisition card. The flow rate through the manifold was calculated using the expression;

$$Q = V \times A$$

where Q is the flow rate, V is the mean air velocity as calculated using Equation (3.2), and A is the cross sectional area of the exhaust pipe. Similarly the pressure drop in the manifold was sensed by the pressure transducer which sent analogue signals to the data acquisition card and was recorded. The flow rates were varied by changing the hole diameters in the end caps. The diameters of the holes used were 4mm, 6mm, 8mm, 10mm, 12mm, 14mm, 16mm, 18mm, and 21mm (fully open end). Mathematical expressions for aspirator characteristics were developed over different speed range and flows rates.

3.3.1.1 Steps taken to determine aspirator performance at different speeds and flow rates

The equipment was setup the same way as that shown in figure 3.6. The aspirator speed was set to 3000 rpm and an end cap with a 4mm diameter hole was fixed to the intake
of a 21mm PVC pipe initially. Hole diameters were then changed to 6, 8, 10, 12, 14, 16, 18 and 21mm respectively for different flow rates. Pressure drop and velocity readings were recorded for all the restrictors. This procedure was repeated with aspirator speeds set at 3400 rpm, 3800 rpm and 4200 rpm, respectively. All together thirty six measurements were taken.

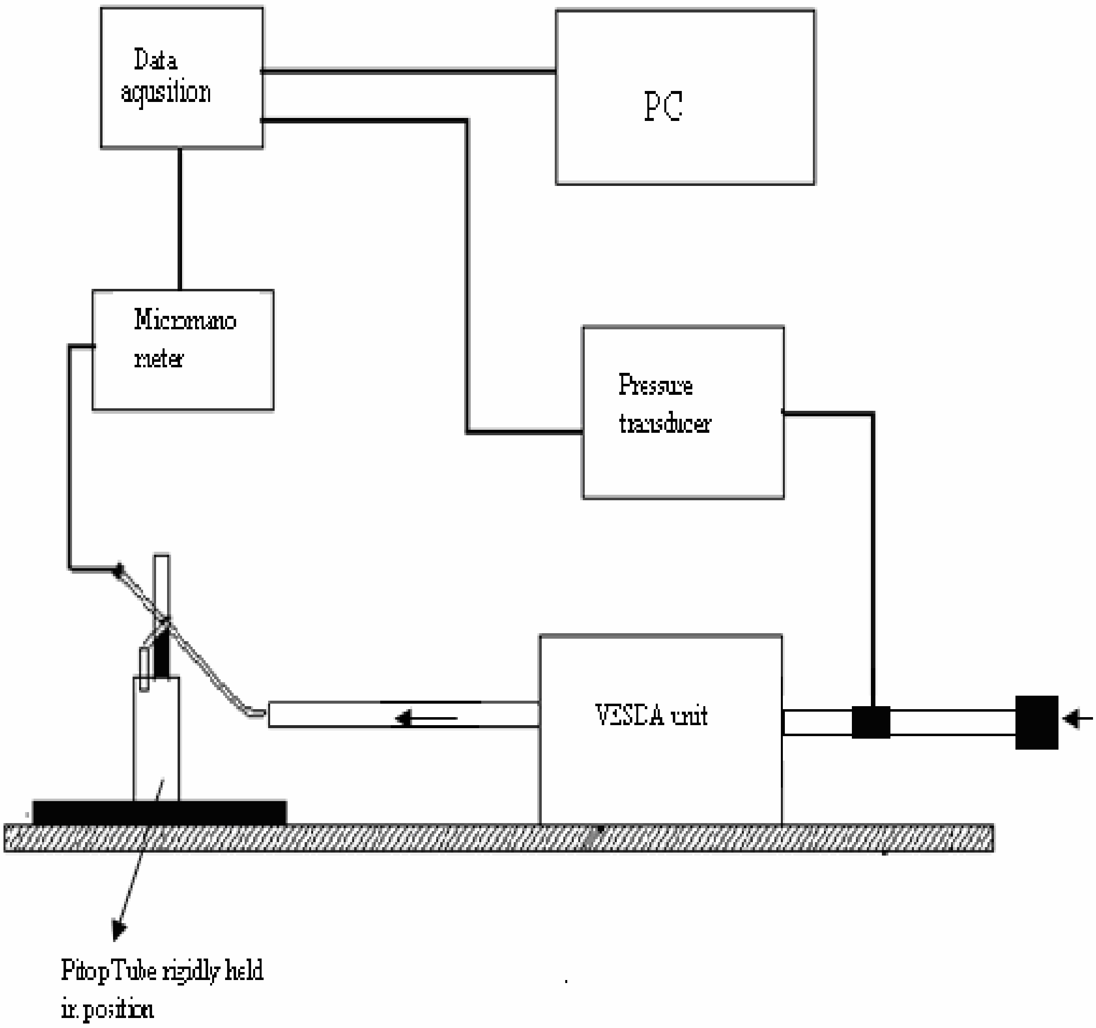

Figure 3.6 Experiment set to characterise the VLP Aspirator

Graphs of pressure drop versus flow rates were plotted. Using the curve fitting procedures, the equations of best fit were determined. It was found that polynomials of third order proved to be accurate enough for the current purpose.

3.3.2 Mathematical Equations for VLP Aspirator Performance

A single mathematical expression is required which will allow the calculation of pressure at the manifold given the aspirator speed, *S* (rpm) and the flow rate.

To generate the expression, firstly, equations were obtained by correlating the pressure versus flow rates at each aspirator speed, $P \to f(Q)$, using third order polynomials.

In order to generate an equation where $P \to f(Q,S)$ (pressure as a function of flow rate *Q* and aspirator speed, *S*), equations are generated by plotting the aspirator speeds versus the coefficients of the polynomials. Figure 3.7 shows the experimental data and the results calculated from the curve fitted polynomials. The figure shows that the curve fittings are reasonable, where the R^2 values were in the range of 0.9 to 0.98.

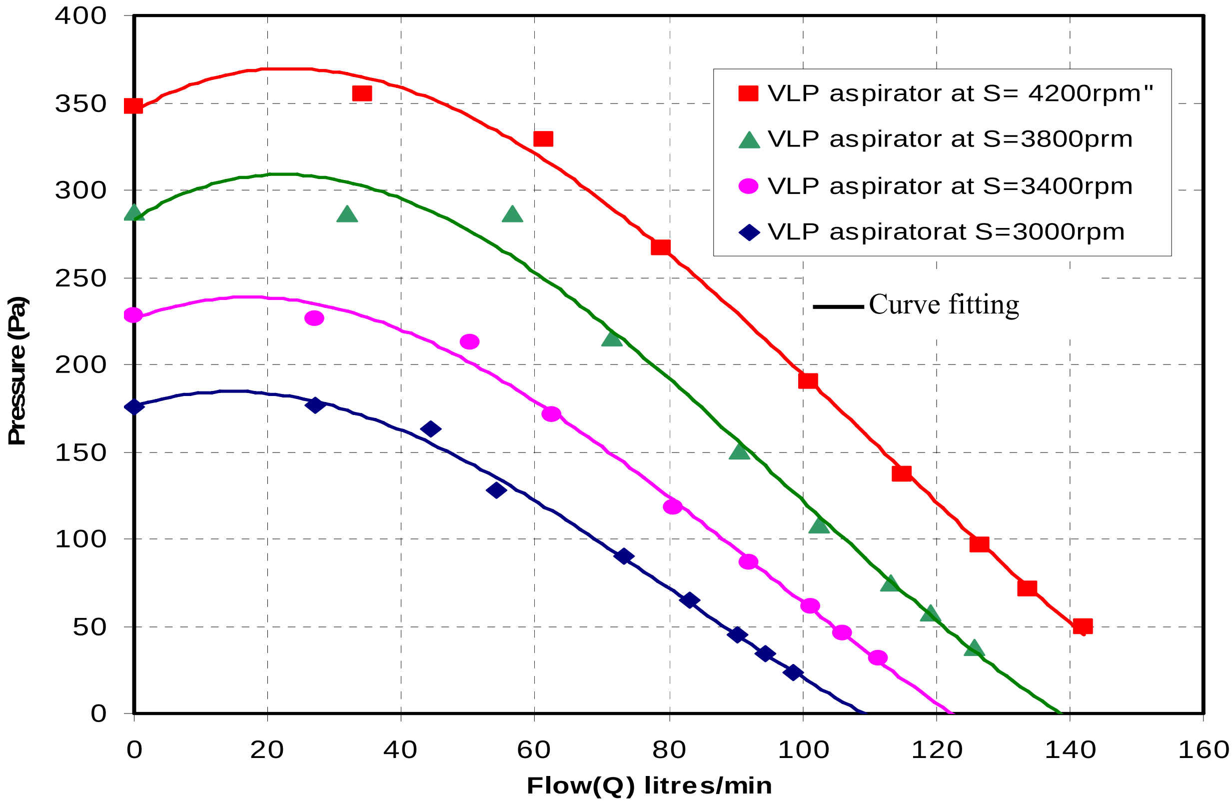

Figure 3.7 Pressure drop, P vs flow rate (Q) for various aspirator speeds, S, for VLP Aspirator

Table 3.2 shows the coefficients for the third order polynomials at different speeds,

$$P = AQ^3 + BQ^2 + CQ + D$$

Rpm (S)	Coefficient A	Coefficient B	Coefficient C	Coefficient D
3000	0.00016868	-0.043545	1.1154	175.33
3400	0.00017406	-0.048846	1.5228	226.09
3800	0.00017841	-0.053653	1.948	284.59
4200	0.00015955	-0.053044	2.2086	344.57

Table 3.2 coefficients of equations from figure 3.7

3.3.2.1 Equations of aspirator speed (S) versus Coefficients A, B, C, D,

Data from table 3.2 were used to generate equations. For simplicity linear equations were preferred, however, the R^2 values are to be 0.9 or better for the accuracy required to compute the manifold pressure. Where the linear equations were not applicable, polynomial equations were used in the form $y = aS + b$ or $y = aS^2 + cS + d$ for each coefficient A, B, C, and D respectively. The results are as following.

$$y_1 = -0.37912 \times 10^{-10} S^2 + .2672 \times 10^{-6} S + -0.29384 \times 10^{-3}$$
$$y_2 = 0.92408 \times 10^{-8} S^2 - .07486 \times 10^{-4} S + .098114$$
$$y_3 = 0.926 \times 10^{-3} S - 1.63562$$
$$y_4 = 0.16051 \times 10^{-4} S^2 + 0.02729 S - 50.266$$

$$P_{manifold} = y_1 + y_2 Q + y_3 Q^2 + y_4 Q^3 \qquad (3.14)$$

Here Q is the flow in litres /min., and y_1, y_2, y_3, and y_4 are the curve fitting of A, B, C and D respectively

3.3.3 Experimental set up to characterise the VLS aspirator

Figure 3.8 shows the VLS system which has a butter fly valve in each of its inlets. These valves will disturb the flow entering the aspirator system and thus the relationship between pressure and speed will be different from those for the VLP system and therefore it needs to be characterised separately.

Figure 3.9 shows the experimental setup to collect data of a VLS aspirator. Four separate pipes from each port are merged into a single pipe as shown in Figure 3.9, detail 1.

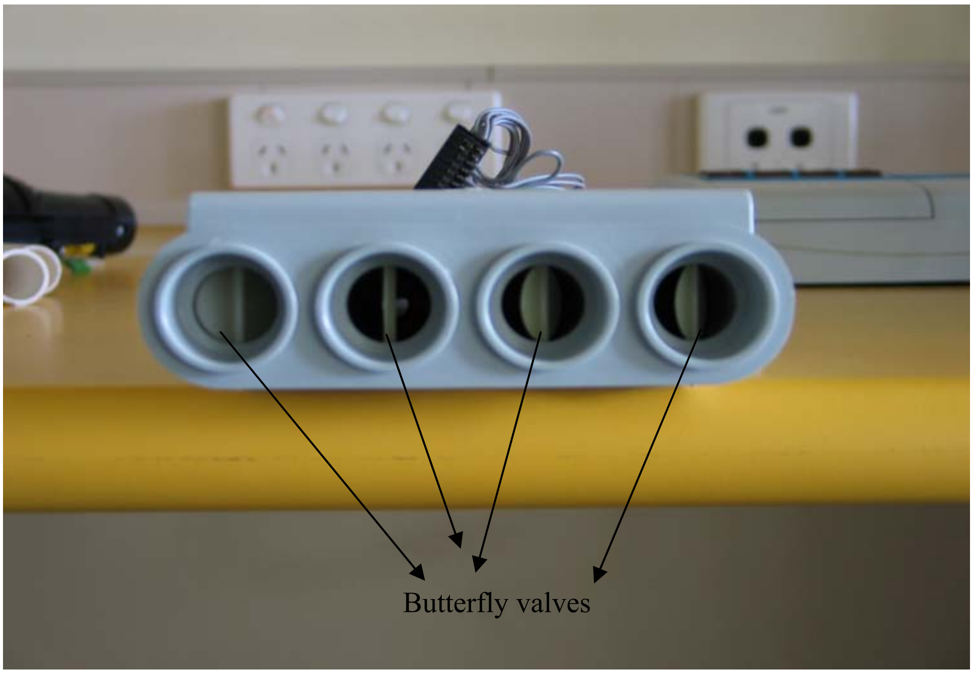

Figure 3.8 Showing the butter fly valves in a VLS

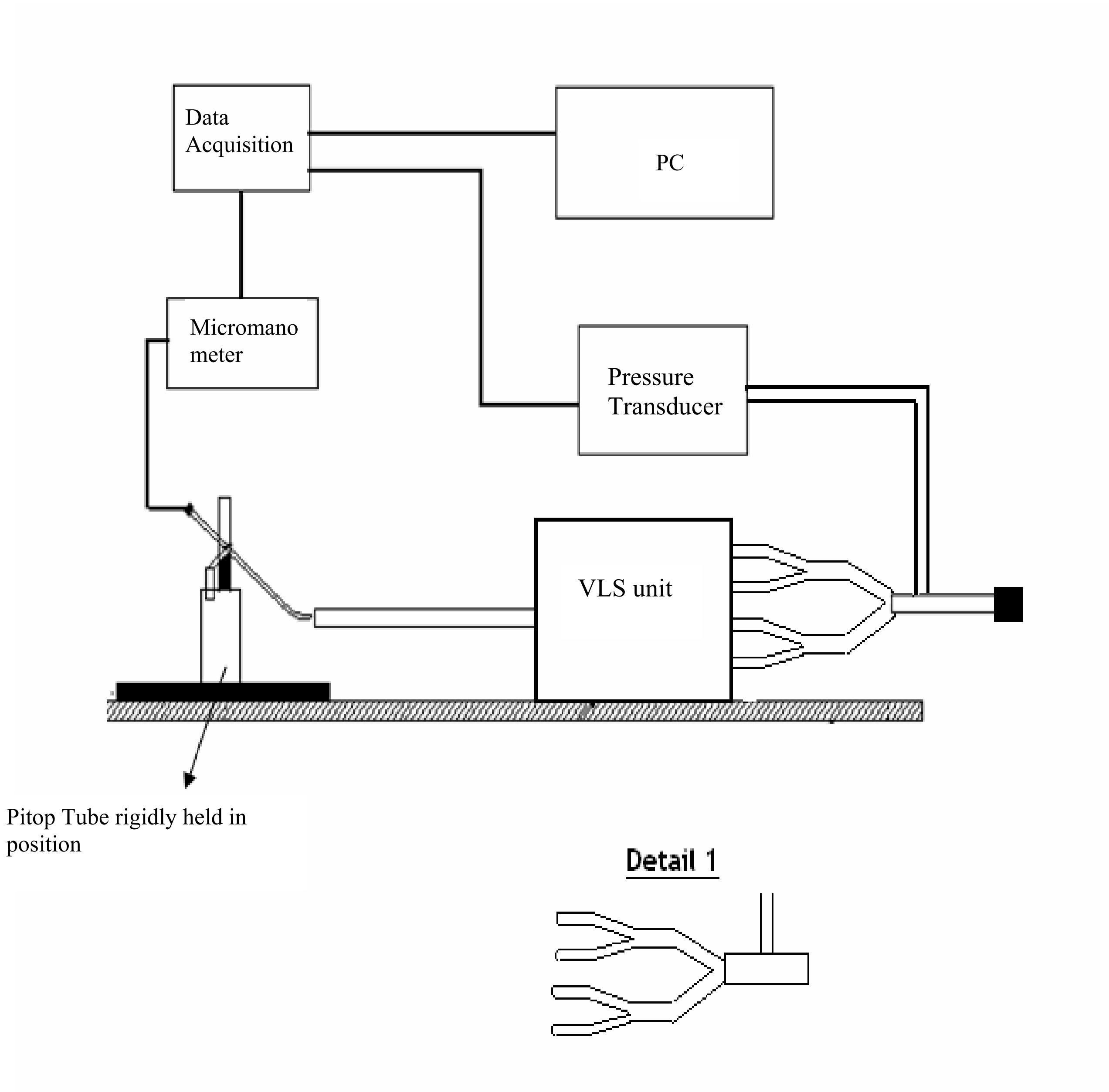

Figure 3.9 Experiment set up to characterise the VLS Aspirator. Detail 1 showing the pipe connection to manifold

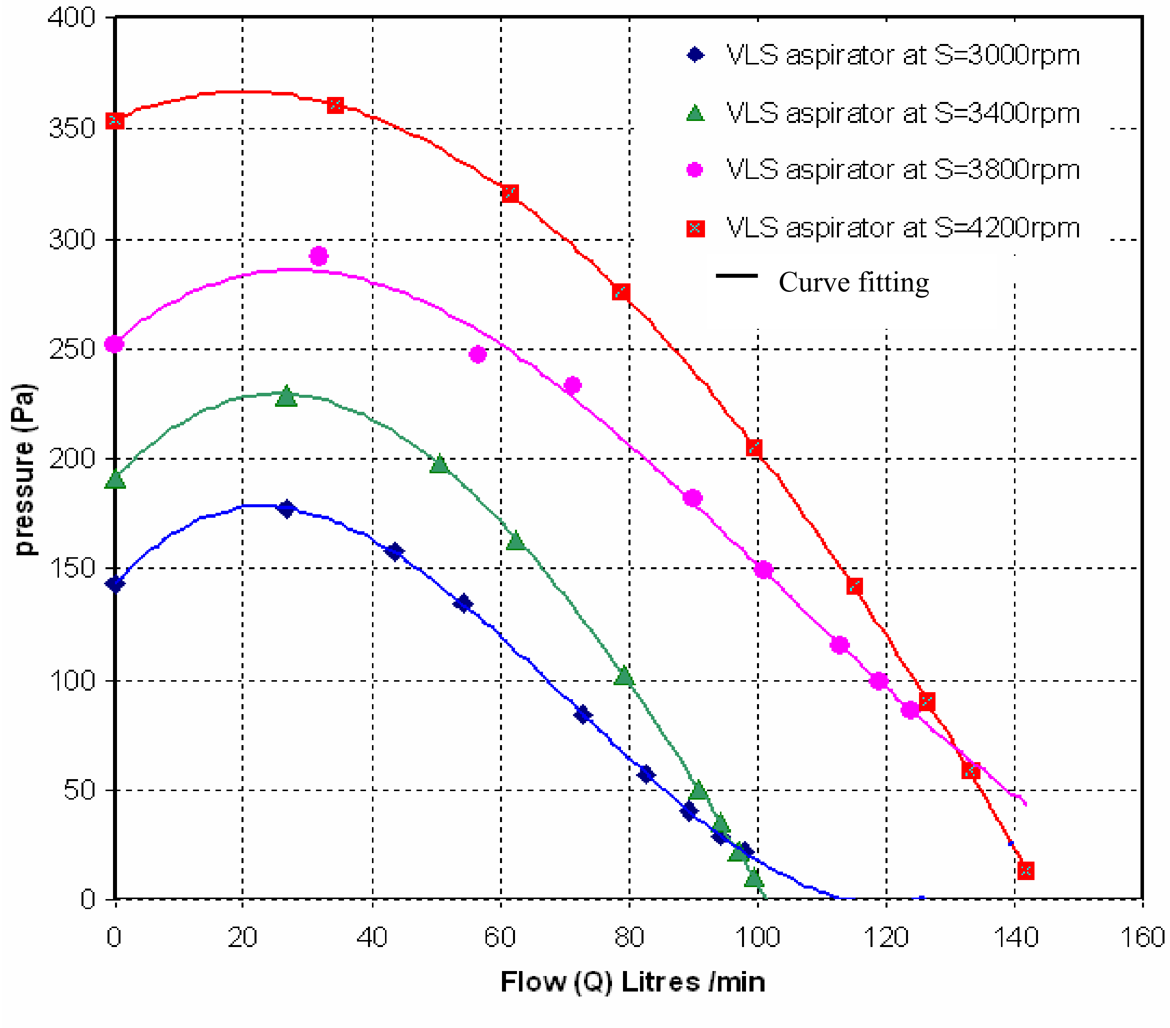

Figure 3.10 Pressure drop, P vs flow rate (Q) for various aspirator speeds, S, for VLS Aspirator unit

3.3.3.1 Equations of pressure versus flow, $P \rightarrow f(Q)$

The general form of the polynomial for a given speed is again assumed to be $P = AQ^3 + BQ^2 + CQ + D$ .The R^2 values for the correlation are in the range of 0.9 to 1. Fitting a third order polynomial using four data points will produce an exact curve fit therefore $R^2 = 1$.

Rpm (S)	Coefficient A	Coefficient B	Coefficient C	Coefficient D
3000	0.00040001	-0.0855026	3.29941	142.8003
3400	0.0002012	-0.0700925	3.156740	191.0959
3800	0.0001688	-0.0519819	2.5031336	252.519
4200	0.0000408	-0.0313247	1.2181955	354.061

Table 3.3 Curve fitting equations from figure 3.10

3.3.3.2 Equations of aspirator speeds(S) versus Coefficients A,B,C,D

Data from table 3.3 are used to generate second order polynomials in the form $y = aS^2 + bS + c$ for each coefficient A, B, C, and D respectively. The R^2 values were in the range of 0.9 to 0.98

$$y_1 = 1.1064 \times 10^{-10} S^2 - 1.0741 \times 10^{-6} S + 2.6135 \times 10^{-3}$$
$$y_2 = 8.1986 \times 10^{-9} S^2 - 1.3869 \times 10^{-5} S - 0.11769$$
$$y_3 = -1.7848 \times 10^{-6} S^2 + 1.1126 \times 10^{-12} S - 14.022$$
$$y_4 = 0.000083 S^2 - 0.425221 S + 671.03447$$

$$P = y_1 + y_2 Q + y_3 Q^2 + y_4 Q^3 \qquad (3.15)$$

Here Q is the flow in litres /min., and y_1, y_2, y_3, and y_4 are the curve fitting of A, B, C and D respectively

3.3.4 The manifold pressure equation of the VLC unit

The VLC unit runs at a constant speed of 2800 rpm, hence the equation takes the form $P \rightarrow f(Q)$

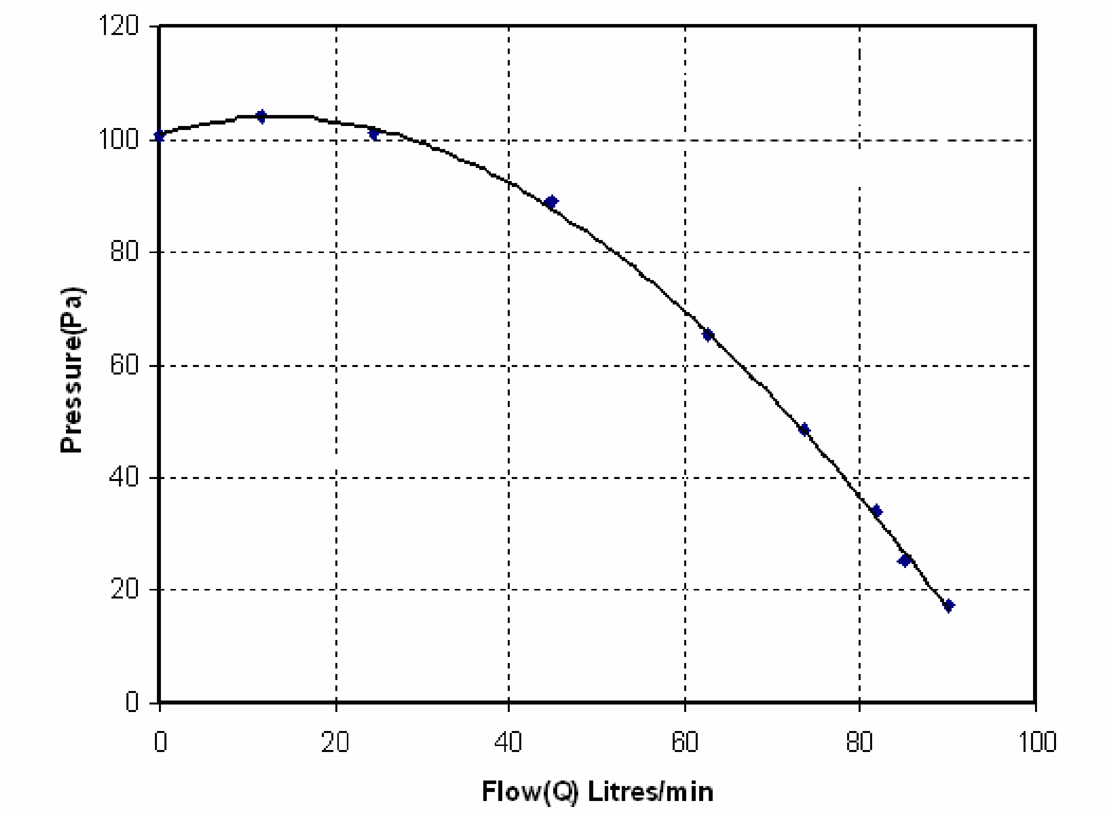

Figure 3.11 Vacuum pressure, P Vs flowrate, Q for VLC unit

$$P_{manifold} = 100.75 + 0.476 \times Q - 0.0184 \times Q^2 + 3 \times 10^{-5} \times Q^3 \qquad (3.16)$$

The R^2 value in this curve fitting is 0.99

CHAPTER 4

COMPUTATIONAL FLUID DYNAMICS SIMULATION AND DATA ANALYSIS

The objective of this chapter is to obtain some understanding on the friction factor and the local loss caused in a pipe where the flow is interrupted by jet inductions. Good approximations for these losses are needed to model the pressure losses associated with each of the expected variations in a typical pipe network that is used for VESDA® aspirated smoke detection systems.

In modeling the pipe networks used with VESDA® systems, previous pipe network models use equations for friction such as $f = 64/Re$ for laminar flow (Equation 2.6) or $f = 0.316/\mathrm{Re}^{0.25}$ for turbulent flow (Equation 2.7). None of these equations give values for friction that are accurate enough to model the pressure loss and transport time to the desired 90% accuracy requirement.

This chapter describes the methods and the results of simulations carried out using Computational Fluid Dynamics (CFD) software (CFX – 5.5.6) to gain an understanding of the effect the disturbance ratio (Q_{in}/Q) has on friction factors so that an equation for the friction factor, which is a function of the disturbance ratio, can be determined.

Computational Fluid Dynamics is computer based software used for simulating the behaviour of the systems involving fluid flow, heat transfer and other related physical processes. It works by solving the equations of fluid flow over a region of interest, with specified conditions on the boundary of that region.

Recent advantages in computing power, together with powerful graphics and interactive 3-D manipulation of the models mean that the process of creating a CFD model and analysing the results is much less labour intensive, reducing time and cost.

Consequently CFD provides a cost effective and accurate alternative to scale model testing, with variations on simulation being performed quickly. CFD is exclusively used in research and as a design tool in industries.

4.1 Creating a VESDA Pipe Model for Simulation

A typical VESDA pipe with a capillary tube model was created as shown in figure 4.1. The length of the main pipe was 1 meter and the capillary tube was attached 100mm from the intake end. The reason for the 1m pipe was to give enough length to ensure that the flow was reasonably developed after being disturbed by the jet induction from the capillary tube.

The volume flow rate of the jet induction was regulated by changing the length of the capillary tube. (The flow rate can also be changed by varying the inlet velocity). This was necessary to determine the impact on losses due to the ratio of Q_{in}/Q. Here Q_{in} is the flow rate in the capillary tube and Q is that in the main pipe. The magnitude of disturbance, Q_{in}, coming in contact with Q is represented by the ratio Q_{in}/Q. The longer the capillary tube, the lower the volume flow rate from the capillary tube, hence the lower the magnitude of disturbance.

Simulations were carried out for capillary tube lengths from 125mm to 1000mm.

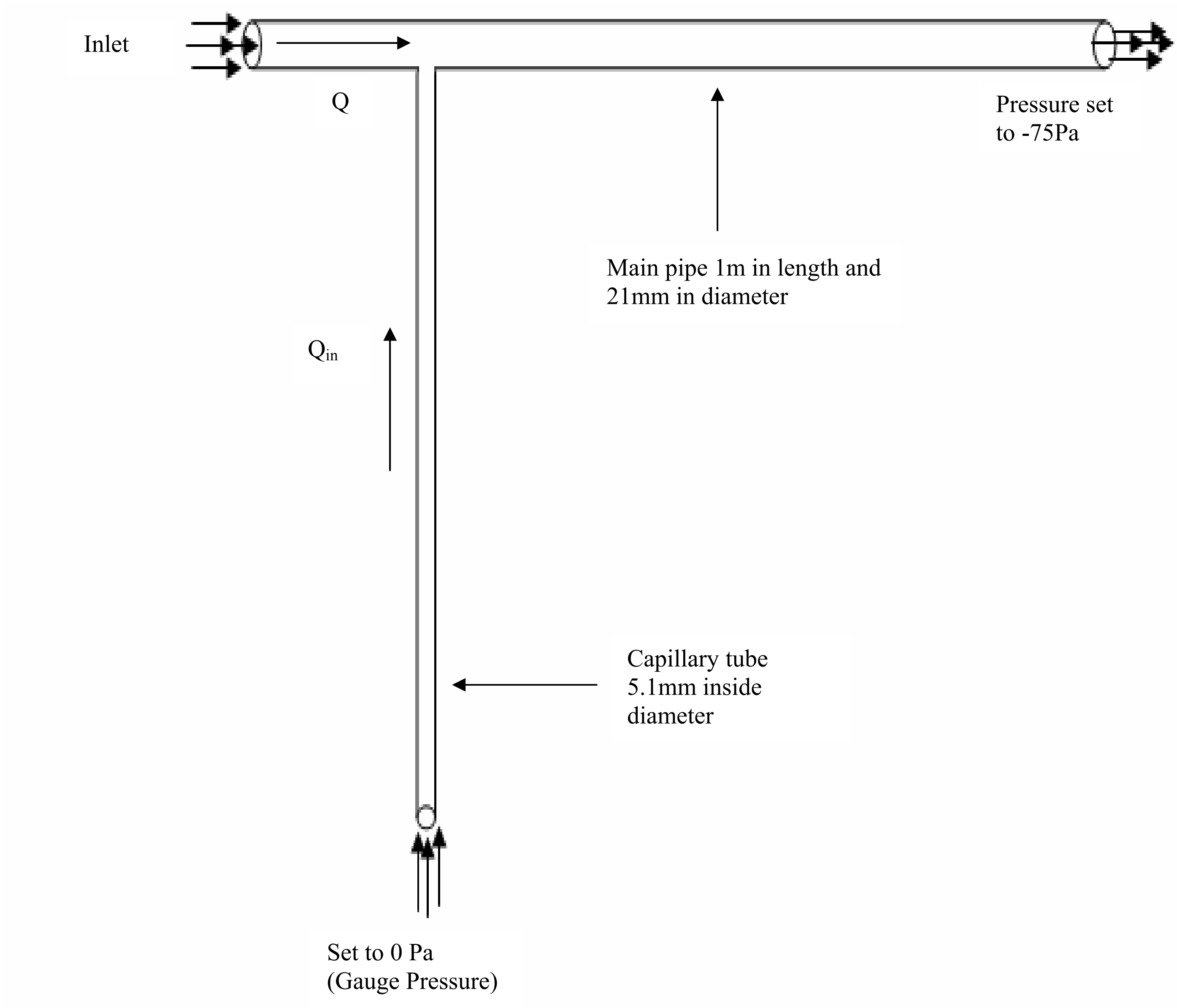

Figure 4.1 Geometry of a model and boundary conditions

4.2 Boundary Conditions

Figure 4.1 illustrates the boundary conditions for the pressures and the flows. The boundary condition for the inlet of the main pipe was set as parabolic, illustrated by equation (4.1). The inlet flow is a continuation of an existing pipe. If a uniform velocity inlet is used, a long developing length is required to have the flow fully developed.

$$Inlet\ Velocity \quad = V_{\max} \times \left(1 - r_a^{\,2}\right) \tag{4.1}$$

$$r_a = \sqrt{\left(r_x^{\,2} + r_y^2\right)}$$

$$r_x = \frac{2x}{D_{pipe}}$$

$$r_y = \frac{2y}{D_{pipe}}$$

$$V_{\max} = 3.0\, m/s$$

$$D_{pipe} = 21mm$$

The suction pressure of the outlet was set to –75 Pa and the reference pressure at the capillary tube intake was set to 0 Pa (gauge pressure). Due to the expected low volume flow rates in VESDA systems, this value of V_{max} was chosen which is close to the velocity encountered in the field. The flow regime was set to subsonic and this flow was considered as isothermal.

4.3 The Solution Method Used by CFX – 5.5.6 CFD Software

There are a number of different solution methods used in CFD software. The most common, and the one on which CFX – 5.5.6 is based is known as the finite volume technique.

In this technique, the region of interest is divided into small sub regions, called control volumes. The equations were discretised and solved iteratively. As a result, an approximation of the value of each variable at a specific point throughout the domain can be obtained. In this way, one derives a full picture of the behaviour of the flow.

4.4 The Turbulence Model Applied

The commonly used κ-ε turbulent model was applied in the simulation. This model is based on the concept that turbulence consists of small eddies which are continuously forming and dissipating. This model is numerically more robust than the Reynolds stress turbulent model in terms of convergence and stability. Even though the Reynolds numbers in the simulations are low, however, it was thought that the flows are generally turbulent due to regular disturbances.

4.5 Convergence Criteria

The CFD software package offers various surface and volume mesh types. For this study the hex/wedge fine mesh option was used in order to obtain simulated results of high accuracy. The maximum grid length was set to 0.001m. The maximum number of iterations was set to 150 and the target relative residual was set to 0.001. The blend factor was specified to 2nd order. These settings were determined based on many trial simulations. Past experience showed that for pipe diameter of 21mm a grid size of 1mm yielded sensible results.

4.6 Simulating the Flows

The simulation process took approximately 120 iterations to converge. A total of five flows were created, keeping all the boundary conditions constant, except the capillary tube length, which was changed from 125mm for the first model to 1000mm for the last model.

4.7 CFD Simulation Results

In this section the simulated results are presented. These include the flow rates through the capillary tube, the flow rates at the inlet and outlet of the main pipe and graphical representations of pressure gradients, wall shear stress, and velocity vectors.

Tecplot was used to plot the velocity vectors to visualise directions and magnitudes. An Excel spreadsheet was used to graphically illustrate the pressures drop and wall shear stress as affected by the disturbance from the jet.

4.7.1 Extracting the Results from CFD Simulations

The following data were extracted for each CFD simulation.

- Mass flow rate in the capillary tube
- Mass flow rate in the inlet
- Pressure drop along the main pipe
- Pressure drop near the capillary tube, in the main pipe, due to the disturbance
- Wall shear stress
- Velocity vectors of the flow in the main pipe

The results for the pressure gradient and velocities were determined at a set of user defined points within a coordinate system. The polyline function in the CFD program was used as a locator for the user defined points. Figure 4.2 shows the YZ plane coordinate system that was used.

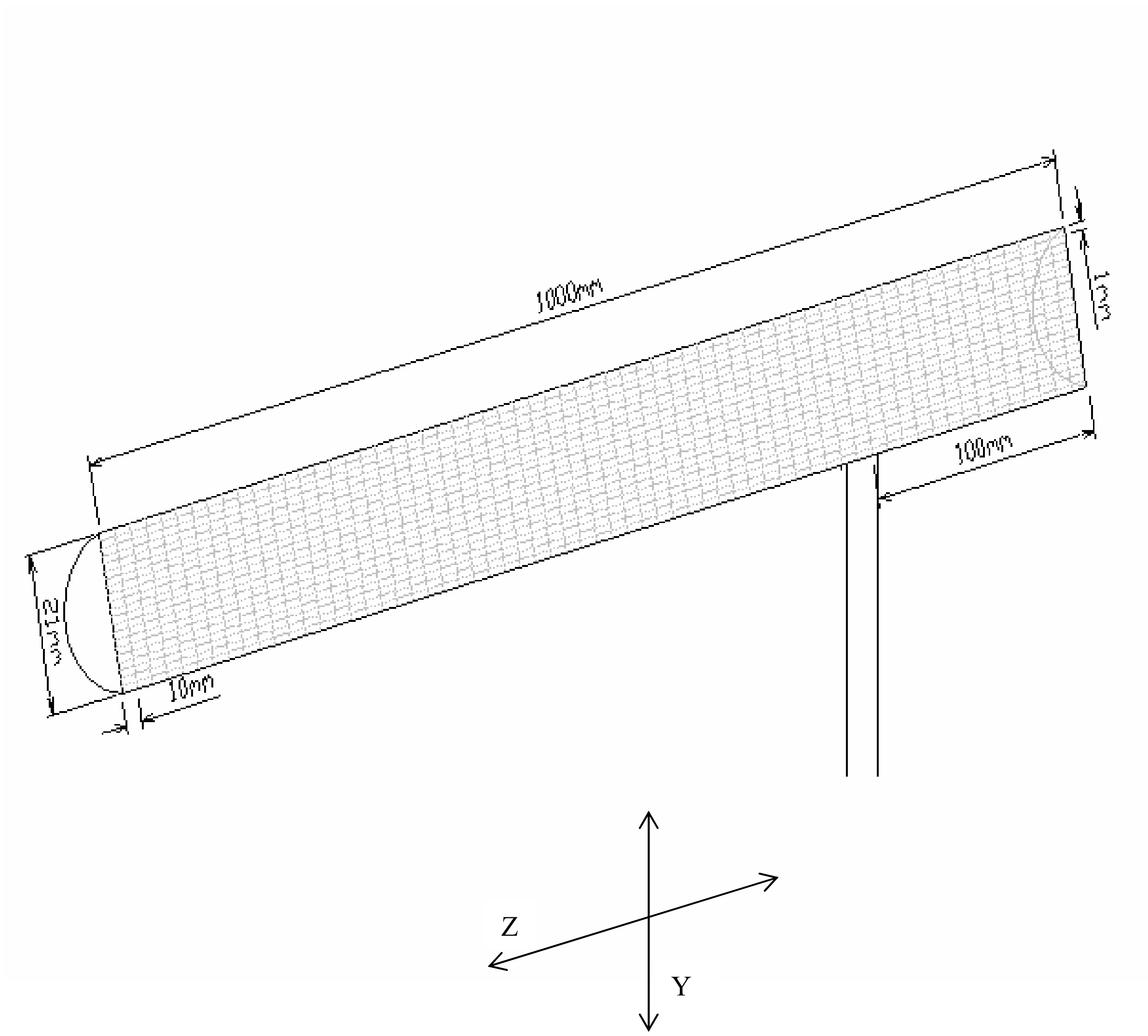

Figure 4.2 The coordinates in YZ plane

4.8 Simulation Results

4.8.1 Mass Flow Rates of the Simulations

Table 4.1 shows the mass flow rates in the capillary tube and the disturbance ratio (Q_{in}/Q). This information is included here as reference. The values in this table are used to determine the effects on friction when jet induction is present.

	Mass Flow			
Simulation No.	**Capillary tube length (mm)**	**Capillary Tube kg/hr**	**Inlet kg/hr**	**Disturbance Ratio (Qin/Q)**
1	125	0.89	2.44	0.366
2	250	0.58	2.44	0.238
3	375	0.53	2.44	0.220
4	500	0.44	2.44	0.184
5	1000	0.31	2.44	0.128

Table 4.1 Results of the Simulation of Mass Flow Rates

4.8.2 Pressure Drop along the Main Pipe

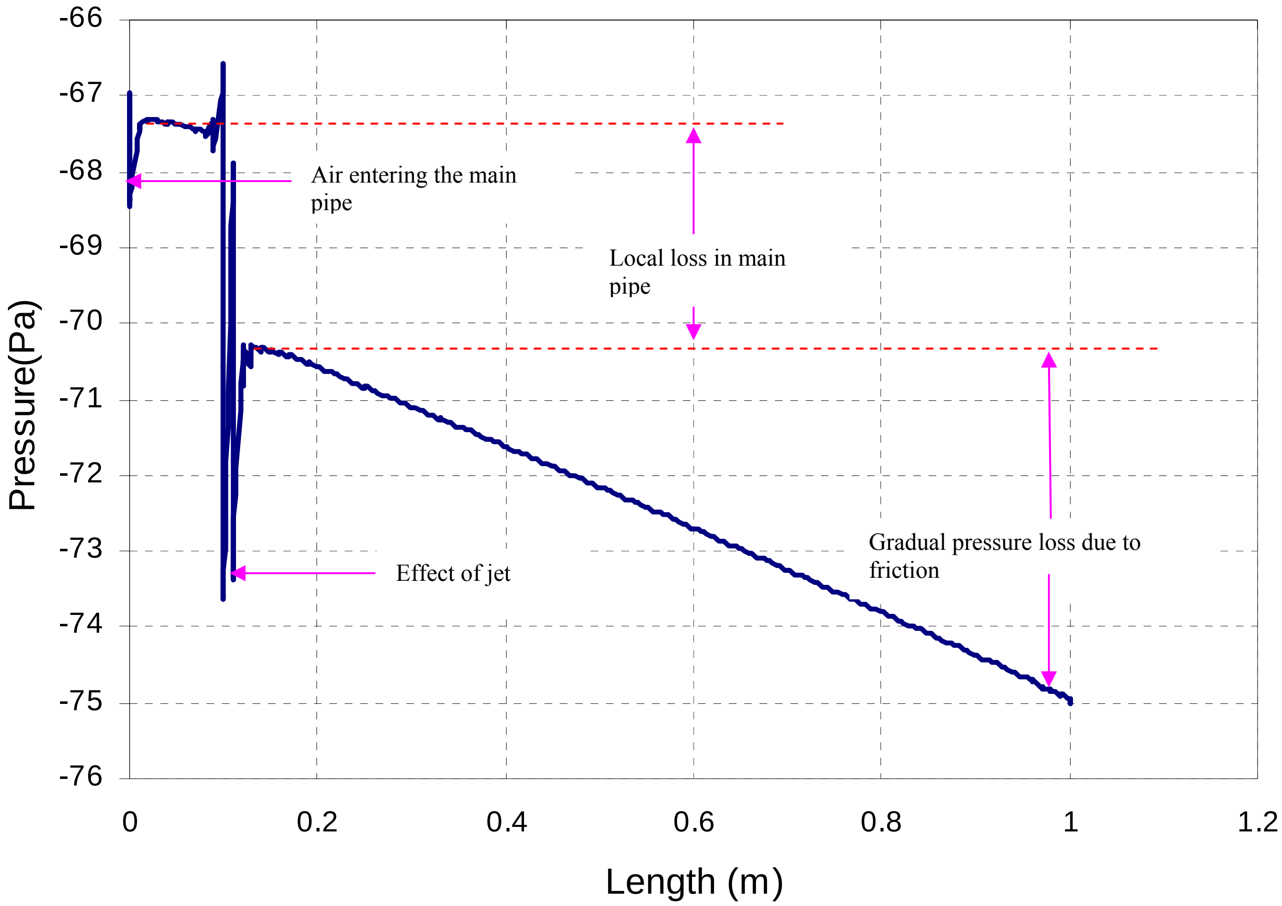

Figure 4.3 Pressure drop along the main pipe with side pipe 125mm long and flow ratio Q_{in}/Q of 0.366

Figure 4.3 shows the pressure drop along the pipe, with a capillary tube length of 125mm. After flow enters the main pipe, at 100mm from the entry, the main flow is disturbed by the incoming jet from the capillary tube.

The disturbance from the jet induction causes pressure fluctuations as the flow passes the capillary tube hole. The disturbance is present over the 5.1mm diameter of the capillary tube.

At the end of the disturbance, the normally expected gradual pressure drops due to friction. The local loss in this situation has been defined by the difference in the pressure at the beginning of the capillary tube and the pressure at the beginning of the resumption of the gradual decrease in pressure after the capillary tube.

Five cases were simulated with varying capillary tube lengths. Each capillary tube length caused a different flow rate thereby changing the level of disturbance. For each simulation, the interests were the local loss and the pressure loss gradient for the main pipe flow after the capillary tube. In section 4.9 these data are compared to standard formulae for determining local loss and pressure gradient and a mathematical model for friction is developed. (The simulated results can be seen in the appendices, figures E1 to E5).

4.8.3 Flow Velocity Vectors near the Jet Injections.

To calculate the transport time it was necessary to understand the effect of the jet on the main flow.

Figure 4.4, produced from CFD simulation models, and charted using Tecplot, shows the velocity vectors of the main flow as it passes the jet from a capillary tube. The main flow is forced towards the pipe wall, which causes the shear stress at this point to increase. This can be seen in figure 4.5, which is plotted from CFD simulation.

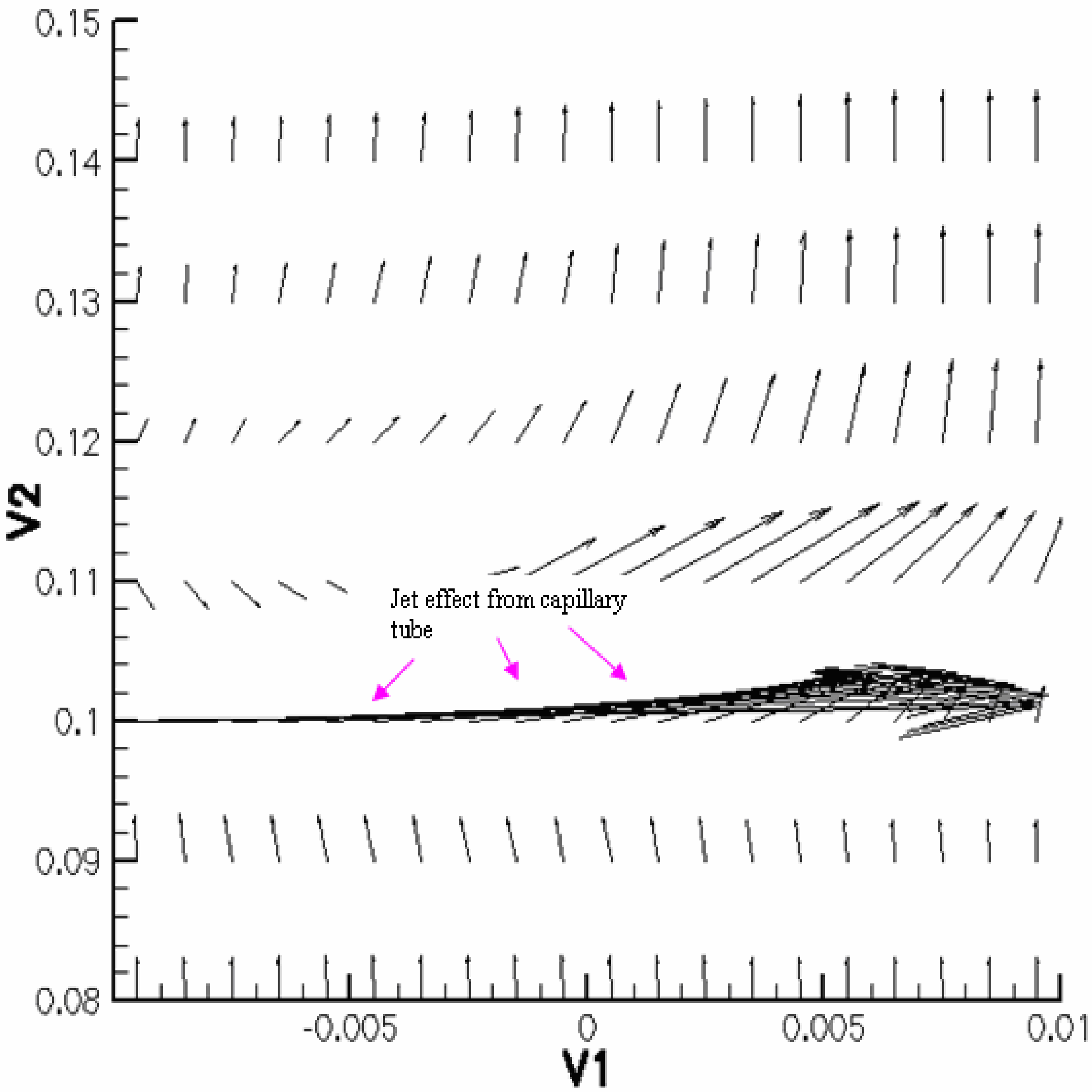

Figure 4.4 Showing velocity vector along the main flow. The velocity V2 in the Z direction and V1 in Y direction

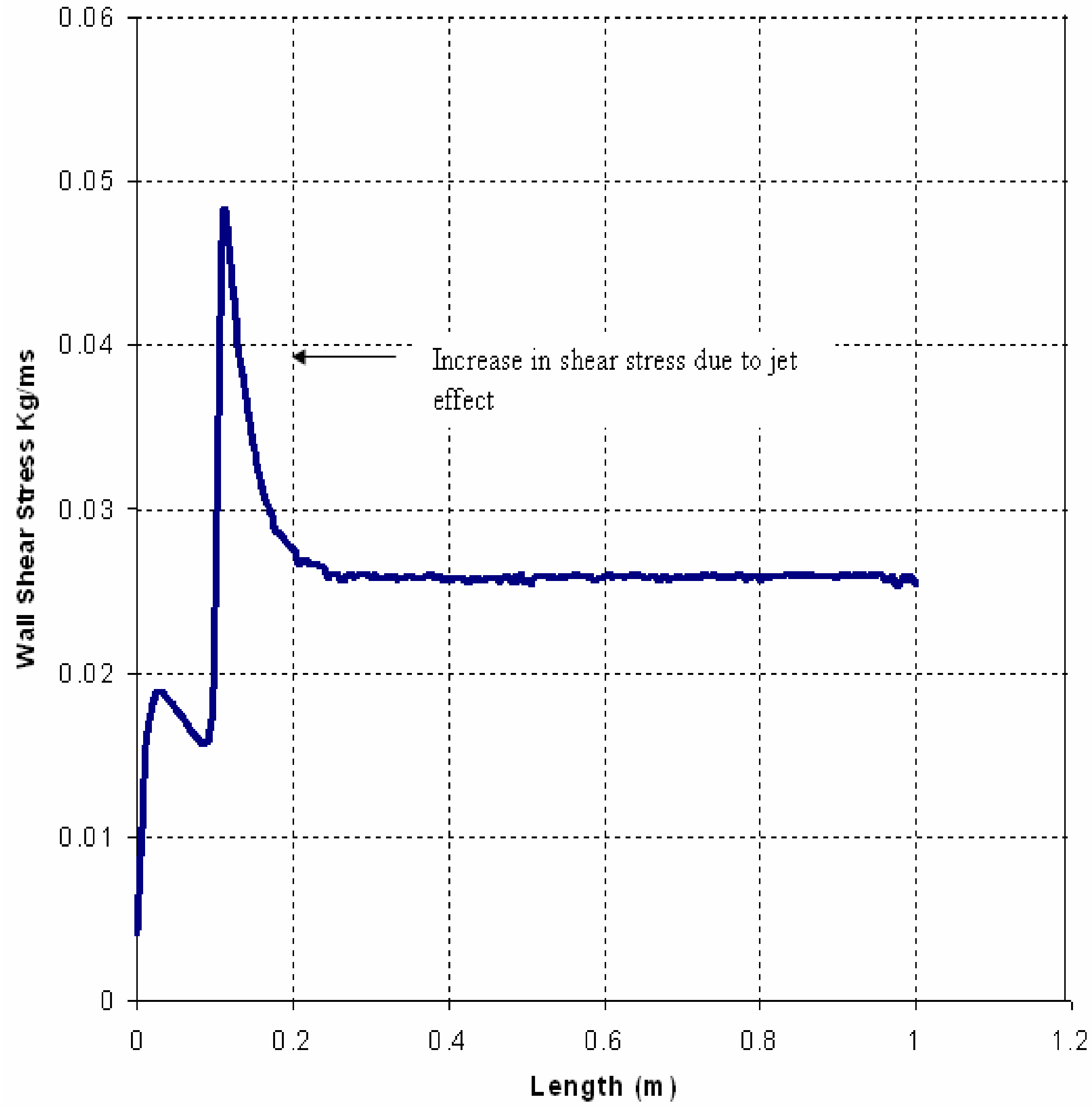

Figure 4.5, Showing the jet effect on the wall shear stress on the flow in the main pipe

At the point where the shear stress is very large, the main flow is damped, losing kinetic energy to overcome the shear forces, thus causing increased impedance to the main flow.

4.9 Analysis

In this section, the simulated data are analysed. From figure 4.3 the local loss and the frictional loss in the main pipe are compared with the results obtained by standard mathematical models as described in chapter 2.

4.9.1 Local Loss Coefficient (K)

The local loss coefficient in the main pipe close to a capillary tube is calculated using two methods. The first method uses equations from a standard text book, such as Potter and Wiggert, (2002). The second method uses simulated data from figure 4.3 and works backwards to determine a value for the local loss coefficient. The results are then compared.

Air entering the sampling hole into the main pipe is considered as sudden enlargement geometry. From Potter and Wiggert,(2002), for sudden enlargement

$$K = \left(1 - \frac{A_1}{A_2}\right)^2 \tag{4.2}$$

Here K is the local loss coefficient, A_1 is area of the capillary tube and A_2 is the effective area of the enlargement.

In the case being considered A_2 is the main pipe surface area, which is very large in comparison to A_1. Thus $K \approx 1$. Using simulated data from figure 4.3, K_{sim} is calculated using the equation

$$K_{sim} = \left[\frac{\Delta P_L \times 2}{\rho \times V^2}\right] \tag{4.3}$$

Here ΔP_L is the pressure loss in the main pipe close to the capillary tube and V is the mean velocity in the capillary tube.

Table 4.2 shows the K_{sim} values determined from the simulations and gives an average value of 0.80

Simulation	K_{sim} **value**
1	1.01
2	0.70
3	0.72
4	0.70
5	0.69
Average	0.80

Table 4.2 Values of K calculated from

4.9.2 Calculation of Friction Factor *f*

The friction factor is calculated and compared with the results from the CFD simulation.

The first calculation uses equation (2.6), for laminar flow, knowing that the flow in VESDA pipe networks is frequently at a Reynolds number value of 2000 or lower. The widely accepted equation for *f* for Reynolds numbers of 2000 or less is;

$$f = \frac{64}{\mathrm{Re}}$$

The second calculation uses equation (2.7), for turbulent flow. This equation is used knowing that even at low Reynolds numbers in the VESDA pipe networks, the flow can be of a turbulent nature due to frequent jet disturbances of the main flow. The widely accepted equation for turbulent flow for Reynolds numbers between 4 x 10^3 and 1 x 10^5 is;

$$f = \frac{0.316}{\mathrm{Re}^{0.25}}$$

The calculated values are compared with the friction factor determined from the CFD simulations for pressure drop versus pipe length as in figure 4.3. The other simulated graphs are attached in Appendix C. The actual friction factor is calculated using. equation (4.4), which is a transposition of equation (2.5) by solving for *f*.

$$f = \frac{2D}{V^2 \rho} \times \frac{\Delta P}{\Delta L} \tag{4.4}$$

In equation (4.4), $\frac{\Delta P}{\Delta L}$ is the slope of the graphs in the region where the pressure drop occurs linearly due to friction as indicated in figure 4.3, ΔP is the pressure drop due to friction, ΔL is the length of main pipe segment where the pressure loss occurs due to friction and V is the mean velocity of air in the main pipe labelled as “outlet” as calculated from the mass flow values in Table 4.1

The results are presented graphically in figure 4.6.

4.9.3 Results for Friction Values

Pressure drop (Pa)	Volume Flow rate from outlet (M^3/S)	Re	Q_{in}/Q	Friction$_{Sim}$	Friction$_{Lam}$	Friction$_{Tur}$
4.9	7.717×10^{-4}	3119	0.366	0.03838	0.02051	0.04228
3.7	6.994×10^{-4}	2827	0.238	0.03528	0.02263	0.04333
3.6	6.889×10^{-4}	2784	0.219	0.03538	0.02298	0.04350
3.5	6.689×10^{-4}	2703	0.184	0.03648	0.02366	0.04382
3.2	6.450×10^{-4}	2607	0.128	0.03587	0.02454	0.04422

Table 4.3 Results of friction factor *f* obtained from published equations and compared to friction factor obtained from simulation at different disturbance levels

From figure 4.6 it can be seen that equation (2.6) always predicts lower values for friction factor and equation (2.7) always predicts higher values, when compared to the actual friction loss determined from CFD simulations. This is expected since the Reynolds numbers shown in table 4.3 are in the transition region. From the simulated data it can also be seen that the friction factor increases as the Reynolds number increases. This is due to the effect of the disturbance ratio (Q_{in}/Q), which increases as the Reynolds number increases in this system and consequently causes higher losses. This phenomenon becomes more apparent in the later chapters.

This clearly indicates that equations (2.6) and (2.7), do not capture the jet effects of the friction factor because the flows are neither laminar nor fully turbulent. Therefore, these equations are not applicable to calculate friction factors in scenarios where a disturbance to the main flow occurs by jet induction, such as in VESDA pipe network systems. In field measurements, flows in the pipe work for aspirator smoke detection system are in or close to the transition region.

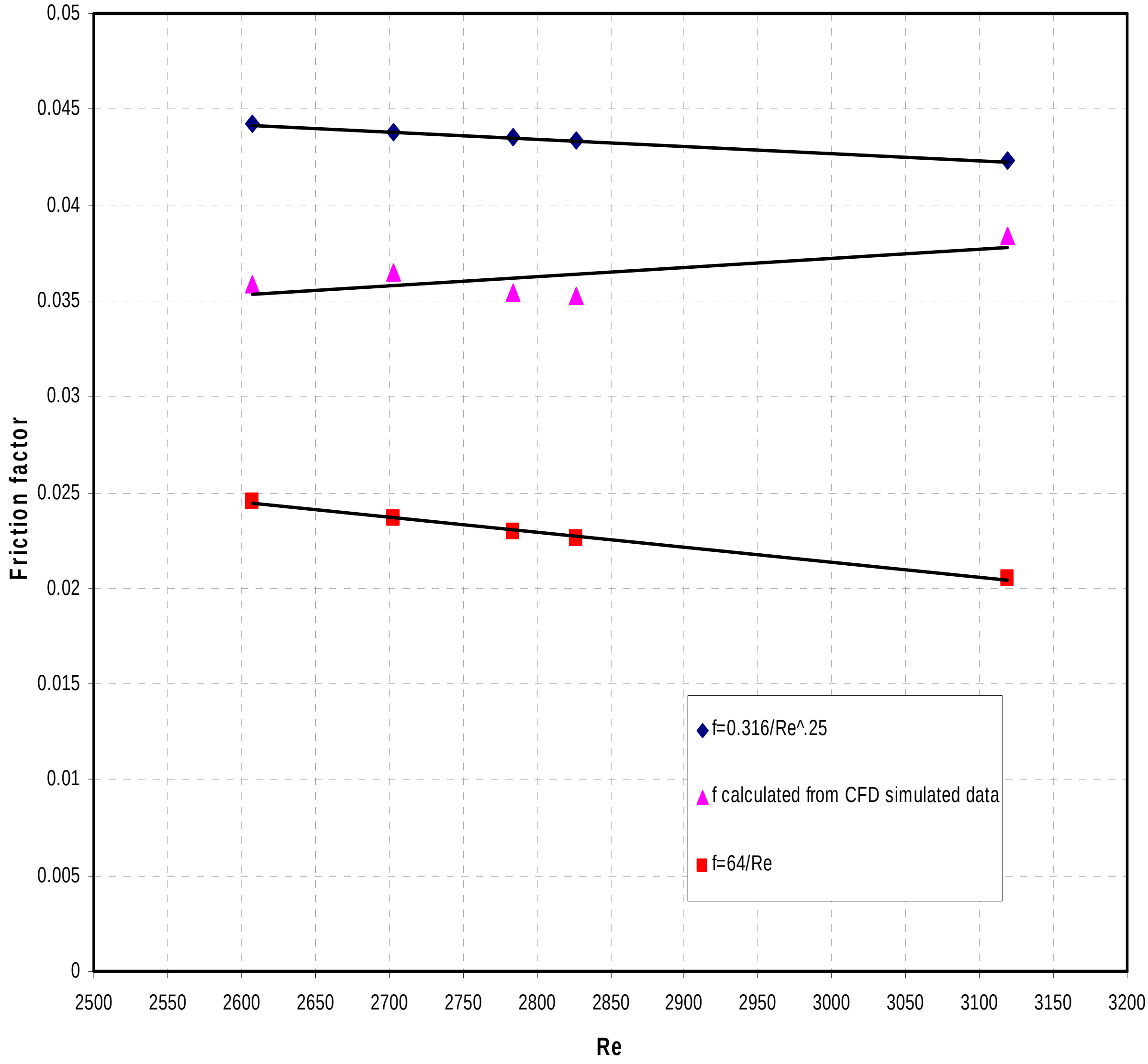

Figure 4.6 Graph of friction vs Re where the values for friction factor (*f*) calculated using the equations for laminar flow, *f= 64/Re*, turbulent flow *f= 0.316/Re*$^{0.25}$ and from simulated data

4.10 Discussion

Based on analyses of the simulated results, it can be concluded that the equations commonly used are not accurate enough in calculating the friction factor and the local loss coefficients to model pipe networks similar to VESDA systems, especially in order to achieve the desired accuracy.

To determine a model for the friction factor, further analysis of the simulated data is necessary to find a pattern that contributes to the friction loss, which is a function of the disturbance ratio (Q_{in}/Q). Once this is achieved, a new mathematical model can be developed to predict, the frictional loss in jet disturbance scenarios.

CHAPTER 5

MATHEMATICAL MODEL DEVELOPMENT AND VALIDATION

In this chapter mathematical models for friction factor and transport time are developed and the results are validated by measuring the pressure drop at sampling holes and transport times on representative systems.

This chapter also describes the procedures and methods used to calculate and measure the pressure drop near a sampling hole and the transport time from a sampling hole.

5.1 Equation for Friction Loss

From figure 4.6, it is understood that the published equations used to calculate the friction factor for laminar flow and turbulent flow are not accurate enough to calculate the pressure losses where disturbances to the main stream occurs by jet induction and the flows cannot be considered as fully laminar or fully turbulent such as the flow in the VESDA aspirated smoke detection system.

It was therefore decided to closely analyse the friction factor of the simulated system and the contributing factors to these friction factors such as the disturbance ratio (Q_{in}/Q) and flow rates in order to develop a generic mathematical model. The proposed mathematical model of the friction factor will therefore be a function of the disturbance ratio (Q_{in}/Q) which can be applied to pressure loss equations such as Darcy's equation in order to calculate pressure losses in pipes where a disturbance to flow exists.

When a disturbance due to jet induction is not present, the standard formula for friction for low Reynolds numbers (<2000), $f = 64/Re$ is an adequate approximation.

A correction factor, C_f, to this formula is needed for the condition when a disturbance is present. In this section an adequate correction factor will be determined. As a starting point the formula for approximating the friction is assumed as
$f_{sim} = 64/(Re * C_f)$.

From the simulation results in table 4.3, given the values of friction, pressure drop and flow rate, the correction factor (C_f) can be calculated by;

$$C_f = \frac{f_{lam}}{f_{sim}} \tag{5.1}$$

Here f_{sim} is the friction factor from the simulated results and f_{lam} is the friction factor calculated using laminar flow equation (*64/Re*).

Re obtained using equation **Re=** $\frac{\rho VD}{\mu}$	f_{sim}	f_{lam}	$C_f = \frac{f_{lam}}{f_{sim}}$	**Qin/Q**
3119	0.03838	0.02051	0.53451	0.366
2827	0.03528	0.02263	0.64159	0.238
2784	0.03538	0.02298	0.64947	0.219
2703	0.03648	0.02366	0.64868	0.184
2607	0.03587	0.02454	0.68417	0.128

Table 5.1 Results of Reynolds Numbers Ratio

Since the correction factor is also a function of the disturbance ratio (Q_{in}/Q), a relationship between the two can be made by plotting these values as shown in figure 5.1

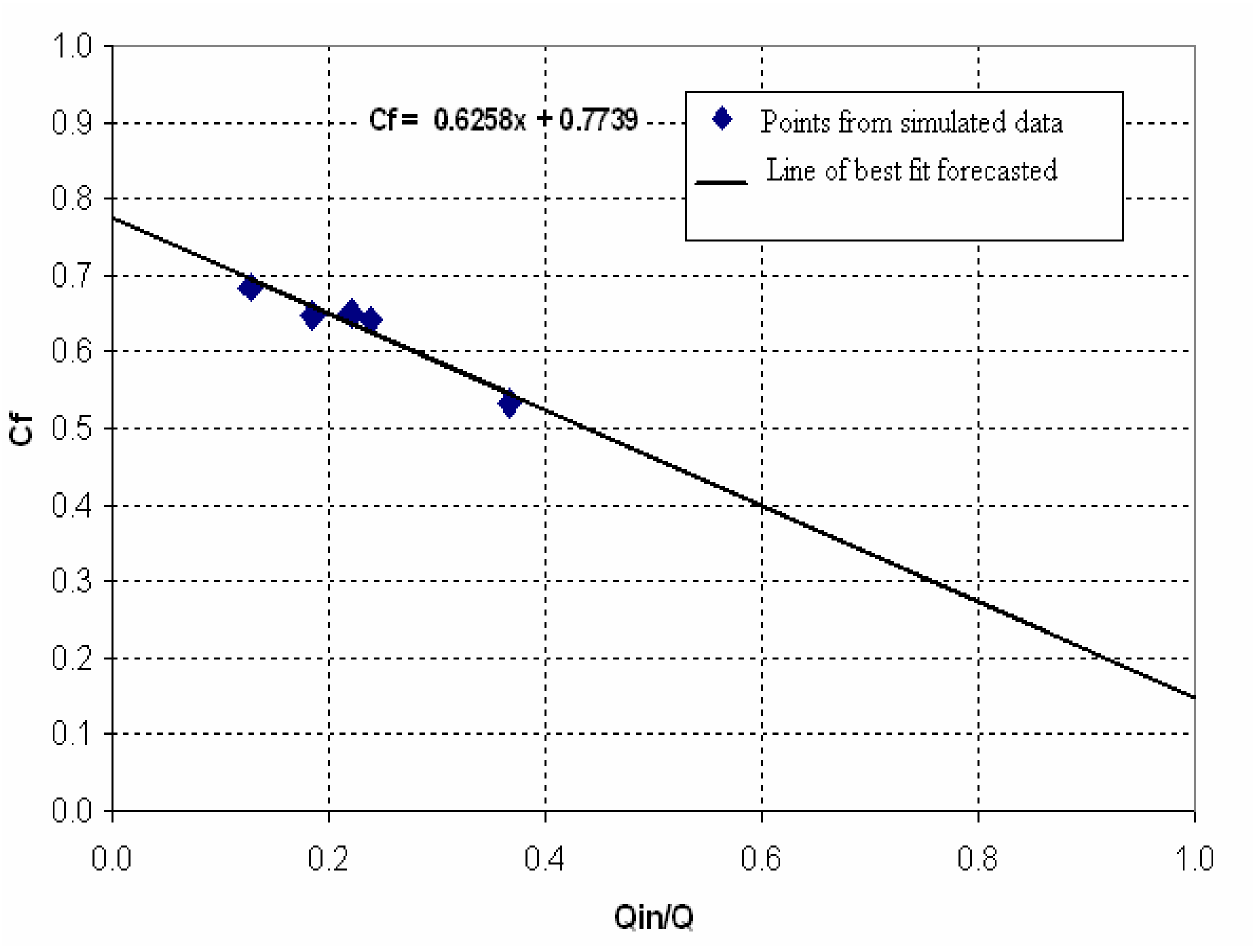

Figure 5.1 Graph of correction factor C_f vs disturbance ratio, (Q_{in}/Q)

From figure 5.1, the equation of the correction factor as a function of disturbance ratio is;

$$C_f = -0.6258 \times \left(\frac{Q_{in}}{Q} \right) + 0.7739 \tag{5.2}$$

The equation for friction factor can be written as;

$$f = \frac{64}{\mathrm{Re} \times C_f} \tag{5.3}$$

Here C_f is the correction factor and f is the friction factor.

Equation (5.3) gives an error of 4% (on average) when used to calculate the suction pressures of the sampling holes. It also gives an incorrect result at Qin/Q =0. When there is no disturbance, C_f should be 1. The reason could be that the Reynolds numbers of the simulated flows are in the transitional region. When applying the correction to Reynolds number less than 2300 (this is the case for the VESDA system), it is expected the trend given in figure 5.1 due to disturbance from the jets should still be correct. Based on this, the correction factor has been adjusted as

$$C_f = -0.6258 \times \left(\frac{Q_{in}}{Q} \right) + 1 \tag{5.4}$$

This is a shift in the Y (C_f) intercept by a factor of 0.23 as seen in figure 5.2
Equation (5.4) also improved the calculated results of the suction pressures in the sampling holes by further 2.8% on average, achieving 90% and better results with various range of disturbance ratios as seen in validation. The possibility of an exponential equation was explored and it was found to offer no significant advantage over the simpler straight line model.

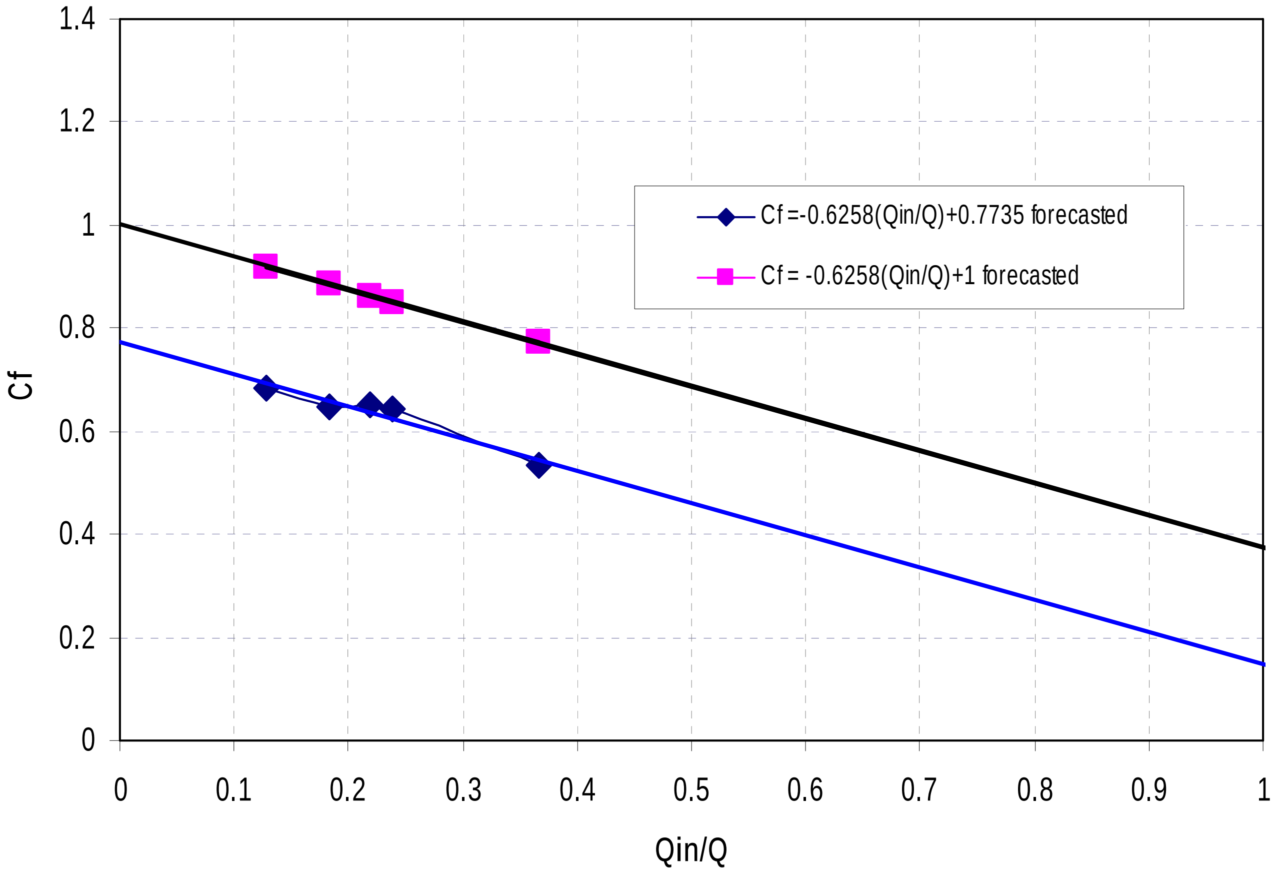

Figure 5.2 Showing a shift in *Y* intercept of equation 5.2 by factor of 0.23

Darcy's equation can now be written as

$$P_{loss} = \left[\left(\frac{64}{\mathrm{Re}\left(-0.6258 \times \left(\frac{Q_{in}}{Q} \right) + 1 \right)} \times \frac{L}{D} \right) + \sum K_f \right] \frac{V^2}{2} \rho \qquad (5.5)$$

5.2 Transport Time Calculation

In this section, the model for calculating transport time is developed.

A series of experiments were carefully conducted on a two pipe system of 100m long as shown in figure 5.2

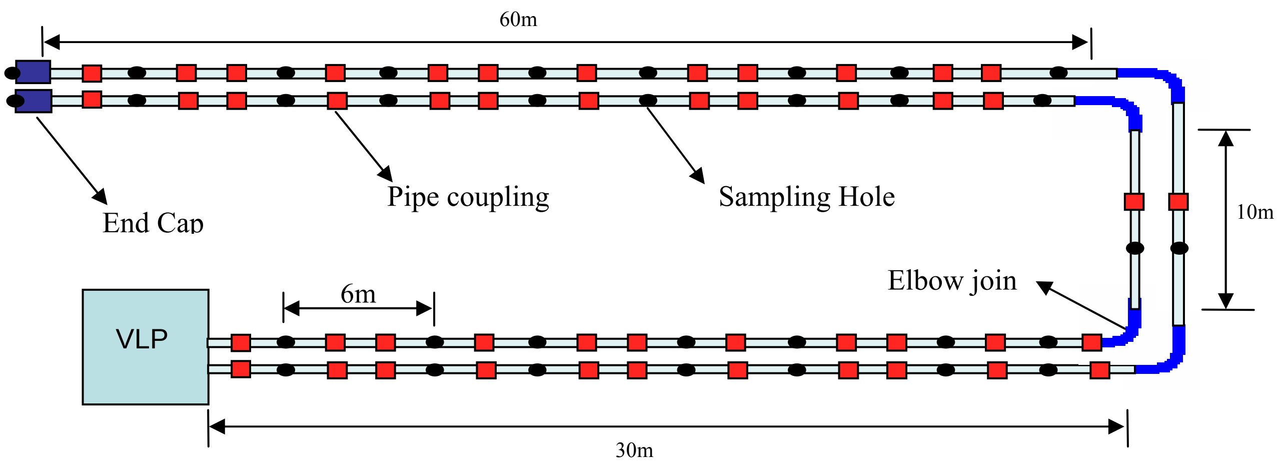

Figure 5.2 Experiment set up for transport time

For analysis purposes, the transport time for pipe 1 was used. Transport time from the end cap (the last sampling hole) is measured and calculated using four different scenarios in order to fine tune the final equation to predict the transport time in all VESDA installations to an acceptable accuracy

The transport time from the end cap was chosen because it is disturbed by 16 jet injections (sampling holes) over the length of the pipe. A pipe of 100m represents the longest practical length (for VESDA installations) and was used because it represents the most difficult problem to model. A model that accurately predicts the transport time for the longest length is expected to predict the transport time for shorter pipe lengths with high level of confidence. The experimental validation to be presented later supports this expectation.

Preliminary experiments showed that the transport time, obtained by summing the time in each segment, using:

$$T_t = \sum_{i=n}^{n} T_{si} \tag{5.6}$$

$$\text{where, } T_s = \frac{L_s}{V_s} \tag{5.7}$$

was not accurate enough. Here T_s is the time for smoke to travel in a segment, L_s is the length of the segment, V_s is the average velocity of air in the segment, and T_t is the total transport time. The results obtained using the above formulae were not in agreement with the measured results and varied by 20% to 37%.

Cole (1999) suggested that a significant proportion of smoke would be entrained within the core of the pipe flow; therefore, the core velocity would dominate any measurement of smoke transport time and for laminar flow be about two times the average velocity. From Cole's (1999) observation, equation (5.7) is modified to;

$$T_s = \frac{L_s}{2V_s} \tag{5.8}$$

Equation (5.8) gave errors in transport time ranging from 37% to 50% with the calculated times being shorter than the measured values.

From these results it can be concluded that the velocity in a segment is between V_s and $2V_s$ and a more accurate equation has to be developed which would take into account the factors that determine the actual transport time.

Because of the growing boundary layers in the pipe after disturbances, it is therefore decided to adopt Cole's (1999) developing length equations (2.24) and (2.25) to calculate the smoke transport time.

$$T_{tur} = \frac{D}{1.3V_{mean}}\left[\frac{L}{D} + 13\ln(1.3 - 0.3e^{\frac{-L}{13D}})\right]$$

$$T_{lam} = \frac{L + 26D\ln\left[(\lambda - (\lambda - 1)e^{\frac{-L}{26D}}\right]}{2V_{mean}}$$

Here T_{lam} means transport time when flow is laminar and T_{tur} means transport time when the flow is turbulent.

From the simulated results in chapter 4 it is apparent that the nature of flow in pipe installations for VESDA, and similar applications, makes it is difficult to distinguish whether the flow is turbulent or laminar. Low Reynolds number does not necessarily mean laminar flow. Cole's (1999) transport time equations were tried and errors up to 50% were found; therefore, a more accurate transport time equation will need to be determined.

To derive a more accurate equation for transport time, it was assumed that the extra transport time caused by the jet induction disturbance is proportional to an extended length (L_T) which is a function of Q_{in}/Q.

$$L_T = f\left(\frac{Q_{in}}{Q}\right) \tag{5.9}$$

A new extended length (L_T) can be expressed as being proportional to L_D, the developing length plus the measured length L of a pipe segment, and a liner relationship is assumed to start with,

$$L_T \propto \left(\frac{Q_{in}}{Q}\right) \times L_D + L \tag{5.10}$$

Here L_D is Cole's (1999) developing length,

$$L_D = 26D \ln\left[\lambda - (\lambda - 1)\exp\left(\frac{-L}{26D}\right)\right] \tag{5.11}$$

In order to get an optimum accuracy for transport time, constants were determined by iteration. The extended length, $L_{T,}$ equation now becomes:

$$L_T = \left(20 \times \left(\frac{Q_{in}}{Q}\right) \times L_D\right) + L \tag{5.12}$$

$$T_{Ts} = \frac{L_T}{1.56V} \tag{5.13}$$

The disturbance ratio is implicit in equation (5.13)

$$T_{Thi} = \sum_{i=1}^{n} \frac{L_{Ti}}{1.56V_i} \tag{5.14}$$

Here we assume that the effect on developing length from disturbance is a linear function of Q_{in}/Q.

When expression (5.13) was used, it was found that the transport time results were still in error by about 10%, with the calculated values giving a longer transport time than the measured values. These values were still not accurate enough to meet the requirements as prescribed by the standards for transport time accuracy. For the calculated transport time to adequately match the actual transport time, equation (5.14) required further modification. It was decided that a more accurate extended length, L_T, needed to be determined.

5.3 Derivation of a More Accurate Extended Length, L_T

From previous investigations, it was found that the pre-dominant factor affecting the transport time is the disturbance ratio, Q_{in}/Q. It is therefore decided to compare the disturbance ratio obtained from equation (5.13), to the disturbance ratio obtained by measuring the transport time.

To determine the values of the disturbance ratios for the measured transport time, the transport times were measured in the pipe setup as shown in figure 5.2. Transport times were measured from sampling holes 1 to 17 and a correlation factor was determined.

The transport times results were used to back calculate the disturbance ratio $\left(\frac{Q_{in}}{Q}\right)$

From equation (4.16), transposing for $\left(\frac{Q_{in}}{Q}\right)$

$$\left(\frac{Q_{in}}{Q}\right) = \frac{L_T - L}{20 \times L_D} \text{ , where} \tag{5.15}$$

$$L_T = T_{Ts} \times 1.56V \tag{5.16}$$

To determine the correlation between the two disturbance ratios,

$$\left(\frac{Q_{in}}{Q}\right)_{actual} = \alpha \left(\frac{Q_{in}}{Q}\right)_{calculated} \tag{5.17}$$

$$\alpha = \frac{\left(\frac{Q_{in}}{Q}\right)_{actual}}{\left(\frac{Q_{in}}{Q}\right)_{calculated}}$$

Here $\left(\frac{Q_{in}}{Q}\right)_{actual}$ is the disturbance ratio from pressure calculation data and $\left(\frac{Q_{in}}{Q}\right)_{calculated}$ is the disturbance ratio back calculated from the measured transport time using equation (5.17) and α is the correlation factor.

It was found from analysis that the α value that best matched the data was (Q_{in}/Q). This shows that the effect on the developing length from the jet disturbance is a quadratic function of Q_{in}/Q. From the experimental data, it was found that the transport times can be expressed as,

$$L_T = L + 20L_D \left(\frac{Q_{in}}{Q} \right)^2 \tag{5.18}$$

$$L_D = 26D \ln \left[\lambda - (\lambda_r - 1) \exp\left(\frac{-L}{26D} \right) \right] \tag{5.19}$$

This shows that the effect of the disturbance on the developing length is stronger than that given by a linear function as in equation (5.12).

L_D is the developing length for transport time and L_T is the extension length for transport time.

$$T_{Ts} = \frac{L_T}{1.56V} \tag{5.20}$$

Here V is the velocity of the air in the segment, T_{Ts} is the time for smoke to travel in a segment (from one sample hole to the next), and T_{Th} is the total transport time from the sampling hole.

$$T_{Thi} = \sum_{i=1}^{n} \frac{L_{Ti}}{1.56V_i} \tag{5.21}$$

This represents the most accurate model for transport time, giving a calculated value that is within 95% to 99% of the measured value.

5.4 Summary of the Four Methods of Calculating Transport Time

In method 1, where the core velocity is used and assumed to be twice the average velocity. The transport time is calculated as

$$T_s = \frac{L_s}{2V_s}; \; T_{Thi} = \sum_{i=1}^{n} \frac{L_{fTi}}{2V_i}$$

The calculated transport time using this method is about 50% less than the measured value.

In method 2, the actual length of a segment is divided by the mean velocity and the resulting transport times are summed to give the total transport time. Equations (4.2) and (4.3) were used.

$$T_t = \sum_{i=n}^{n} T_{si} \; ; \quad T_s = \frac{L_s}{V_s}$$

The calculated transport time is about 30% more than the measured value.

For method 3, for each segment, an extension of length L_T was added and divided by $1.56V$. The resulting transport times of each segment is summed to give the total transport time. This method results in a transport time prediction that is 8% more than the measured value. The following equations are used;

$$L_D = 26D \ln\left[\lambda - (\lambda - 1)\exp\left(\frac{-L}{26D}\right)\right]$$

$$L_T = L + 20 L_D \left(\frac{Q_{in}}{Q}\right)$$

$$T_{Ts} = \frac{L_T}{1.56V}$$

$$T_{Thi} = \sum_{i=1}^{n} \frac{L_{Ti}}{1.56V_i}$$

In method 4, correlation factor (5.18) was used and it gave the most accurate results ranging from 95% to 99%. The following equations are used;

$$L_T = L + 20L_D\left(\frac{Q_{in}}{Q}\right)^2$$

$$L_D = 26D\ln\left[\lambda - (\lambda - 1)\exp\left(\frac{-L}{26D}\right)\right]$$

$$T_{Ts} = \frac{L_T}{1.56V}$$

$$T_{Thi} = \sum_{i=1}^{n}\frac{L_{Ti}}{1.56V_i}$$

Figure 5.3 compares the transport times calculated using the above four methods and the measured transport time for a 100 meter long pipe with 17 sampling holes.

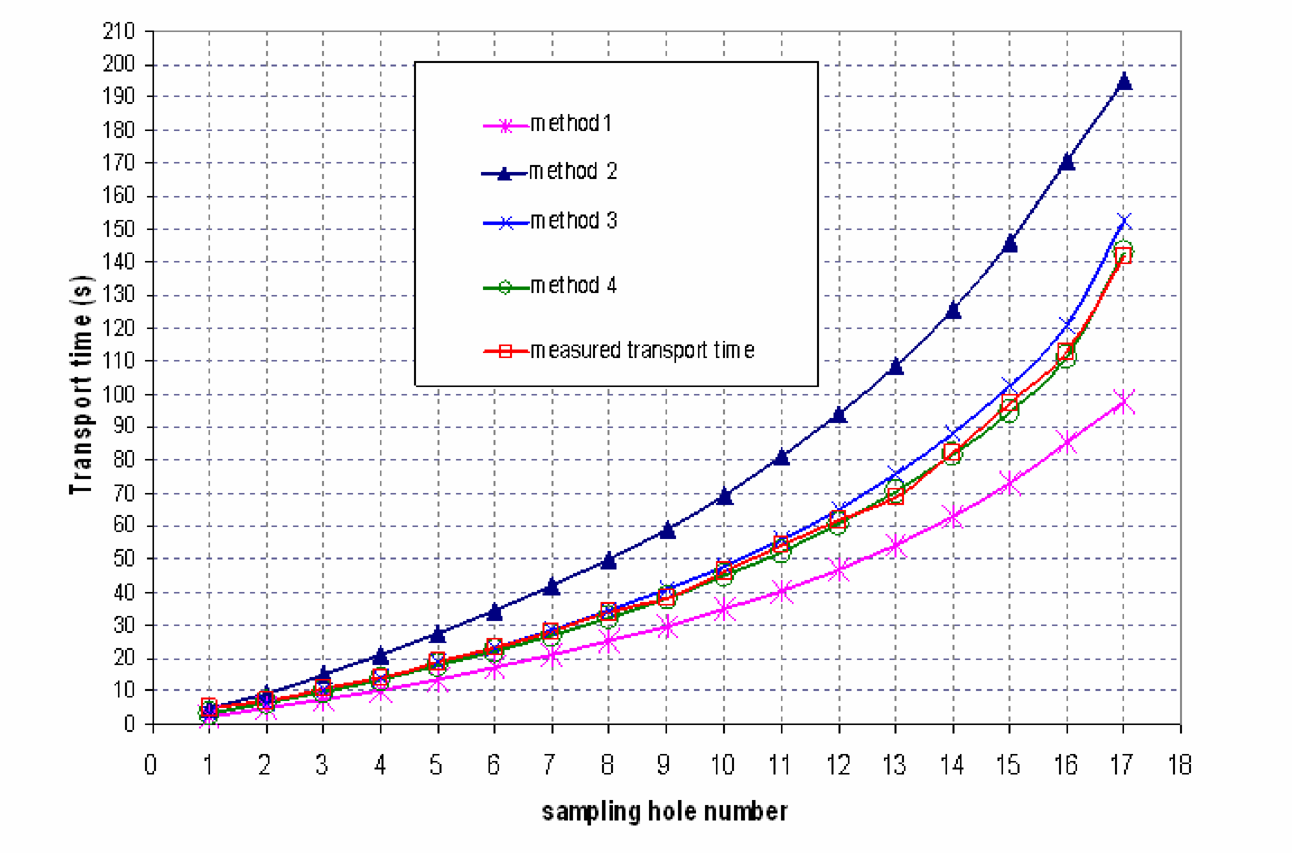

Figure 5.3 Results of different equations used to calculate the transport time.

5.5 Validation

It was first decided to replicate some realistic pipe configurations. After achieving accurate results and gaining a high level of confidence in the ability of the model, further testing was done on a pipe configuration which was beyond VEDSA system recommendations for good installation practice. This was done in order to find the strength and limitations of the new model.

A smoke detection pipe network is constrained by regulatory standards such as AS1670, AS1603, BS5839 and BS6266, which state that the maximum transport time is required to be 60 seconds with allowable error of 10 seconds and that the vacuum pressure drop at the sample hole is to be no less than 25 Pa.

Validation was carried out for the following pipe configurations;

- 2 x 100m pipes with 17 sampling holes in each pipe, figure 5.6
- 4 x 50m pipes with 7 sampling holes in each pipe, figure 5.7
- 4 x 50m pipes with 6 capillary tubes and a ceiling rose assembly as the sampling holes, figure 5.8
- Branched pipe configurations with a total of 6 capillary tubes, figure 5.9

In this section, the mathematical models for predicting pressures at different sampling locations using the friction factors and local loss factors determined in previous chapters are validated using four different network configurations. The transport times from these network configurations are also compared with the models proposed in the last section.

5.5.1 Procedure to Calculate Vacuum Pressure and Transport Time at Sampling Holes.

Flow charts are used to illustrate the sequential steps necessary in order to calculate the vacuum pressure and transport time of the sampling holes as shown in figures 5.4 and 5.5, respectively.

5.5.2 Vacuum Pressure at Sampling Holes

Based upon the relevant parameters for the pipe system, a system operating point is calculated. The methodology proceeds as follows.

1. A first estimate of the system flow rate is made. At the given aspirator speed the system vacuum pressure is calculated at the manifold at the given flow rate. The pressure characteristic equation is used.

2. Vacuum pressure drop is calculated at the first sampling hole, using equation (2.5), where the friction factor is calculated using equation (2.6). If capillary tube is used, then equation (3.14) is used to calculate the vacuum pressure at the ceiling rose.

3. The flow through the first sampling hole is determined by the local vacuum pressure and the hole diameter, using the K value of sampling hole from table 3.1 in equation (3.4) transposing for V. If capillary tube is used, then use equation (3.12) to calculate the velocity and hence the flow in the capillary tube.

4. The flow through the first hole is subtracted from the pipe flow rate to determine the flow in the next pipe segment.

5. Vacuum pressure drop is calculated at the next sampling hole. The process continues until the end of the pipe (end cap), or the vacuum reaches zero.

6. If the vacuum pressure reaches zero before the end cap, then a new flow rate is assumed and the iteration restarts at step 1.

7. If the flow rate in the last segment is the same as or is a close match to the flow rate from the last hole (end cap), then a solution has been found (dynamic equilibrium). If the calculated flow rate is more than the flow rate through end cap, then the system flow rate is decremented and the iteration restarts at step 1. If the flow rate is less than the flow rate from the end cap then the system flow rate is incremented and the iteration restarts at step 1. For the second iteration and until a dynamic equilibrium is achieved, pressure loss in a segment is calculated using equation (5.5)

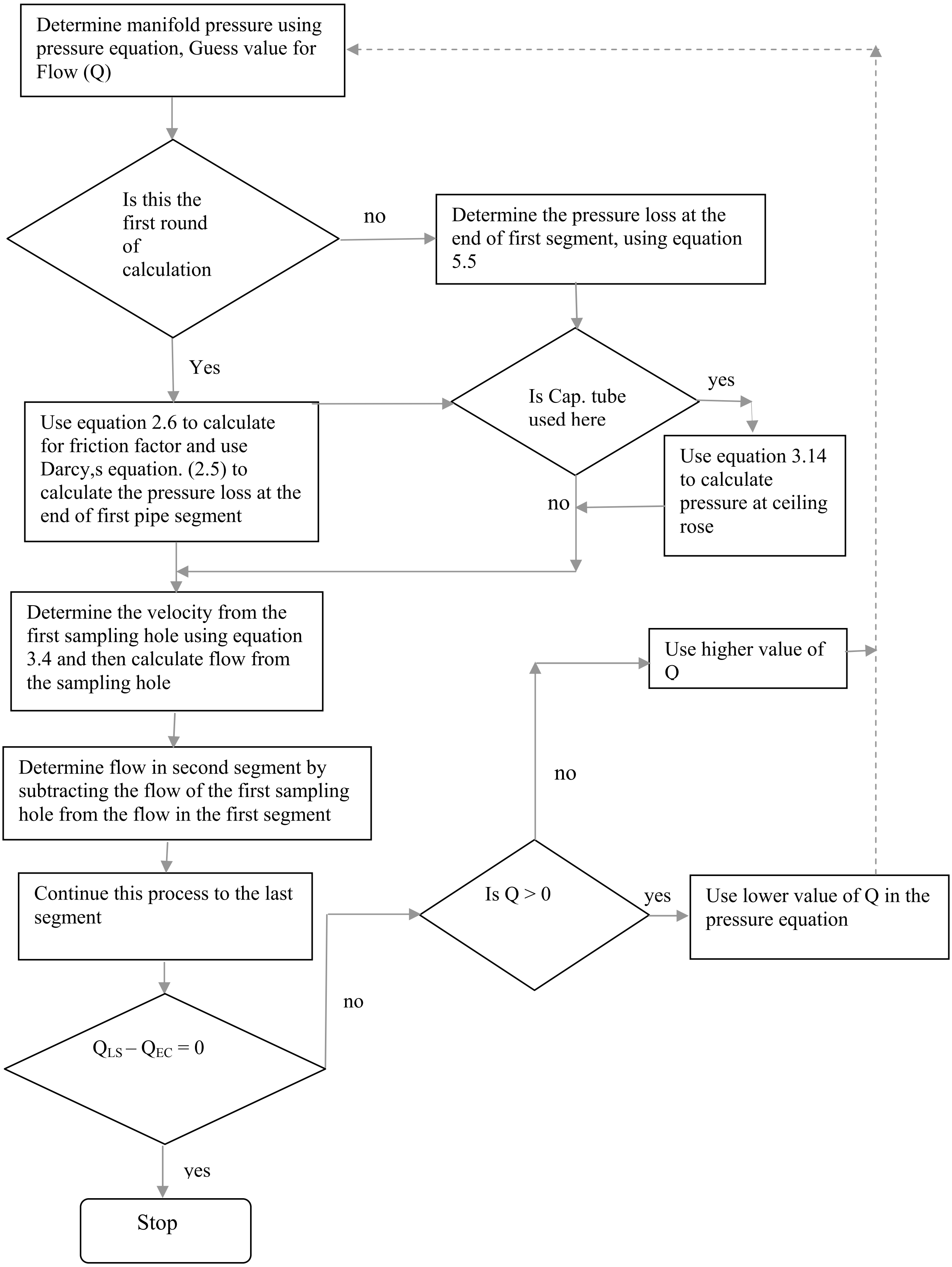

Figure 5.4 Flow chart to calculate vacuum pressure of sampling holes in a pipe configuration

5.5.3 Transport Time Calculation.

When the dynamic equilibrium has been reached for the sampling hole vacuum pressure calculation, the flow rate values are used to calculate the developing length L_D and frictional length L_T for smoke transport time.

The methodology proceeds as follows.

1. The developing length L_D for the last segment is calculated using equation (5.11).

2. L_T for the last segment is calculated using equation (5.18).
   If capillary tube is used then the transport time from ceiling rose to the main pipe is calculated

3. The increments of time delay within each segment is calculated using equation (5.20)

4. The smoke transport time is then available by summing the increments using equation (5.21)

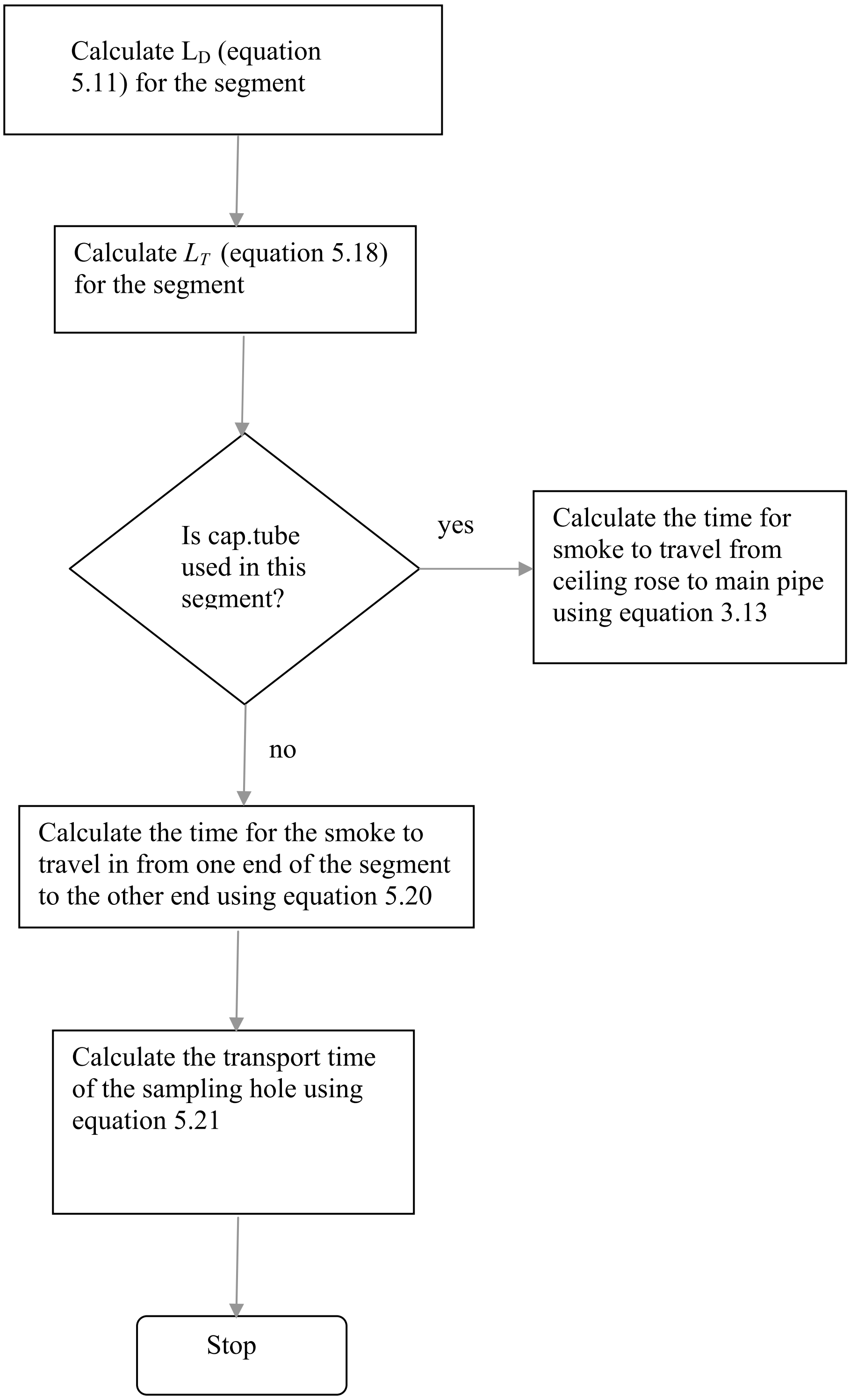

Figure 5.5 Flow chart to calculate transport time of a pipe configuration

5.5.4 Method to Measure Pressure Drop and Transport Time of Sampling Holes.

To measure the sampling hole vacuum pressure, a 3mm hole was drilled close to the sampling hole under test. A flexible tube capable of forming an air tight fit around the peripheral of the 3mm hole was inserted carefully to make sure that it did not protrude past the inside surface of the pipe. A protruding tube would cause further disturbance to flow regime and therefore would give wrong vacuum pressure readings. The other end of the flexible tube was connected to the pressure transducer. After the test the 3mm hole was sealed by wrapping insulation tape around the pipe.

The reason for drilling a 3mm hole beside every sampling hole was that if the flexible tube was inserted in the sampling hole itself, the system flow rate would change and consequently the manifold vacuum pressure would change. This would then give wrong vacuum pressure results.

A hand held digital manometer, model MODUS-MAZ-020P, was used to measure the vacuum pressures at the sampling holes. This instrument has a pressure range of (±) 500Pa with a resolution of 1 Pa. A validated calibration sheet of the instrument indicated an error of (±) 2 Pa over 0 to 500 Pa.

To measure the smoke transport time, smoke was released near the sampling hole under test. The smoke was generated by using a hot soldering iron on a piece of solder wire. A stop watch was started when the smoke reached the sampling hole. When the detector alarmed, the stop watch was stopped and the time was recorded.

The response time of the detector was investigated by injecting smoke in the detector manifold without any pipes attached. It was found that the detector had 2 to 3 seconds response time delay.

The smoke transport time test was repeated on the sample hole for three times and an average transport time was calculated.

All validation was carried out in the VESDA test room. The room measured 62m by 45m. All pipe work was laid on the floor for convenience of pressure and transport time measurement. The air flow in the room was negligible and the temperature of the room was between 22 and 25^{0}C.

Table 5.2 illustrates the names of the symbols used in the different pipe set ups during validation

Symbols	Name
	End cap
	Coupling
	Sampling hole
	Elbow
	Ceiling rose
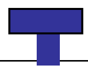	T join

Table 5.2 Symbols and names of pipe fittings used in pipe setup in figures 5.6, 5.7, 5.8 and 5.9

5.6 Validation of 2 x 100m Pipes

Figure 5.6 shows the layout for 2 pipe configuration with 17 sampling holes in each pipe.

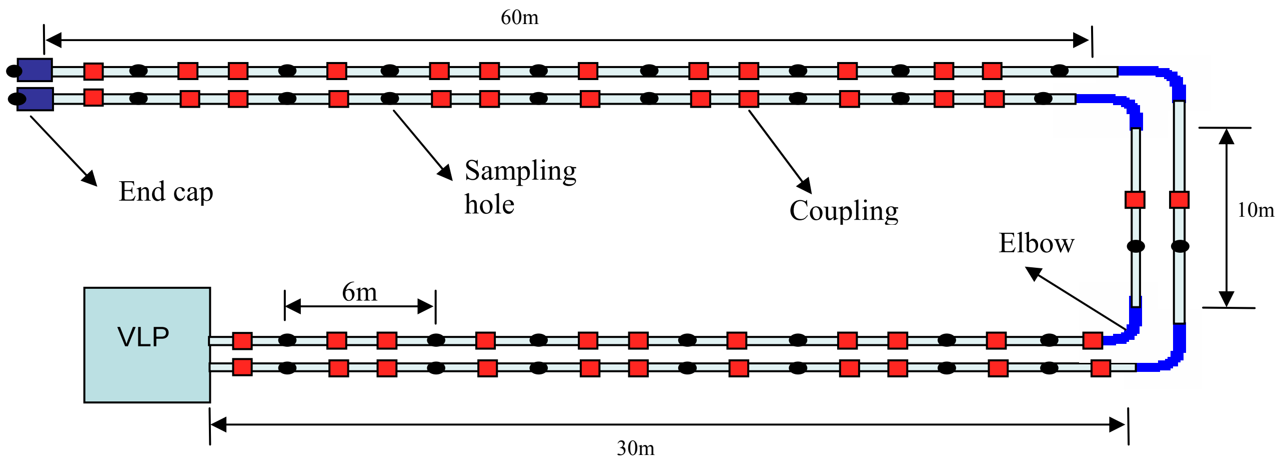

Figure 5.6, Two x 100m pipe set up

Pipe data:

- Sample hole spacing: 6m
- number of sampling holes in each pipe: 17
- number of couplings in each pipe: 24
- Pipe lengths: 100m each
- Number of elbows used: 4

Due to space constraints straight 100m pipes could not be set up hence elbows were used to install the pipes in parallel as shown.

Figures 5.6.1and 5.6.1.1 compares the vacuum pressure of sampling hole and the relative error of the new model and the ASPIRE® model to the measured values. Figures 5.6.2 and 5.6.2.1 compares the transport time from sampling holes and the relative error of the new model and the ASPIRE® model to the measured transport time values. The configurations of both pipes were identical.

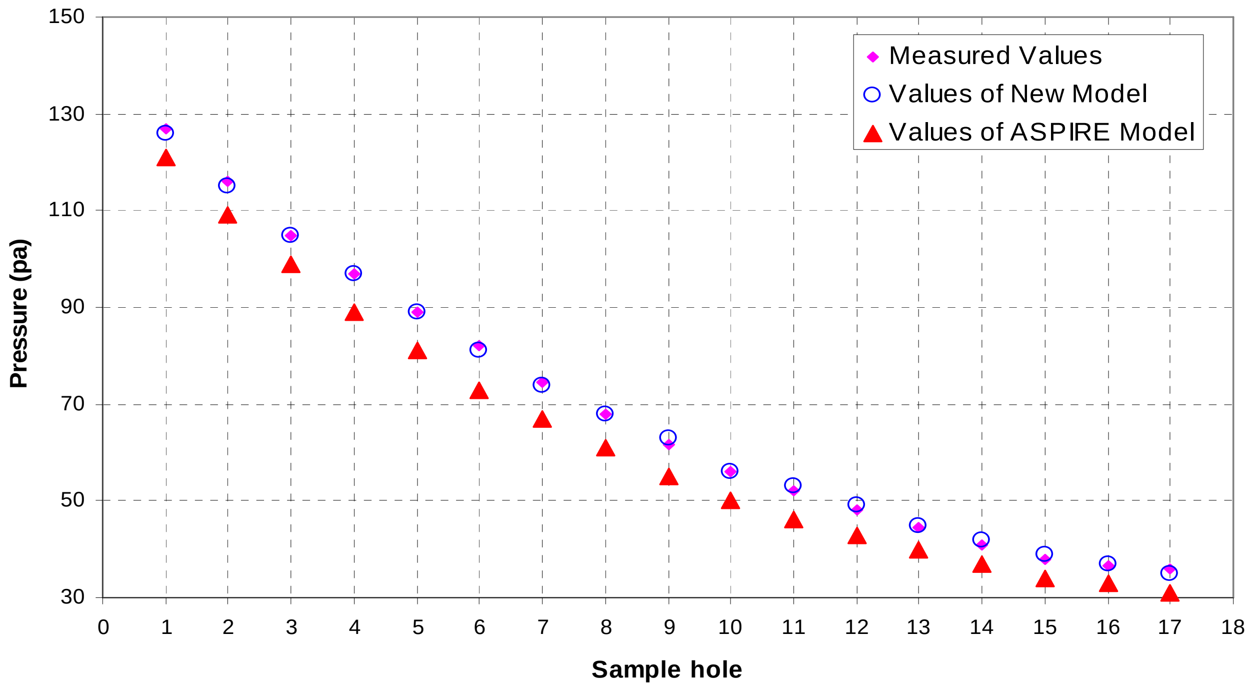

Figure 5.6.1 Test results of sampling hole vacuum pressure comparing ASPIRE® model and New model to the Measured values

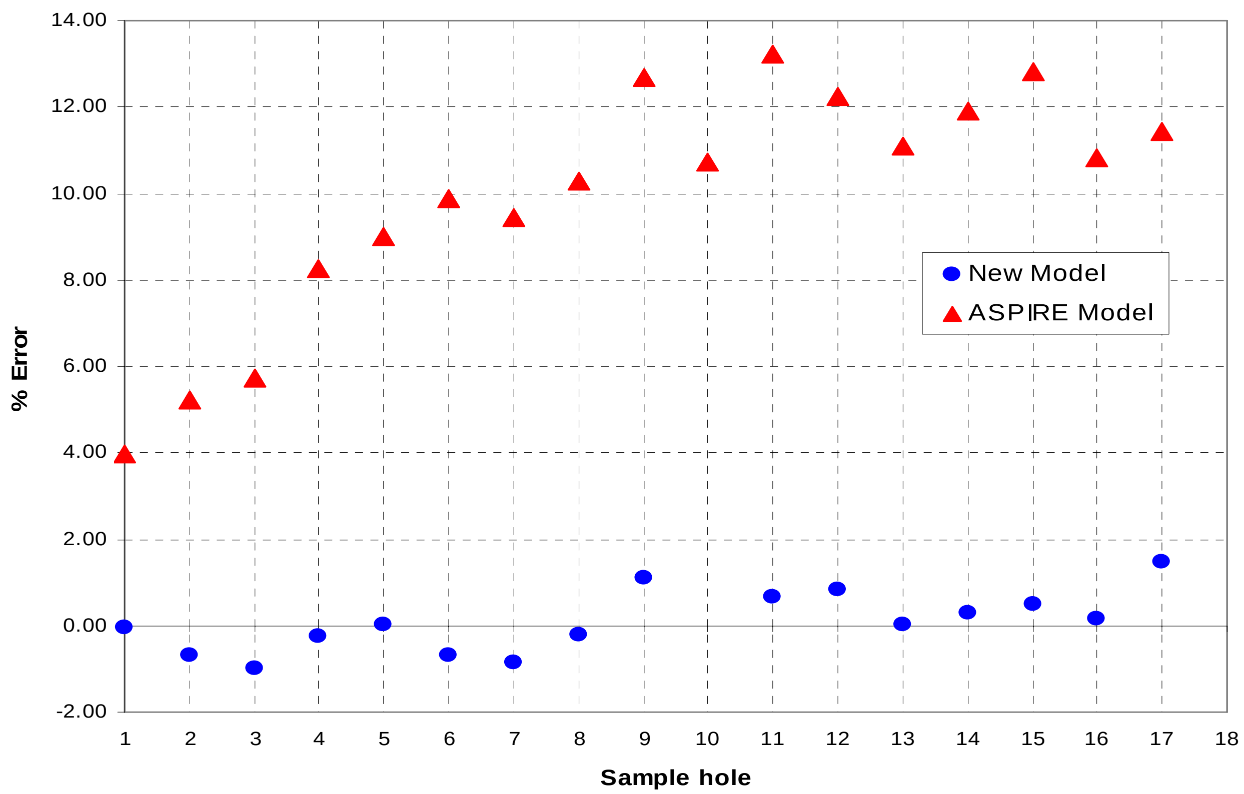

Figure 5.6.1.1 Relative error of sampling hole vacuum pressure of the ASPIRE® model and New model compared to Measured values

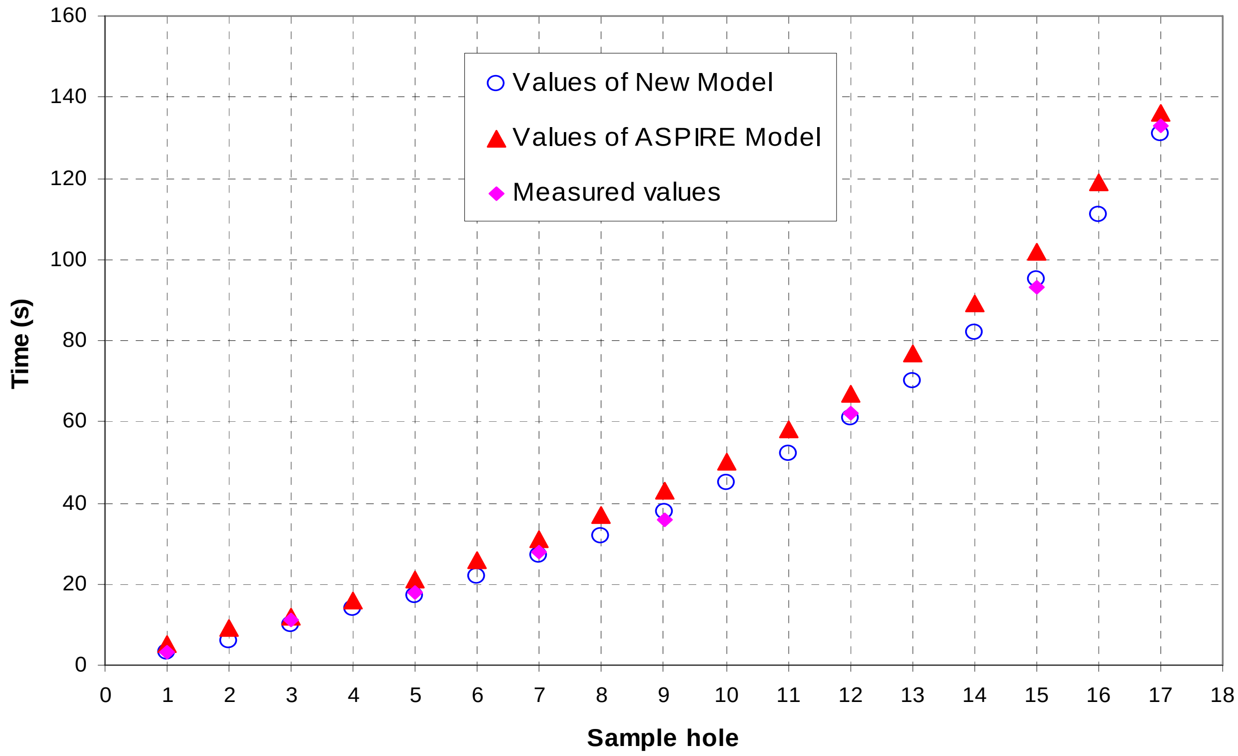

Figure 5.6.2 Test results of sampling hole transport time comparing ASPIRE® model and New model to the Measured values

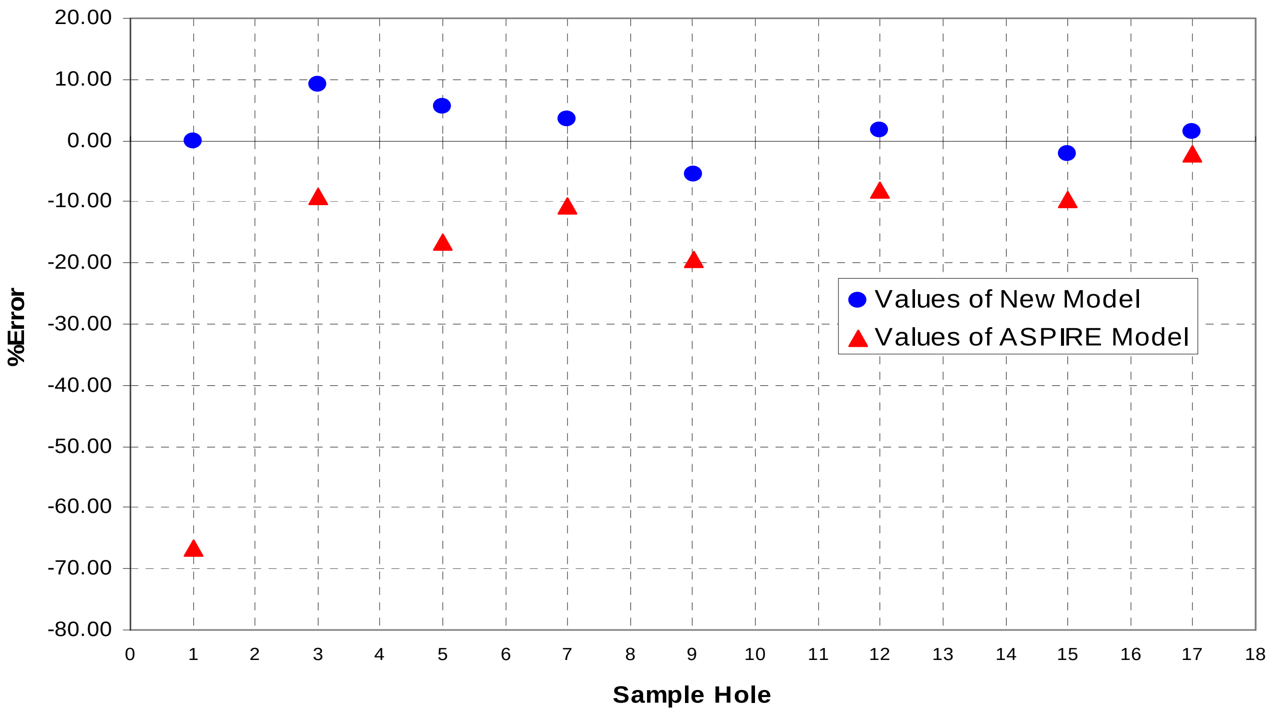

Figure 5.6.2.1 Relative error of sampling hole transport time of the ASPIRE® model and New model compared to Measured values

The transport time was taken from the last sampling hole, which is the end cap and from seven other sampling holes. The reason for this was to get a high enough confidence level that the results predicted by the new model were within the required accuracy. The model can accurately predict well beyond 60 seconds which is further evidence of the validity of the model.

After every transport time test the room had to be purged with clean fresh air by opening the windows and doors of the room and letting in the natural draft fresh air. This was done because at times a small cluster of smoke would enter a sampling hole not under test and cause the detector to alarm at the incorrect time.

The purging duration was determined by the smoke obscuration reading of the detector. The purging process was complete when the obscuration reading went down to zero. This process was time consuming therefore the sampling holes selected were of even spread along the pipe.

The measured vacuum pressure values were within 98% of the values calculated by the new model and the transport time values were within 95%. The measured transport time values were constantly higher than the calculated values. This offset was due to the combination of the delay in response time of the detector and the human error when operating the stop watch. The agreement between the experimental data and the predictions from the new models is expected since the model constants were determined based on the experimental data from this configuration.

The ASPIRE® model predicted the vacuum pressure and transport time within the 90% or 10 seconds of the measured values. It should be noted that in the relative error graph, figure 5.6.2.1, the first point of the ASPIRE model is in error by 70% which is only 2 seconds difference to the measured transport time of 5 seconds, hence the criteria ± 10 seconds must be observed.

These values from the ASPIRE® model were expected. The accuracy decreases as the number of elbows increases and when capillary tubes are used.

5.7 Validation of 4 x 50 m Pipes

Figure 5.7 shows the layout for 4 pipe configuration with 8 sampling holes in each pipe.

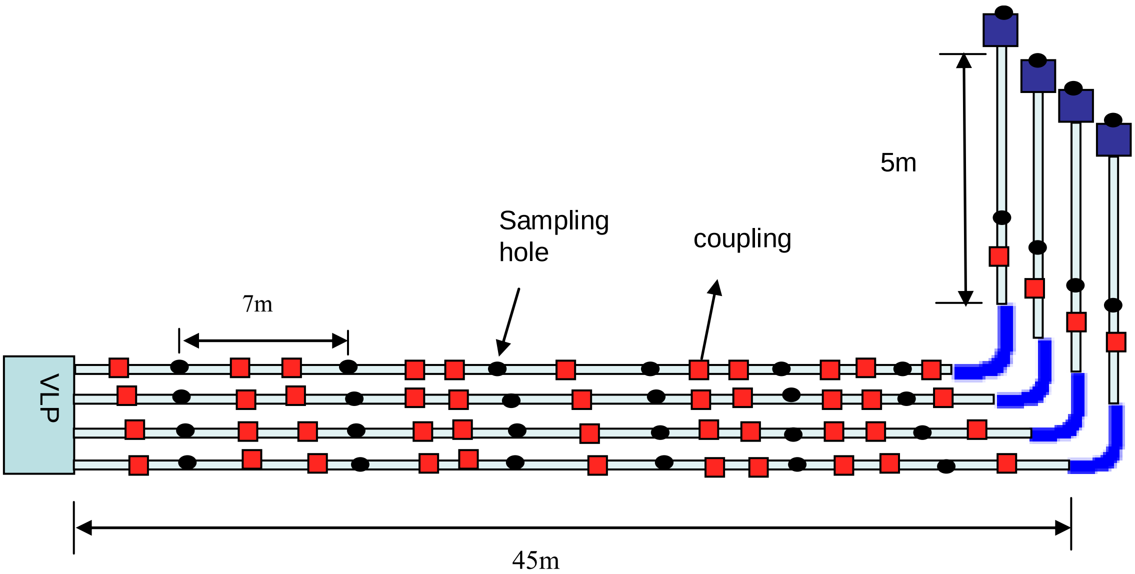

Figure 5.7, Four x 50m pipe set up

Pipe data:

- Sampling hole diameter: 2mm
- End cap hole diameter: 4mm
- No. of sampling hole in each pipe: 8

Figures 5.7.1and 5.7.1.1 compare the vacuum pressure of sampling hole and the relative errors of the new and ASPIRE® models to the measured values. Figures 5.7.2 and 5.7.2.1 compare the transport time from sampling holes and the relative errors of the new and ASPIRE® models to the measured transport time values.

The configurations of the four pipes were identical.

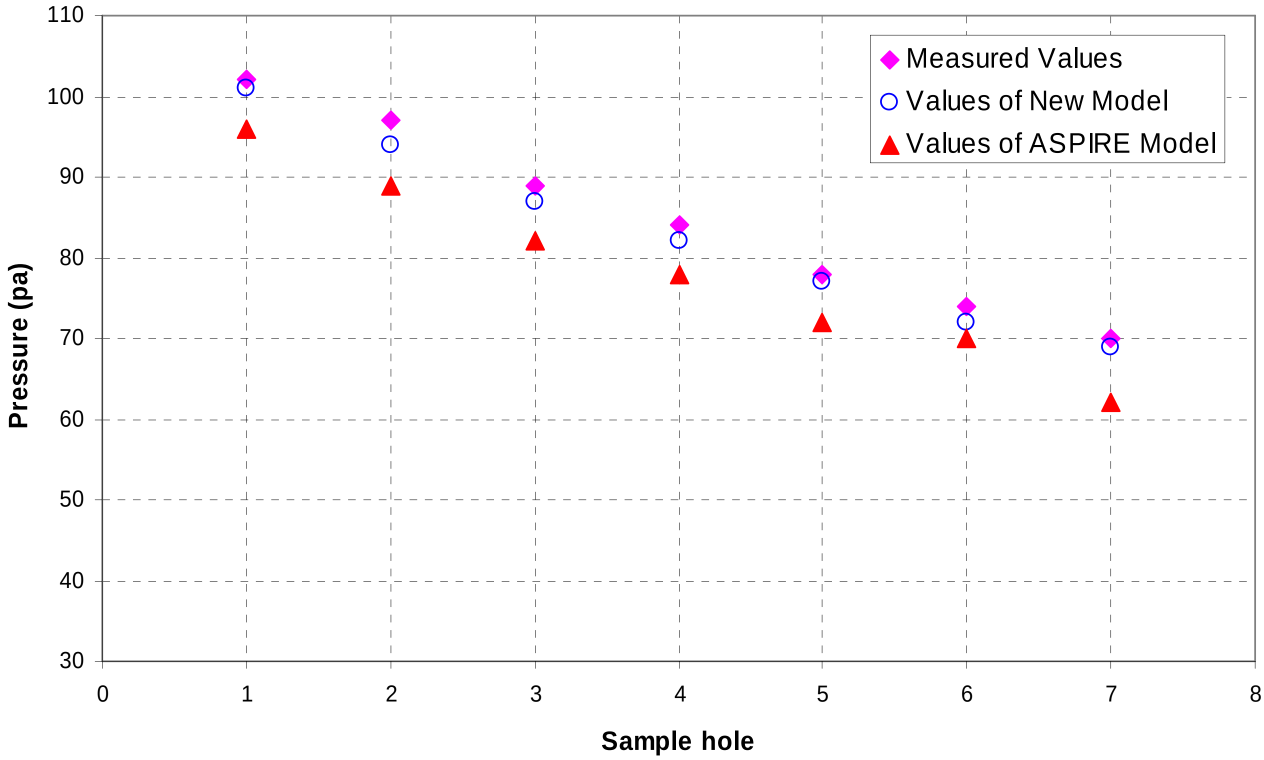

Figure 5.7.1 Test results of sampling hole vacuum pressure comparing ASPIRE® model and new model to the measured values

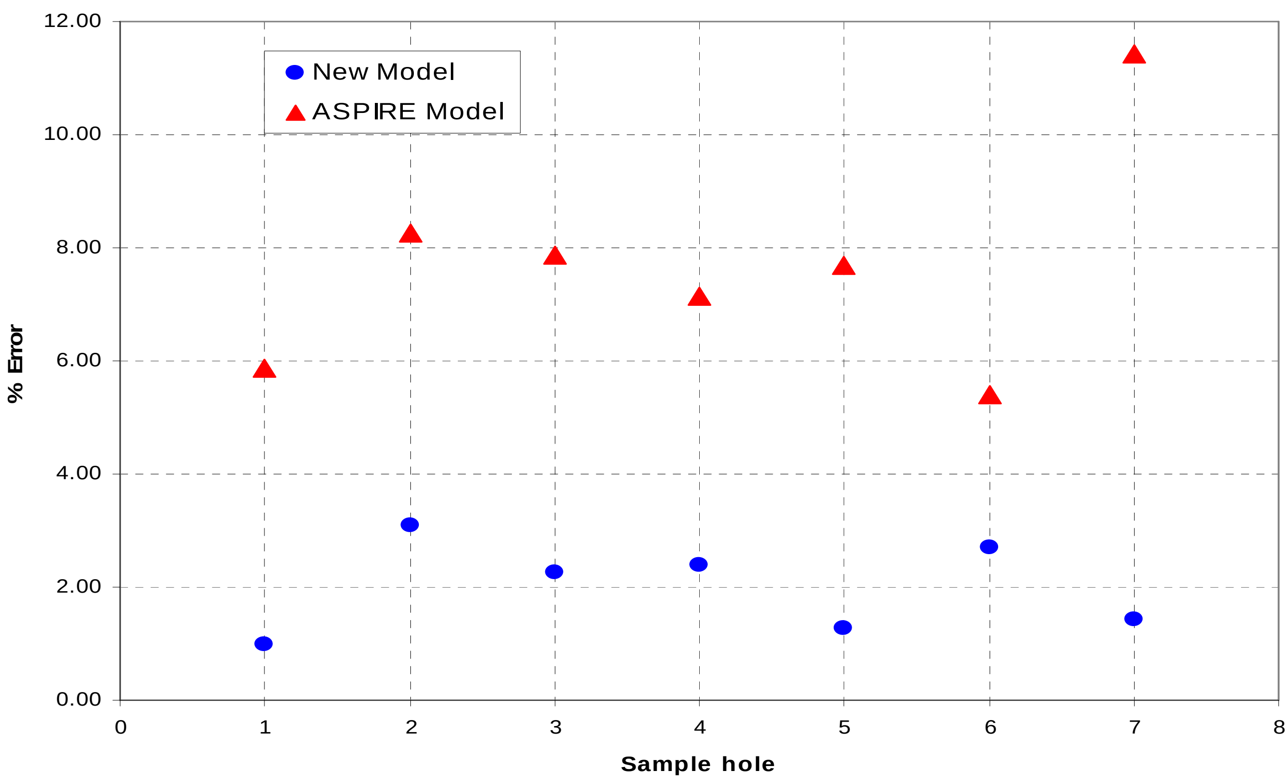

Figure 5.7.1.1 Relative error of sampling hole vacuum pressure of the ASPIRE® model and new model compared to measured values

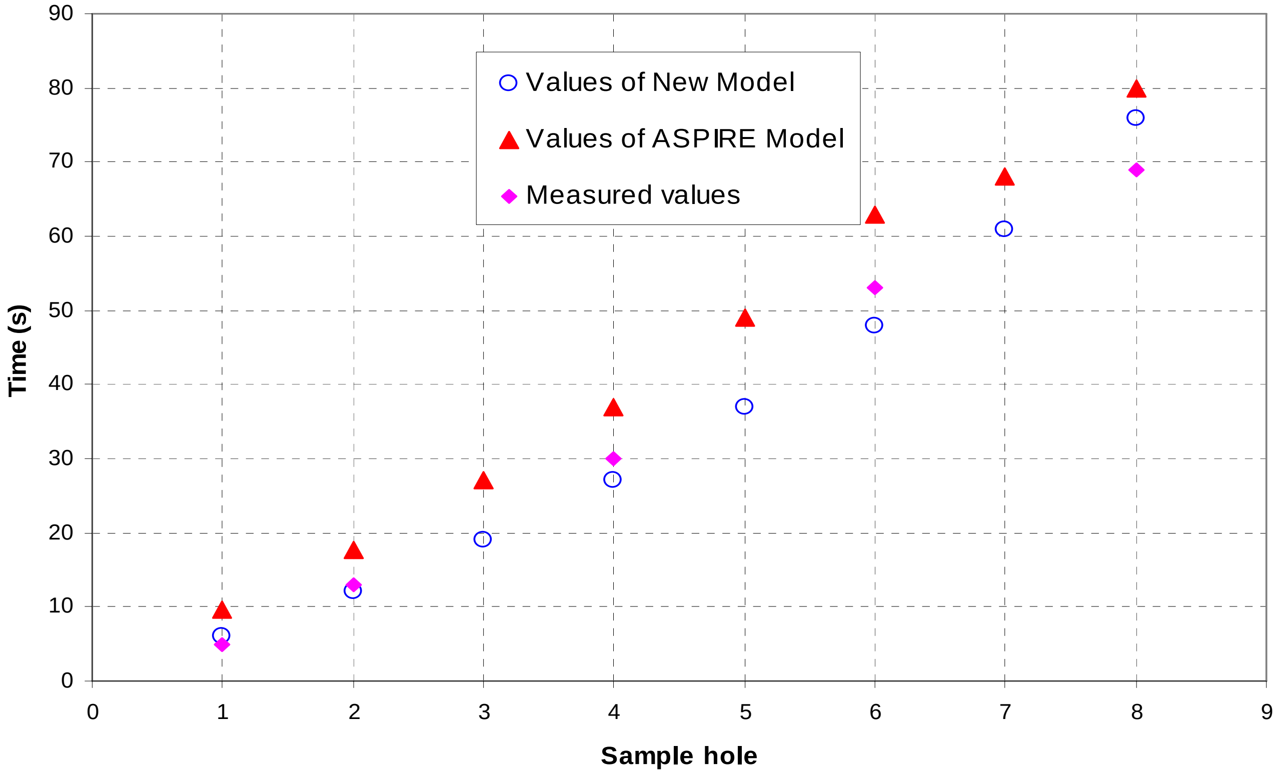

Figure 5.7.2 Test results of sampling hole transport time comparing ASPIRE® model and new model to the measured values

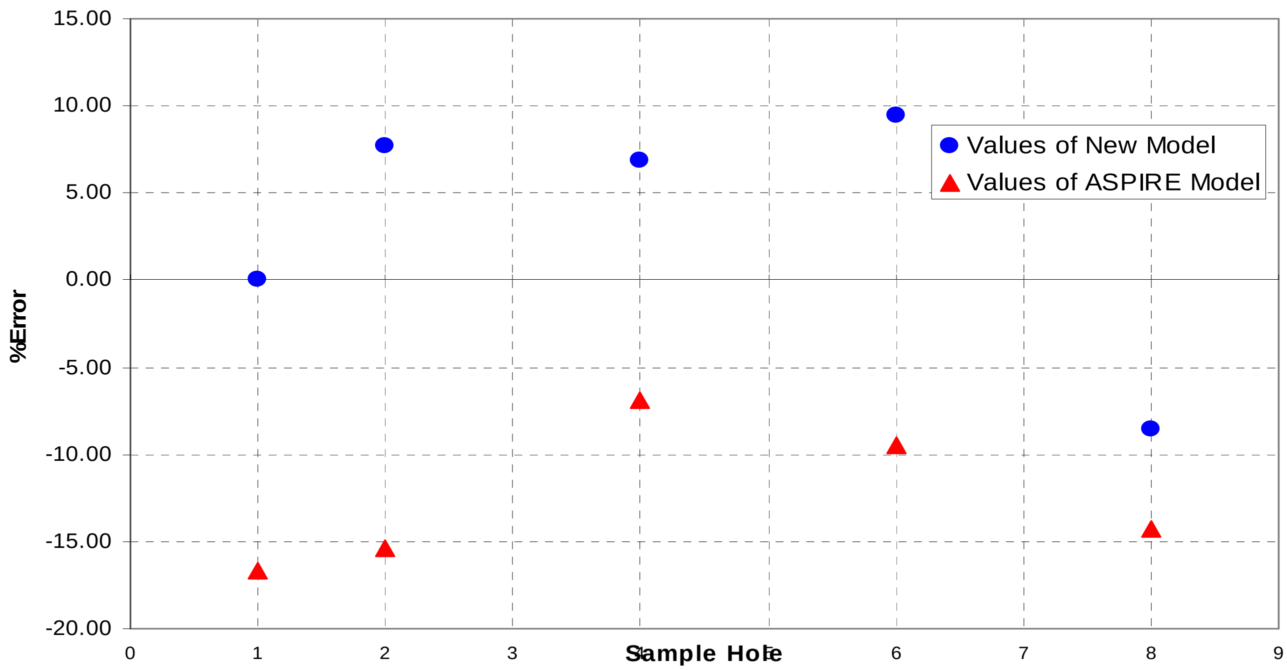

Figure 5.7.2.1 Relative error of sampling hole transport time of the ASPIRE® model and New model compared to Measured values

The measured vacuum pressure values were within 96% of the values calculated by the new model and the transport time values were within 93%.

The ASPIRE® model predicted vacuum pressure values and transport time within 89%. Similar to set up in figure 5.6, this configuration did not have any capillary tubes and the elbows were kept to the minimum of one per pipe.

5.8 Validation of 4 x 50m Pipes with Capillary Tubes

Figure 5.8 shows the layout for 4 pipe configuration with capillary tube and ceiling rose. There are 6 ceiling roses and a 3mm sampling hole in the end cap in each pipe.

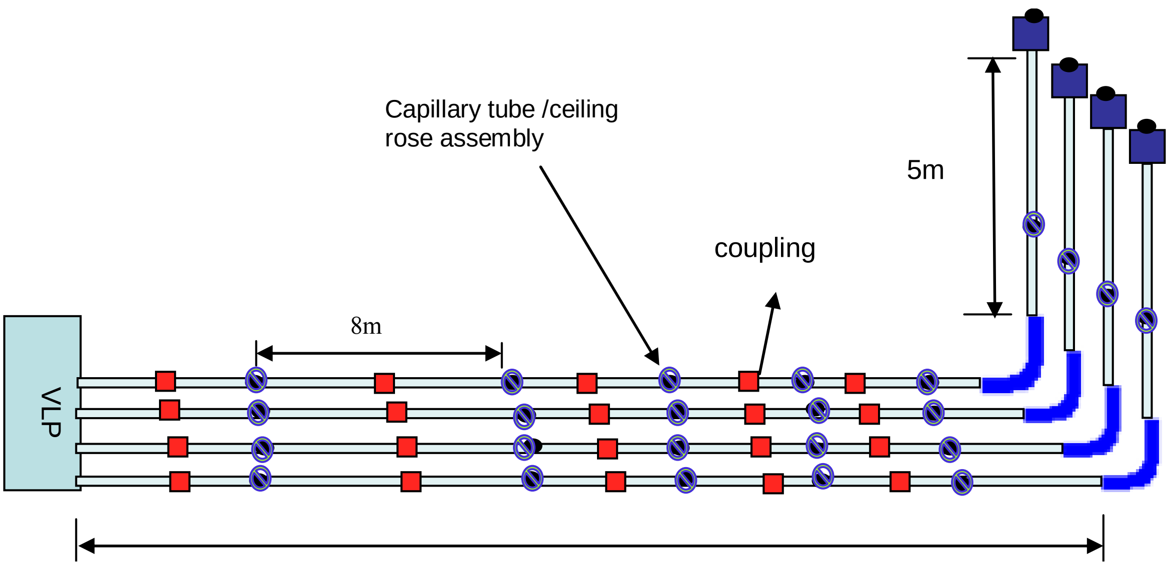

Figure 5.8, Four x 50m pipe set up with capillary tube and ceiling rose

Pipe data:

- Sampling hole diameter in ceiling rose: 2mm
- End cap hole diameter: 4mm
- Total No. of sampling hole in each pipe: 7
- Length of capillary tube: 1m
- Capillary tube spacing: 8 m

Figures 5.8.1and 5.8.1.1 compares the vacuum pressure of ceiling rose and the relative errors of the new and ASPIRE® models to the measured values. Figures 5.8.2 and 5.8.2.1 compares the transport time from ceiling rose and the relative error of the new and ASPIRE® models to the measured transport time values.

The configurations of the four pipes with capillary tubes and ceiling roses were identical. The measured vacuum pressure values were within 98% of the values calculated by the new model and the transport time values were within 95%.

The ASPIRE® model values of vacuum pressures were in discrepancy by 30% to the measured values. This is too inaccurate and does not comply with the applicable standards.

The transport times predicted by the ASPIRE® were within 90% of measured values. The capillary tubes used in this configuration were one meter in length and since the velocity in the tube is relatively high, the time for smoke to travel from the ceiling rose to the main pipe is small. For this reason the error in predicting the transport time values in this configuration are not apparent. If, however, longer capillary tubes were used, the transport time calculated by ASPIRE® model would have been in disagreement by a larger percentage.

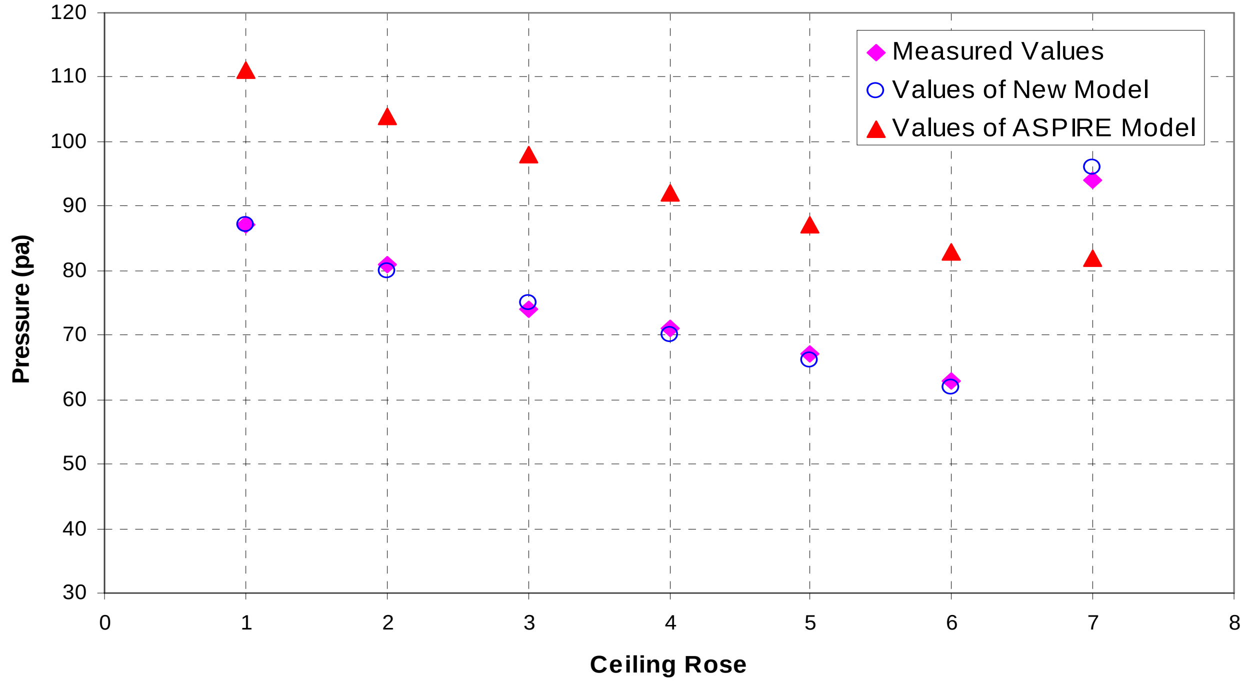

Figure 5.8.1 Test results of Ceiling Rose vacuum pressure comparing ASPIRE® model and New model to the Measured values

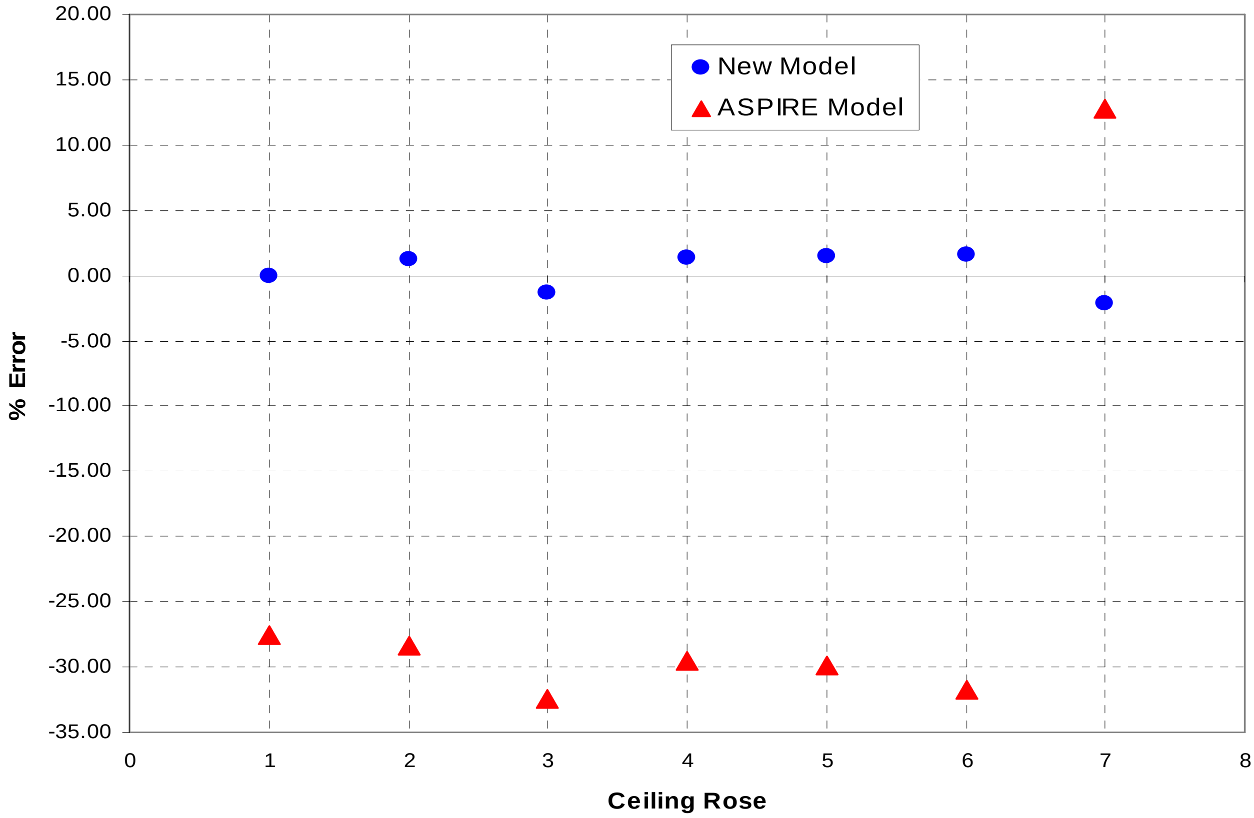

Figure 5.8.1.1 Relative error of sampling hole vacuum pressure of the ASPIRE® model and New model compared to Measured values

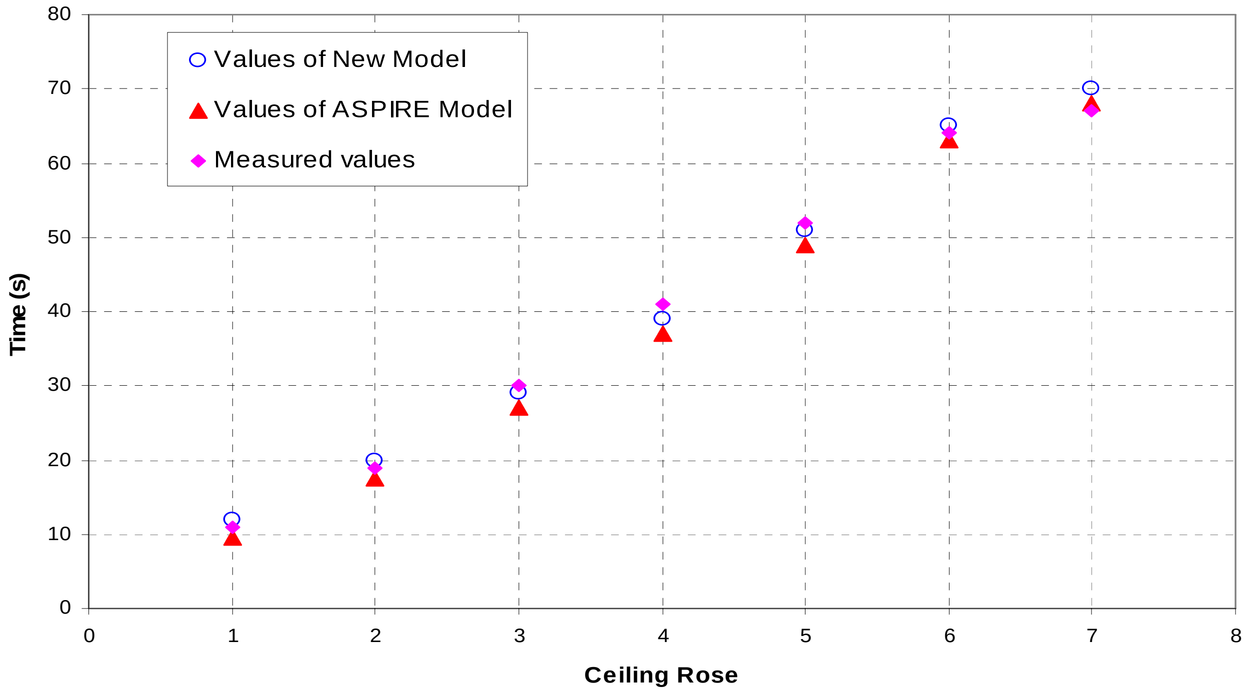

Figure 5.8.2 Test results of Ceiling Rose transport time comparing ASPIRE® model and New model to the Measured values

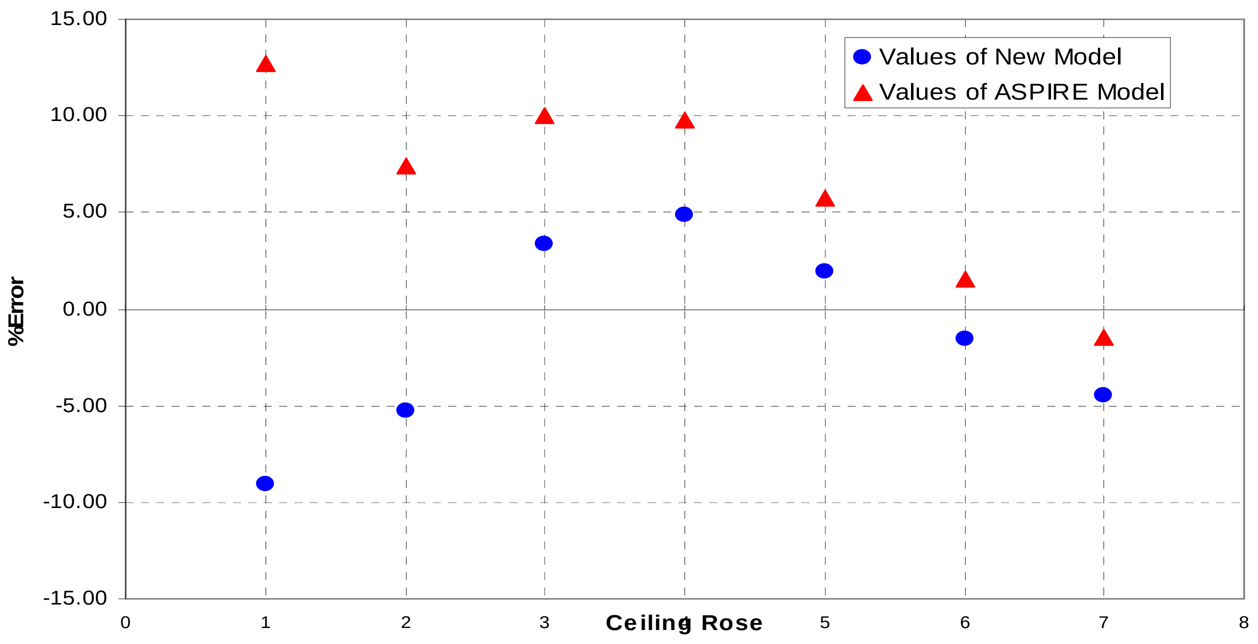

Figure 5.6.2.1 Relative error of Celing Rose transport time of the ASPIRE® model and New model compared to Measured values

5.9 Validation of Branched Pipe Configuration with Capillary Tubes.

Figure 5.9 shows the layout for the branched pipe configuration with capillary tubes.

Pipe Data;

- Capillary tube length: 1m
- Sampling hole diameter: 2mm
- End cap hole diameter: 4mm

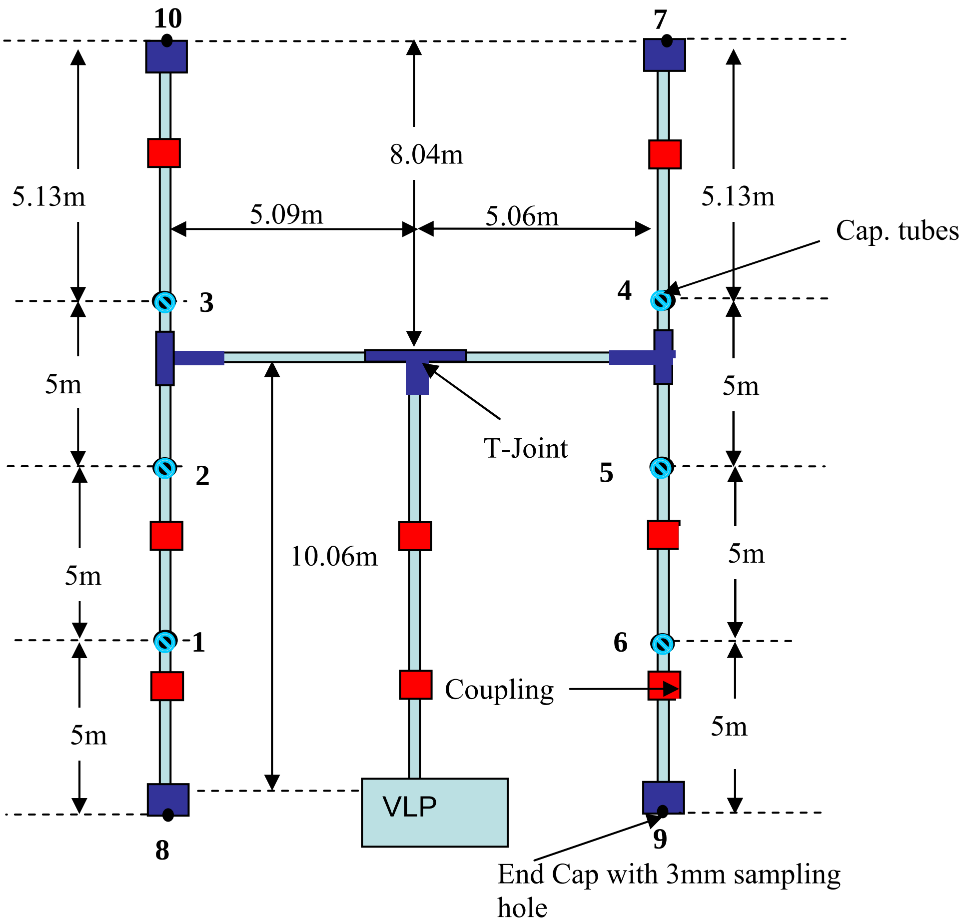

Figure 5.9 A branched pipe set up with capillary tubes

Figures 5.9.1and 5.9.1.1 compares the vacuum pressure of ceiling rose (branched pipe configuration) and the relative error of the new model to the measured values. Figures 5.9.2 and 5.9.2.1 compares the transport time from ceiling rose and the relative error of the new model to the measured transport time values.

It should be noted that the ASPIRE® model does not have the algorithm for branched pipe configurations. Therefore, the comparison in this validation test is made between the new model to the measured values only.

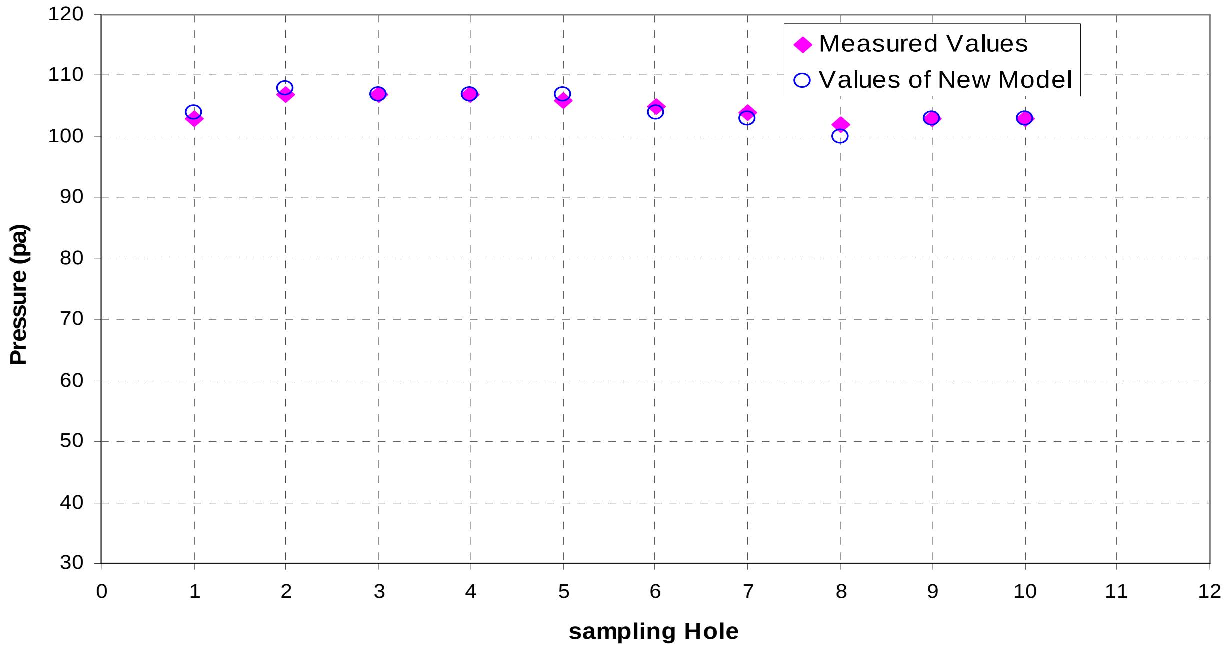

Figure 5.9.1 Test results of Ceiling Rose vacuum pressure comparing New model to the Measured values

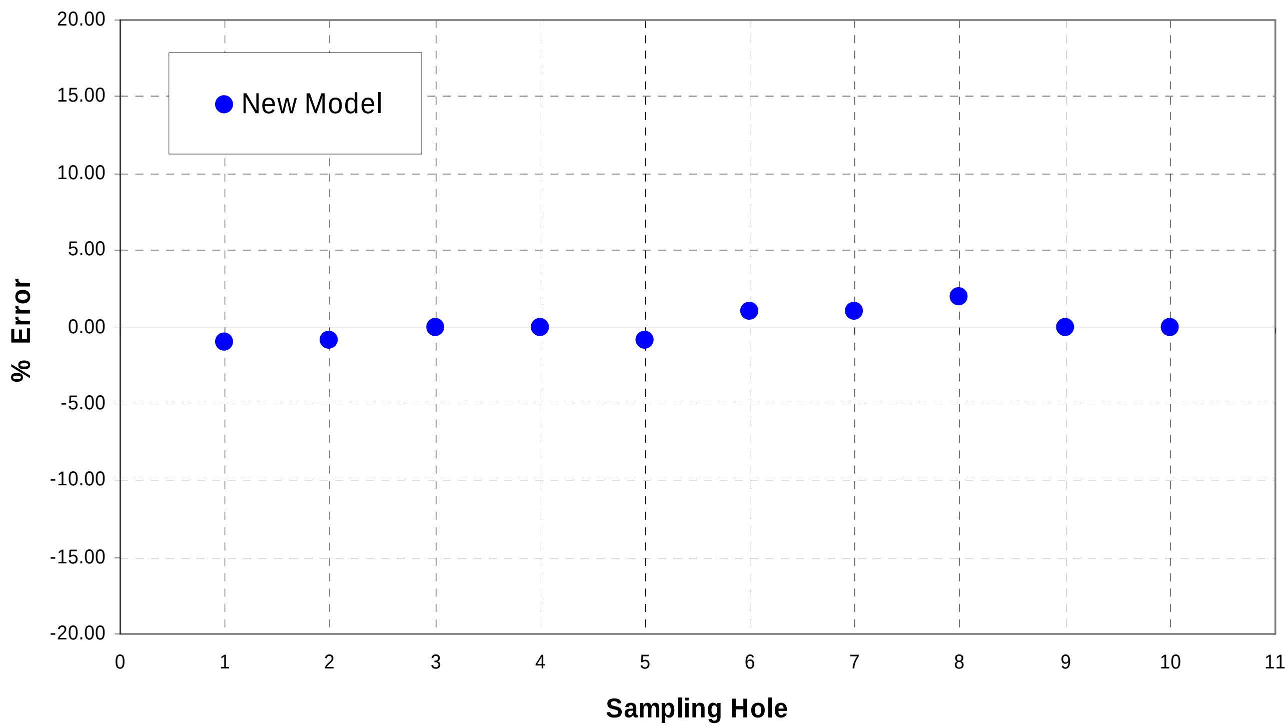

Figure 5.9.1.1 Relative error of Ceiling Rose vacuum pressure of the New model compared to Measured values

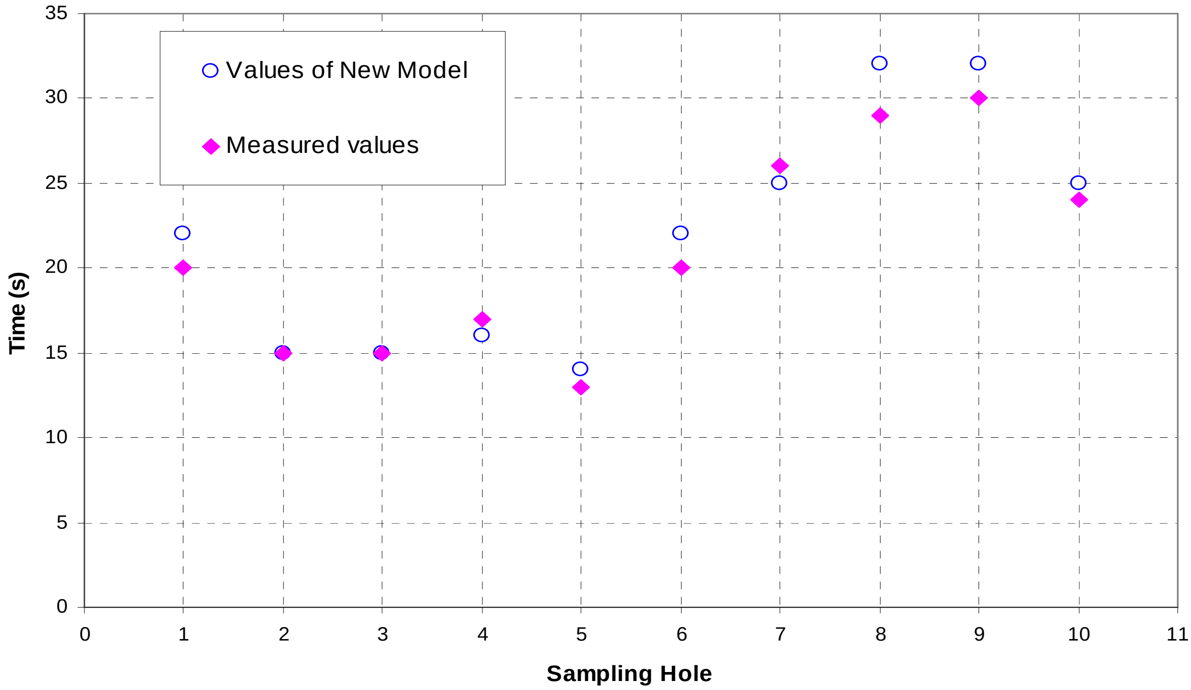

Figure 5.9.2 Test results of Ceiling Rose transport time comparing New model to the Measured values

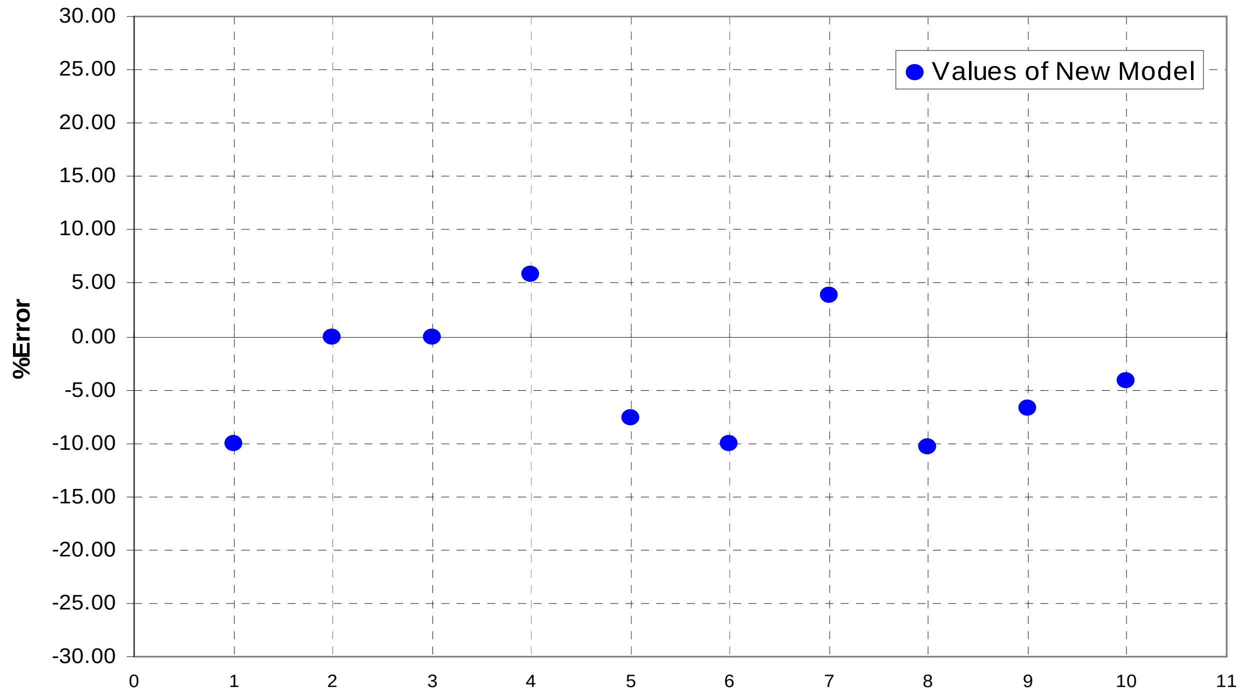

Figure 5.9.2.1 Relative error of Ceiling Rose transport time of the New model compared to Measured values

The measured vacuum pressure values were within 98% of the values calculated by the new model and the transport time values were within 90% where the maximum error in transport time was 3 seconds. These values are well within the accuracy requirements of the standards.

The new model predicted vacuum pressure values of sampling hole within 95% and transport time within 90%. These results give high level of confidence that the new model is capable of predicting the sampling hole vacuum pressures and transport time within the required accuracy for the VESDA installations.

CHAPTER 6

CONCLUSIONS

The literature survey presented in this research thesis showed that there was a significant shortfall in the knowledge needed to relate friction factor with disturbance to flow by jet induction.

The ASPIRE® model, based on Cole's (1999) exponential growth equations has limitations. The model is constrained by the number of fittings, the type of fittings used such as capillarity tube and ceiling rose assemblies, and most importantly by the technique used in determining the friction factor.

Depending upon the flow in the segment, Cole (1999) determines the friction factor by categorising the flow for different regimes in terms of Re, i.e

$$f = 64/Re \quad \text{if } Re < 2280$$
$$f = 0.028 \quad \text{if } 2280 < Re < 2400$$
$$f = 0.028 + 0.007\,(Re - 2400)/600 \quad \text{if } 2400 < Re < 3000$$
$$f = 0.035 + 0.004\,(Re - 3000)/800 \quad \text{if } 3800 < Re < 4400$$

If the flow does not fall in any of above regime then the value for friction factor will be incorrect. Also from the results of CFD simulations carried out, it was seen that the friction factor determined by the equation, $f = 64/Re$ for laminar flow is not valid in situations where jet disturbances exist.

To improve the available technique for mathematically modelling the performance of aspirated smoke detection systems, the following work was carried out.

1. CFD simulations were performed for different jet disturbance scenarios.

2. The CFD results were analysed and the results of the local loss coefficient of the sampling hole and the friction factor values were compared with commonly accepted values

3. From the CFD results it was clear that the local loss coefficients were required to be experimentally determined since the values determined from text book were in disagreement. The friction factor values were also in disagreement as can be seen from figure 4.6.

4. A new mathematical model was developed to calculate the friction factor which is a function of the disturbance ratio (Q_{in}/Q), in the flow regime which the VESDA systems are normally operated at. Having developed the model, pressure loss in a pipe segment was calculated using equation 5.5

$$P_{loss} = \left[\left(\frac{64}{\mathrm{Re}\left(-0.6258 \times \left(\frac{Q_{in}}{Q} \right) + 1 \right)} \times \frac{L}{D} \right) + \sum K_f \right] \frac{V^2}{2} \rho$$

5. For the VESDA system, the transport time, the development length equation (5.11) and the extension length equation (5.18) were developed. A correlation factor of the disturbance ratios was determined which improved the prediction of the transport time to required accuracy.

$$L_D = 26D \ln\left[\lambda - (\lambda - 1) \exp\left(\frac{-L}{26D} \right) \right]$$

$$L_T = \left(20 \times \left(\frac{Q_{in}}{Q} \right)^2 \times L_D \right) + L$$

Having tested the model on various pipe configurations, the calculated pressure values of sampling holes and the smoke transport time closely matched the measured values.

All the results from the validations were within 90% or better for both the pressure at each sampling hole and transport time.

Validation of the model was undertaken by testing pipe configurations of 100m length, pipe configurations with capillary tubes and branched pipe configurations. The ASPIRE® software model is valid only for pipe lengths of less than 100m, it does not model branched pipe configurations and it does not give accurate enough results for configurations with capillary tubes. By testing all four configurations, a level of confidence was achieved that the new models can achieve greater accuracy than that is possible using the ASPIRE® software.

Some of the pipe configurations during validation were deliberately set up to be beyond the recommended VESDA installation practice. These configurations were chosen in order to determine the weaknesses and limitations of the model and also to provide a high level of confidence so that if such pipe configurations become standard in the future, this new model can be used.

In all cases, the results obtained were always within the target estimates when compared to the measured values.

Comparing the measurements to the results obtained from this new model and to those of the ASPIRE® software model, the improvement in accuracy for every configuration is 5 % or better. As the number of fittings (elbows, T-junctions, Y-junctions, etc.) increases, the accuracy of the ASPIRE® model drops proportionally.

In capillary tube configurations, the new model shows an improvement in accuracy of up to 30%, especially in the pressure drop at the ceiling rose.

Branched pipe configurations are beyond the capability of the ASPIRE® model.

The algorithms used in the ASPIRE® software was finely tuned for a VLP unit and simple pipe configuration. As Cole (1999) stated 'it is necessary to manually adjust the linear term of the aspirator characteristic curve by a factor of 0.47 for 3000rpm, 0.57 for 3600rpm and 0.72 for 4200rpm.'

Also, for local losses in the main pipe caused by various fittings, Cole (1999) represents the losses as frictional loss. Cole's methods to determine these losses (described in chapter 2) puts constrain on the number of fittings to be used in an installation for the ASPIRE® model accurately.

If a new detector or a new type of fitting is introduced, it is very cumbersome and may be impossible to adjust the ASPIRE® algorithms so that the model is accurate.

In summary, the mathematical models developed in this research have the following advantages over the current ASPIRE® model

- Longer sampling pipes can be modelled
- The actual number and type of fittings used (such as elbows, tees or couplings, etc.) in an installation can be modelled and is not limited to four
- A branched pipe network can be modelled
- Capillary tube pipe configurations can be modelled
- Pressure values and the transport times can be predicted more accurately
- Aspirator characteristic equations for new detection systems can be easily added to the model's algorithm.
- The loss coefficient of a new fitting can easily be determined and introduced into a new version of the modelling algorithm

A new version of computer based software has been developed by Vision Fire and Security based on the findings of this research. This new modelling software will allow installers to design systems requiring complex pipe configurations that accurately match the measurements taken and to validate the installation, thereby minimizing the work needed to comply with the regulatory standards. This should increase the likelihood of such systems being correctly installed and commissioned, thereby reducing the risk to human life and property brought about by fire.

This thesis also lays a foundation for further research on smoke particle dispersion and dilution as smoke mixes with clean air in the pipe. A relationship between detector sensitivity and smoke concentration could be established. Further more, the research could also lead to distinguish the difference in light scattering pattern between dust and smoke and consequently reduce false alarms.

REFERENCES

Acarlar, M.S. (1987) A study of hairpin Vortices in a Laminar Boundary Layer, *J. Fluid Mech*. **175**, 1-41

Benedict, R. (1980) *Fundamentals of Pipe Flow*, 3rd edition. A. Wiley – Inter Sciences

Bovendeerd, P.H.M. (1987) Steady Entry Flow in Curved Pipe, *J. Fluid Mech*. **117**, 233-246

Brown, G.O. (1990*) The History of the Darcy-Weisbach Equation for Pipe Flow Resistance*, Biosystems and Agricultural Engineering, Oklahoma State University

Cal, B. P., and Castillo, O. L., (1998) *Self-Simiular solutions in Turbulent Boundary Layers with Suction and Blowing* , Rensseleor Polytechnic Institute

Cole, M., (1999) *Disturbance of Flow Regimes by Jet Induction*, Ph.D Thesis, Victoria University of Technology, Australia

Crowe, C. T., and Robertson, J.A.. (1985) *Engineering Fluid Mechanics*, 5th edition. Houghton Mifflin Company.

Crowe, C. T., and Robertson, J.A.. (1985) *Engineering Fluid Mechanics*, 3rd edition. Houghton Mifflin Company.

Dias, F. (1987) Ideal Jet in Two Dimensions*, J. Fluid Mech*. **185**, 275-288

Douglas, J.F. (1986) *Fluid mechanics Volume 1,* 5th edition. Prentice Hall

Douglas, J.F. (1986) *Fluid mechanics Volume 2,* 6th edition. Pitman Pub

Eugene, A (1987) *Standard Hand Book for Mechanical Engineers*, 9th edition. McGraw Hill

Eastop, T.D. and McConkey, A., (1989) *Applied Thermodynamics*, 4th edition, Longman Scientific and Technical.

Fox, J.A. (1997) *An Introduction to Engineering Fluid Mechanics*, 2nd edition, Macmillan Press Ltd

Gerthart, P.M., and Gross, R.J. (1998) *Fundamentals of Fluid Mechanics*, 2nd edition. McGraw Hill

Gulyan and Agrawal (1996) Explicit Equations for Pipe Sizing *PTQ Autumn. 2000*

He, S. (2000) A Study of Turbulence Under Conditions of Transient Flow in a Pipe, *J. Fluid Mech*. **408,** 1-38

Janna, W.S. (1993) *Introduction to fluid mechanics*, 3rd edition. McGraw Hill

Miller, D.S. (1990) *Internal Flow Systems*, 2nd edition. Gulf Publishing

Miller, R.W. (1983) *Flow Measurement Engineering Handbook*. McGraw Hill

Mironer, A. (1997*) Engineering Fluid Mechanics*, 3rd edition. McGraw Hill

Modi,V. (1987) The Dynamics of the Near Field of Strong Jets in A Cross Flow,
J. Fluid Mech. **177**, 37-47

Mott, R.L (1990) *Applied Fluid Mechanics*, 3rd edition. Merrill Publishing Company

Needham, D.J and Riley N. (1988) A jet in Cross Flow*, J. Fluid Mech*. **8.** 159-184

Notarianni, K.A.(1988) *Modeling Design of Equal Sampling –Rate Multiple Orifice*, United States Patent 5,103,212 files 1992

Potter,M.C., and Wigget,D.C. (2002) *Mechanics of fluids*, 3rd edition. Prentice-Hall

Schaschke, C. (1998) *Fluid mechanics* 3rd edition. McGraw Hill

Soh, W.Y. (1988) Developing fluid flow in curved duct of Square Cross Section and its Fully Developed Dual Solution*, J. Fluid Mech*.**188,** 337-361

Street,R.L.,Watters, G.Z., and Vennard,J.K. (1996) *Elementary Fluid Mechanics*,3rd edition. John Wiley and Sons

Swearingen, C. (1997) *Velocity Profile Deviations and Flowmeter performance,* 2nd edition, American Society of Mechanical Engineers

Taylor, N.A. (1984) *Modeling of Air Flows Through the Sample Pipe of a Smoke Detecting System*, United Kingdom Atomic Energy Authority

Vardy,A. (1999) *Fluid Principles*, McGraw Hill

White, F.M.(1994*) Fluid Mechanics*, 3rd edition. Mc Graw Hill

APPENDICES

Appendix A – VESDA Installation

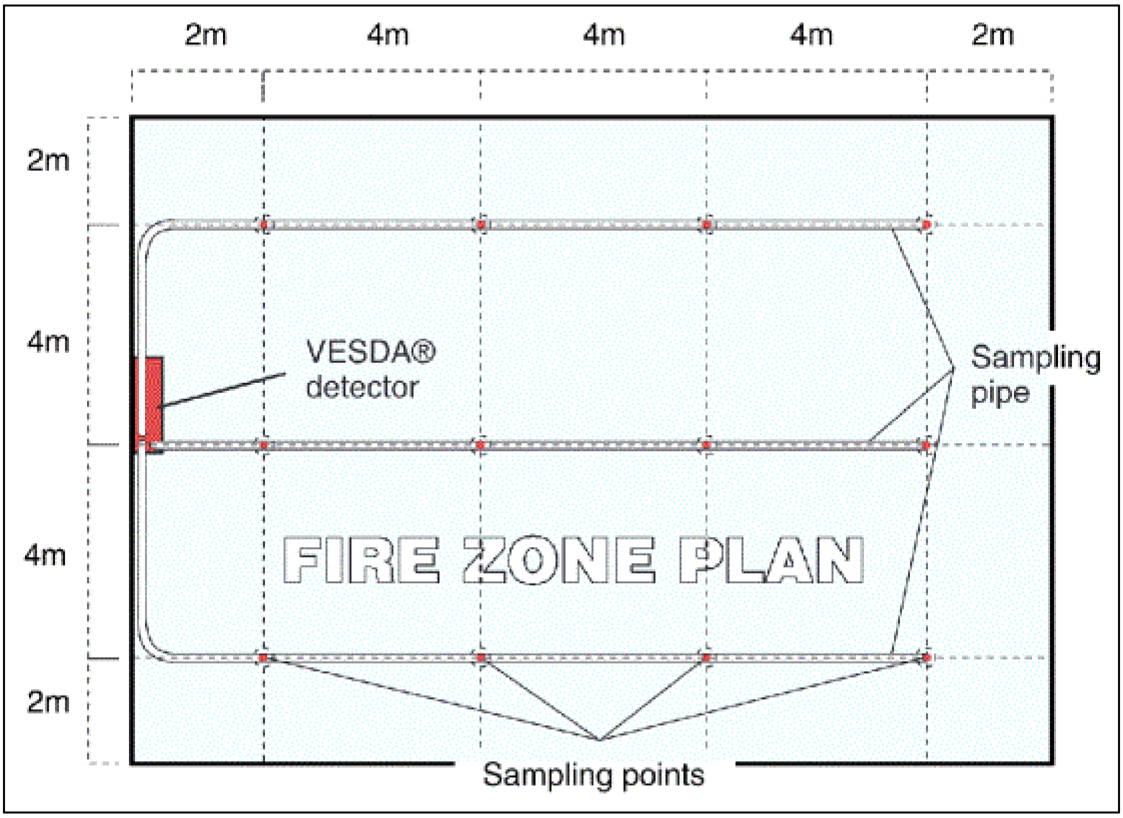

Figure A 1 Grided pipe layout for a typical fire zone

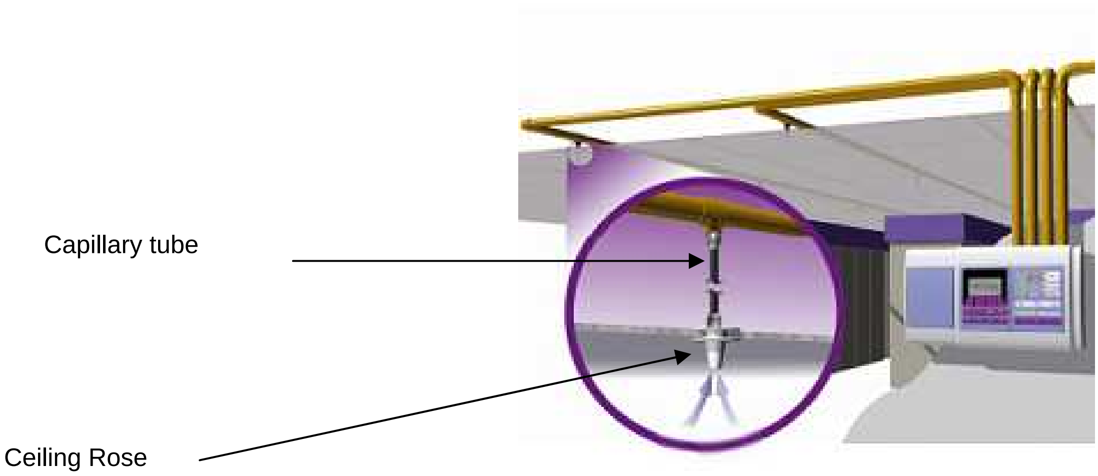

Figure A 2 A magnified view of capillary tube connection

Appendix B - VLP Aspirator Characteristic tables

In this appendix the aspirator performance characteristics of VLP unit were recorded. The pressure equations of the unit were developed from these data.

The aspirator speed for a VLP unit range for 3000 rpm to 4200rpm.

Maximum pressure	
Aspirator speeds (RPM)	Pressure (Pa)
3000	176
3200	202
3400	228
3600	254
3800	287
4000	316
4200	347

Figure B1 Aspirator characteristics of a VLP unit at maximum pressure

3000RPM			
End cap hole dia. (mm)	Pressure (pa)	Velocity (m/s)	Flow rate (l/min)
6	176.159	1.133	27.227
8	162.724	2.130	44.285
10	128.186	2.60	54.226
12	89.943	3.520	73.162
14	65.044	3.994	83.012
16	45.036	4.349	90.391
18	33.802	4.542	94.408
21	23.805	4.749	98.704

Figure B2 Aspirator characteristics of a VLP unit at 3000 rpm

3400RPM			
End cap hole dia. (mm)	Pressure (pa)	Velocity (m/s)	Flow rate (l/min)
6	286.945	1.534	31.883
8	286.613	2.728	56.699
10	215.246	3.435	71.394
12	150.423	4.354	90.494
14	108.382	4.934	102.549
16	75.087	5.453	113.337
18	57.345	5.741	119.322
21	37.896	6.052	125.786

Figure B3 Aspirator characteristics of a VLP unit at 3400 rpm

3800 RPM			
End cap hole dia. (mm)	Pressure (pa)	Velocity (m/s)	Flow rate (l/min)
6	226.524	1.310	27.0277
8	212.249	2.432	50.5477
10	171.048	3.021	62.789
12	118.385	3.879	80.622
14	86.160	4.433	92.136
16	60.946	4.870	101.219
18	45.705	5.108	106.166
21	31.516	5.358	111.362

Figure B3 Aspirator characteristics of a VLP unit at 3800 rpm

4200 RPM			
End cap hole dia. (mm)	Pressure (pa)	Velocity (m/s)	Flow rate (l/min)
6	354.052	1.650	34.294
8	328.752	2.957	61.459
10	266.787	3.794	78.855
12	189.787	4.857	100.949
14	136.951	5.540	115.145
16	96.007	6.090	126.576
18	70.839	6.432	133.684
21	49.167	6.838	142.123

Figure B4 Aspirator characteristics of a VLP unit at 4200 rpm

Appendix C - VLS Aspirator Characteristic Tables

In this appendix the aspirator performance characteristics of VLS unit is recorded. The pressure equations of the unit was developed from these data.

The aspirator speed of a VLS unit range form 3000 rpm to 4200 rpm.

3000rpm			
End cap hole dia. (mm)	Pressure (pa)	Velocity (m/s)	Flow rate (l/min)
blocked	142.810	0	0
6	177.631	1.276	26.523
8	157.731	2.085	43.356
10	134.100	2.608	54.219
12	83.871	3.508	72.913
14	57.069	3.980	82.726
16	40.568	4.294	89.254
18	29.211	4.533	94.221
21	21.733	4.708	97.862

Figure C1 Aspirator characteristics of a VLS unit at 3000 rpm

3400rpm			
End cap hole dia. (mm)	Pressure (pa)	Velocity (m/s)	Flow rate (l/min)
blocked	191.110	0	0
6	229.221	1.277	26.549
8	197.859	2.426	50.431
10	163.749	3.007	62.511
12	101.855	3.806	79.118
14	49.719	4.377	90.897
16	35.174	4.528	94.116
18	21.696	4.665	96.966
21	10.199	4.780	99.367

Figure C2 Aspirator characteristics of a VLS unit at 3400 rpm

3800rpm			
End cap hole dia. (mm)	Pressure (pa)	Velocity (m/s)	Flow rate (l/min)
Blocked	251.28	0	0
6	291.789	1.527	31.75
8	246.908	2.716	56.466
10	232.873	3.242	71.183
12	181.850	4.329	89.995
14	149.610	4.806	101.025
16	115.264	5.431	112.895
18	98.379	5.725	118.999
21	85.739	5.955	123.788

Figure C3Aspirator characteristics of a VLS unit at 3800 rpm

4200rpm			
End cap hole dia. (mm)	Pressure (pa)	Velocity (m/s)	Flow rate (l/min)
Blocked	354.051	0	0
6	360.823	1.641	34.124
8	320.163	2.954	61.41
10	276.401	3.776	78.496
12	205.206	4.789	99.547
14	142.510	5.527	114.886
16	90.048	6.087	126.400
18	58.112	6.398	132.987
21	13.475	6.821	141.774

Figure C4 Aspirator characteristics of a VLS unit at 4200 rpm

Appendix D - VLC Aspirator characteristics Table

In this appendix the aspirator performance characteristics of VLC unit is recorded. The pressure equations of the unit were developed from these data.

The VLC aspirator unit runs on a single speed of 2800rpm.

2800 rpm			
End cap hole dia. (mm)	Pressure (pa)	Velocity (m/s)	Flow rate (l/min)
0	100.824	0	0
6	103.96	0.559	11.618
8	101.18	1.1784	24.492
10	88.77	201496	44.678
12	65.47	3.006	62.477
14	48.441	3.5393	73.561
16	33.961	3.9274	81.628
18	25.31	4.091	85.02
21	17.282	4.3304	90.0004

Figure D1 Aspirator characteristics of a VLC unit at 2800 rpm

Appendix E – Graphs of CFD simulation of different disturbance ratios (Qin/Q)

In this appendix the graphs from simulated data is shown. Simulations were carried out on various disturbance ratios (Q_{in}/Q). These can be seen in figures D1 to D5

From these graphs the actual value of friction is calculated using equation (4.5), which is a transposition of equation (2.5) by solving for *f*.

$$\Delta P = f \frac{L}{D} \frac{V^2}{2} \rho$$

$$f = \frac{2D}{V^2 \rho} \times \frac{\Delta P}{L} \tag{D.1}$$

In equation (D.1), $\frac{\Delta P}{L}$ is the slope of the graphs in the region where the pressure drop occurs linearly due to friction as indicated in figure 4.3

In equation (D.1), ΔP is the pressure drop due to friction, L is the length of main pipe segment where the pressure loss occurs due to friction, V is the mean velocity of air in the main pipe labelled as “outlet” as calculated from the mass flow values in Table 4.1

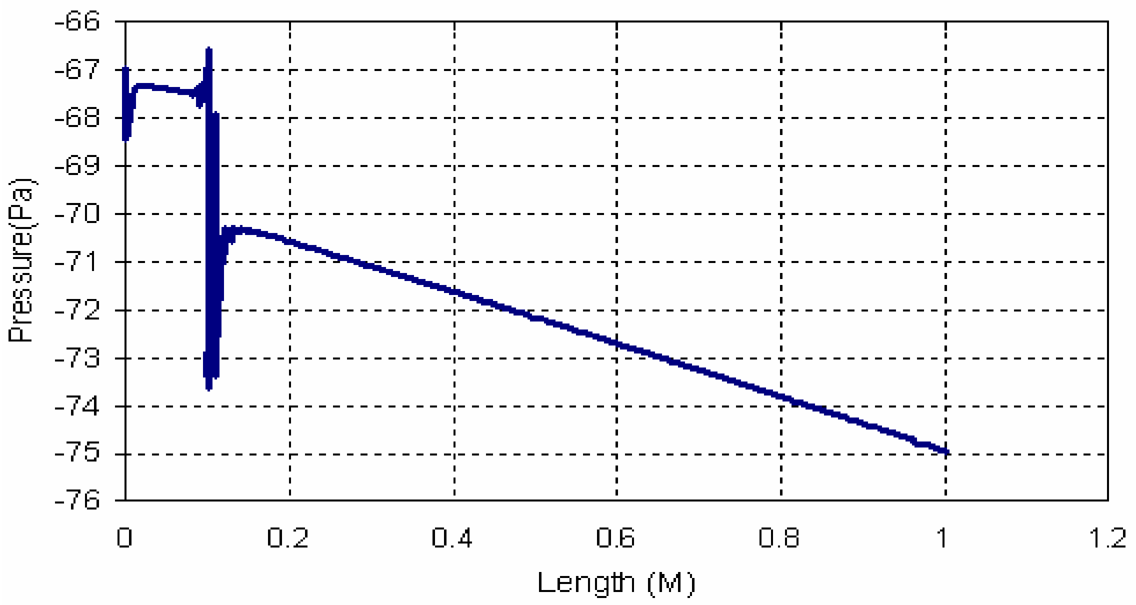

Figure E1 Graph of simulated data where the disturbance ratio (Q_{in}/Q) is 0.36608

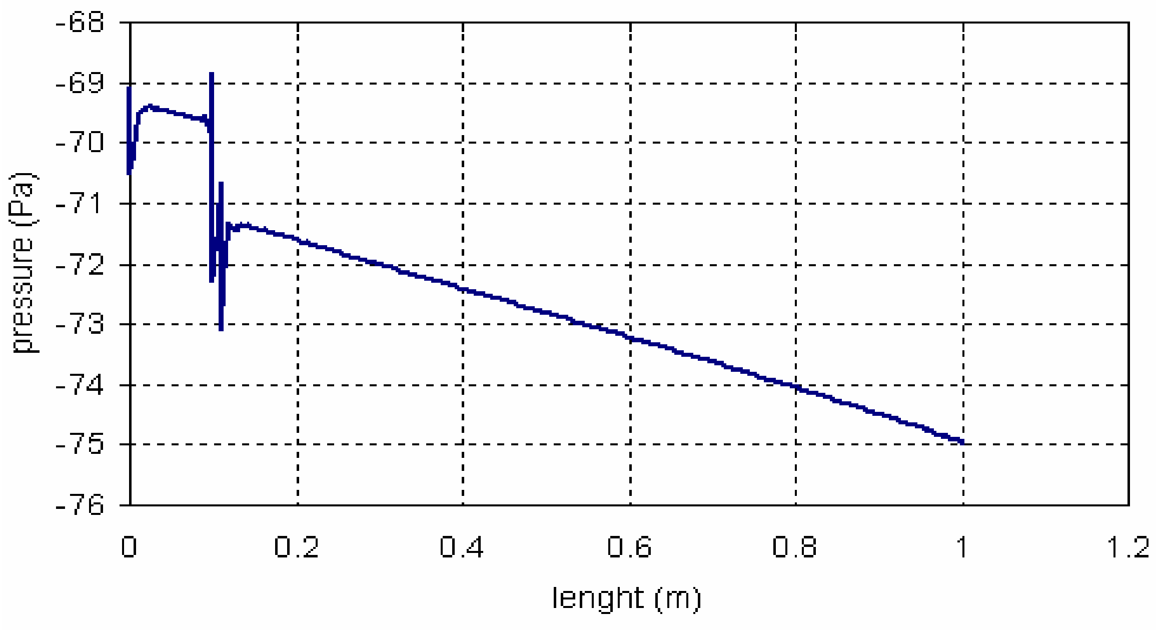

Figure E2 Graph of simulated data where the disturbance ratio (Q_{in}/Q) is 0.23815

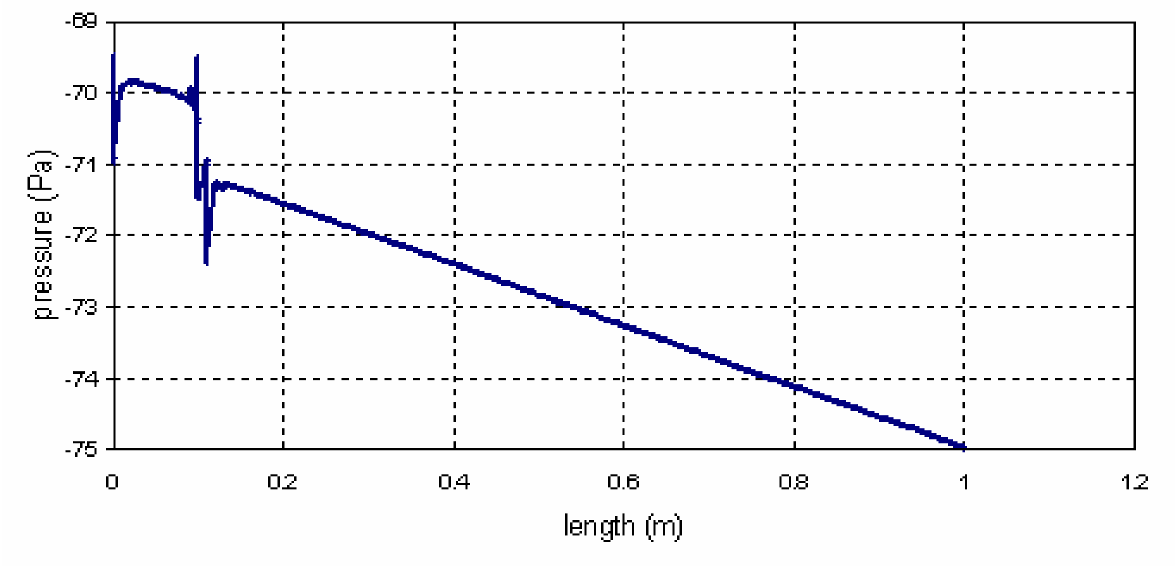

Figure E3 Graph of simulated data where the disturbance ratio (Q_{in}/Q) is 0.21955

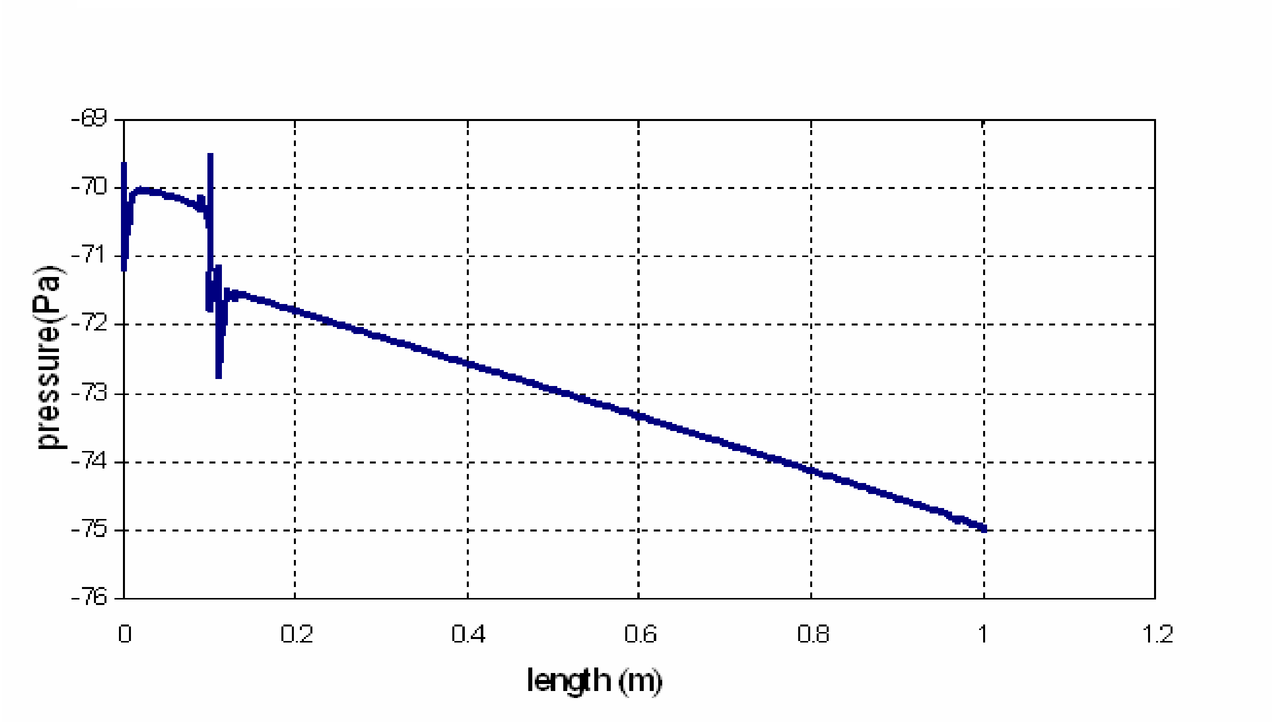

Figure E4 Graph of simulated data where the disturbance ratio (Q_{in}/Q) is 0.18431

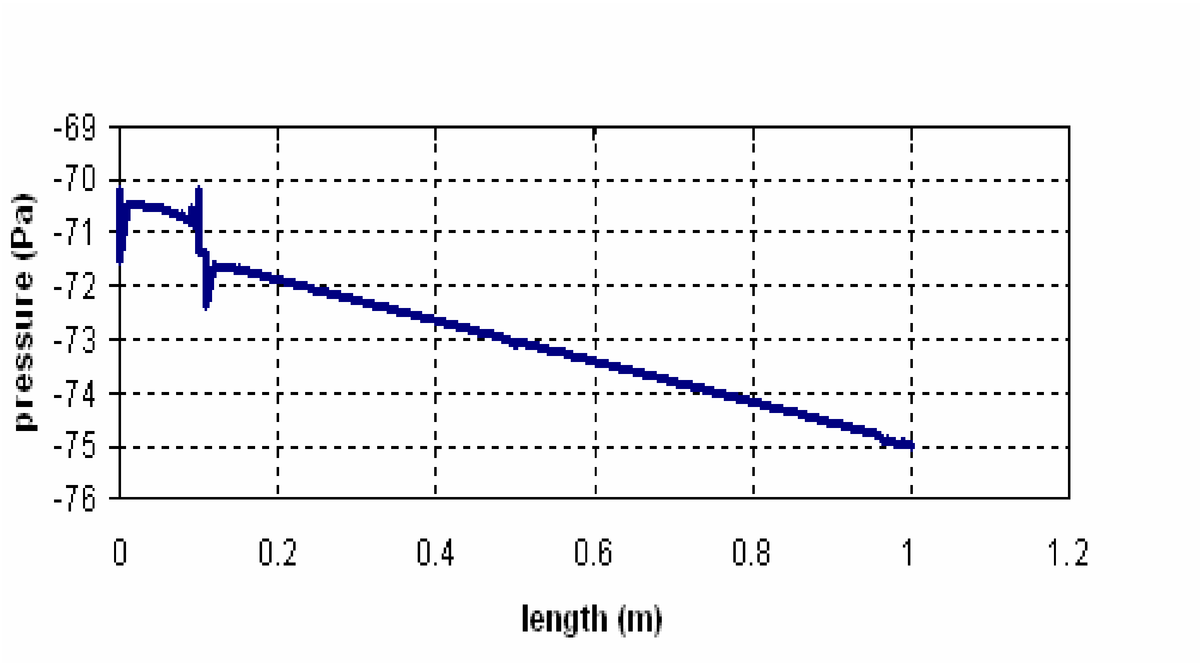

Figure E5 Graph of simulated data where the disturbance ratio (Q_{in}/Q) is 0.12845